UNIVERSITÀ DEGLI STUDI DI NAPOLI "FEDERICO II"

Scuola Politecnica e delle Scienze di Base

Area Didattica di Scienze Matematiche Fisiche e Naturali

Dipartimento di Fisica "Ettore Pancini"

Laurea Magistrale in Fisica

Study and experimental implementation of two-qubit superconducting quantum circuits

Relatori:
Prof. Tafuri Francesco
Dott. Davide Massarotti
Dott.ssa Halima Giovanna Ahmad

Candidato:
Viviana Stasino
Matr. N94000723

Anno Accademico 2022/2023

Contents

Introduction

The concept of Quantum Advantage represents an ambitious goal in the field of quantum computation. It is related to scientific and technological achievements for which quantum computers overcome the computational capabilities of classical computers [1]. Quantum computation is expected to offer great potential in solving hard problems, such as simulating complex molecules [2][3], optimizing neural networks [4], or cryptography [5], with unprecedented speed and efficiency. In order to harness the full potential of quantum computing, the quantum hardware needs to scale to a large numbers of qubits and the development of efficient quantum algorithms is required [6][7].
This thesis aims at exploring the protocols used for optimizing sequences of quantum gates, referred to as *quantum circuits*. Their optimization is a crucial aspect of quantum algorithm design, which allows for the reduction of resource requirements, while maintaining the accuracy and efficiency of quantum computation, in terms of gate fidelities and mitigation of quantum errors. As quantum circuits grow in complexity with an increasing number of qubits and gates, optimization techniques become essential to overcome the challenges in large-scale quantum computing. Specifically, the main goal of this work is to contribute to characterize multi-qubit superconducting devices by realizing specific state-of-the-art protocols for the implementation of quantum circuits.
The work is composed of four Chapters. The first one describes the theoretical principles of superconducting quantum platforms. We discuss how a superconducting circuit encompassing Josephson junctions behaves as a macroscopic quantum system and can be used as a qubit. Hence, we focus on a specific qubit design, namely the transmon, the possibility to tune the electrodynamical parameters of the device through flux-biasing, and to exploit this property for the implementation of two-qubit gates, which can guarantee logical operations in quantum computation. The Chapter also describes the readout of qubit states in a quantum non-demolitive way, and introduces the concept of qubit drive. The computing potential in superconducting devices is affected by noise and decoherence, which are analyzed to better understand their effects on qubit stability. Finally, we describe the possible ways to engineer the coupling between two superconducting qubits, providing an insight into the interactions that allow for entanglement and complex quantum operations.
The second Chapter is focused on the techniques employed for the implementation of

algorithms in quantum devices. We first describe single-qubit gates, with particular emphasis on the Hadamard gate, extensively used in the experimental work. Then, the protocols used for optimizing the single-qubit gates are described, as well as those used to estimate decoherence times. In addition, there is a description of two-qubit gates, like the CNOT gate, which is another gate used in the experiments. Finally, quantum non-demolition readout techniques are discussed, focusing on the requirements to achieve high-fidelity single-shot readout.

The experimental details of the cryogenic and room-temperature electronics setup used in this work, as well as an overview on the architecture, design principles and functionalities of the device analyzed in this work, i.e. a 5-qubit superconducting quantum processor, are reported in Chapter 3.

The last Chapter is focused on the experimental results and the analysis on one qubit pair of the 5-qubit system, i.e., on a two qubit register, both in terms of single-qubit performances, coupling mechanisms, gate pulse optimization and fidelity of different single- and two-qubit quantum circuits. Through Quantum State Tomography (QST), the attainment of Bell states has been demonstrated, which is the maximum manifestation of the quantum entangled nature of the system.

Chapter 1

Superconducting quantum bits

Quantum computers have been proposed as efficient platforms for solving hard problems, as for instance the factorization of large numbers [6], modelization of complex systems [3], molecule's simulations [2]. The main difference between quantum and classical computers relies on how the information is encoded. In classical computers, the information is encoded in two logical states, "0" and "1". Quantum computers use the quantum bit, or *qubit*. A qubit obeys to the following laws of quantum mechanics:

- Quantum superposition, i.e., a qubit state can be represented as:

$$|\Psi\rangle = \alpha\,|0\rangle + \beta\,|1\rangle\,, \qquad \text{with } |\alpha|^2 + |\beta|^2 = 1, \tag{1.1}$$

  where $|0\rangle$ and $|1\rangle$ are the qubit basis eigenstates. A qubit state can be also represented as a vector on the Bloch sphere, as shown in figure 1.1.

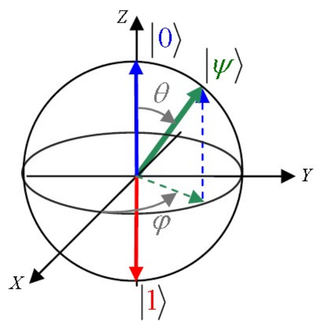

Figure 1.1: Representation of a generic qubit state (green arrow) $|\Psi\rangle$ on the Bloch sphere. The blue and red arrows represent the ground state and the excited state respectively. The angles θ and φ describe the precession and the rotation around z-axis, respectively.

The z-axis connects the north and the south pole, which represent state $|0\rangle$ and state $|1\rangle$, respectively. It is possible to represent the quantum state using the angles θ and φ as:

$$|\Psi\rangle = \cos\frac{\theta}{2}|0\rangle + e^{i\varphi}\sin\frac{\theta}{2}|1\rangle \,. \tag{1.2}$$

- Quantum entanglement: coupled qubits will influence each other. If we know the state of one of the two qubits, the state of the other one is automatically known as well. This property can be used in computation and algorithm designs.

Quantum computation is significantly efficient in solving a large variety of problems [2][4][3], which cannot be solved by a classical computer. The physical realization of quantum computers must fulfill precise requirements, known as *Di Vincenzo's criteria* [8].

- *Scalable physical system with well characterized qubits*: a quantum computer must be made up of many quantum bits, whose parameters are accurately known (energy of the states, coupling to other qubits, coupling to the environment).

- *Ability to initialize the state of the qubits to a simple fiducial state*: it must be possible to initialize the qubits in a well defined state. As a matter of fact, any algorithm would require the computational register to be in some known state before any specific algorithm.

- *A 'universal' set of quantum gates*: any quantum algorithm is a set of unitary instructions that involve some number of qubits. Instead of implementing a series of arbitrary Hamiltonians, it is more convenient to break them down into some set of constituent parts. There are many possible sets of "universal" gates, that will be discussed in Section 2.6.

- *A qubit-specific measurement capability*: it must be possible to read the state of the quantum system, typically via readout of individual qubits.

- *Long relevant coherence times, much longer than the gate operation time*: a large number of single and 2-qubit gate operations must be performed within the coherence time of the qubit. During this mean time the qubit should not randomly go into another state. This loss of information, known as decoherence, may be due to unintentional coupling to the environment and noise in control and readout signals.

In literature, there are several hardware platforms to realize qubits according to the Di Vincenzo's criteria. In this thesis, we will focus on superconducting qubits. In this Chapter, basic notions on superconductivity, superconducting circuit and superconducting qubits will be introduced, with a particular focus on a specific qubit, called *transmon* [9][10].

1.1 Superconductivity and the Josephson Effect

Superconductivity is a peculiar state of the matter that occurs below a critical temperature T_c. A superconductor is characterized by:

- Perfect conductivity, i.e., the resistivity of the material drops to zero below the critical temperature T_c (Figure 1.2a));
- Meissner effect: superconductors expel external magnetic fields up to a critical field H_c below T_c (Figure 1.2b)). The superconductor is capable of expelling the external magnetic fields, expect for a superficial region of thickness λ, called London penetration depth [11].

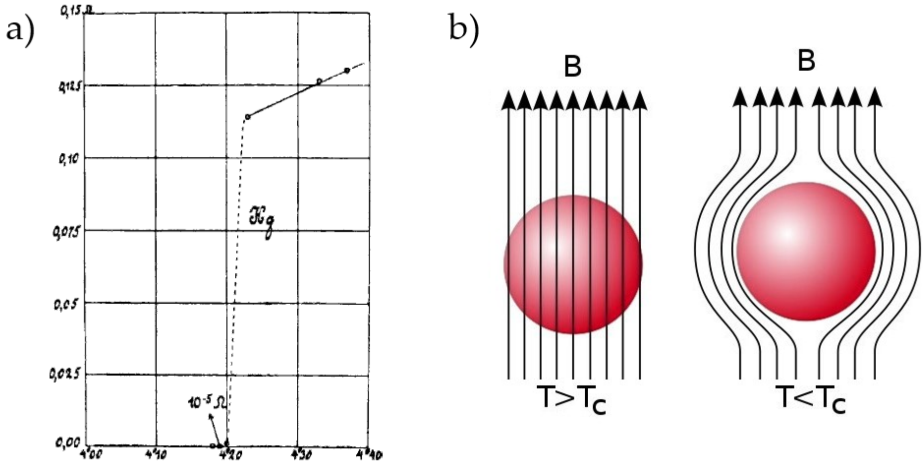

Figure 1.2: In a) resistivity as a function of the temperature measured by Kamerlingh Onnes when he discovered superconductivity in Leiden in 1911 [12]; b) Meissner effect: if $T > T_C$ the magnetic field B penetrates the metallic material, while for $T < T_C$ it is expelled from the superconductor [13].

The Bardeen-Cooper-Schrieffer (BCS) theory of superconductivity states that below T_c, a condensate of Cooper-pairs, pairs of electrons in a singlet state, originates [13]. Such condensate can be represented as a quantum wavefunction, with a macroscopic quantum phase. Therefore, one can build circuits made of superconducting capacitors and inductors by using intrinsic dissipationless materials, including LC-circuits. They will exhibit quantum behavior with energy levels set by their electrodynamical parameters. The Hamiltonian is the Quantum Harmonic Oscillator (QHO) Hamiltonian [14], with energy spectrum shown in figure 1.3.

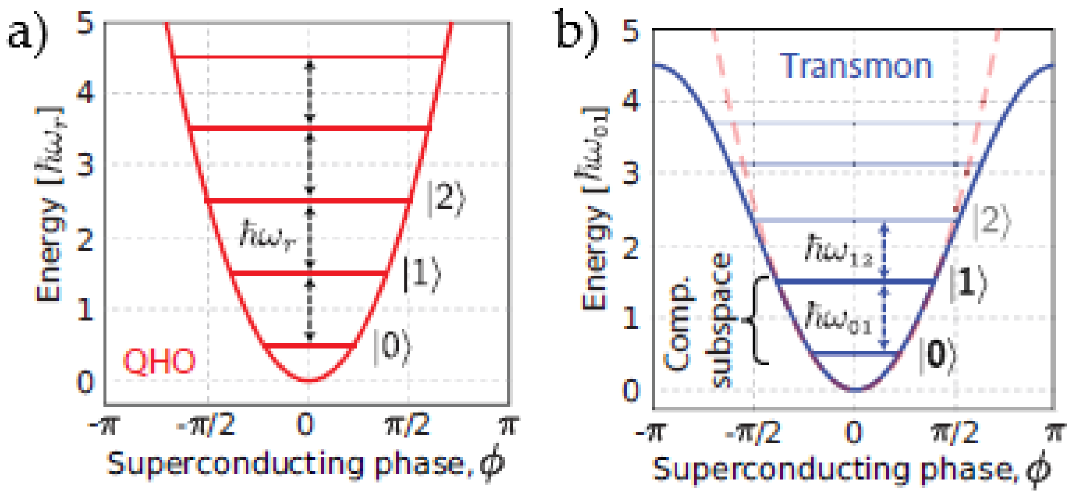

Figure 1.3: In a) the energy potential for the linear Quantum Harmonic Oscillator (QHO) as a function of the superconducting phase. The energy levels are equally spaced by $\hbar\omega_r$, where ω_r is the characteristic oscillation frequency of the LC circuit [15]; b) energy potential for the quantum oscillator with non-linear Josephson inductance, which yields non-equidistant energy levels [15].

The Hamiltonian for the circuit is:

$$H = 4E_C n^2 + \frac{1}{2}E_L\phi^2, \tag{1.3}$$

where $E_C = e^2/(2C)$ is the charging energy of a single electron stored on the capacitance C and $E_L = (\Phi_0/2\pi)^2/L$ is the inductive energy. Here Φ_0 is the magnetic flux quantum $\Phi_0 = h/(2e)$, n is the number of Cooper pairs and ϕ is the superconducting phase. The two operators $\hat{n}$ and $\hat{\phi}$ form a canonical conjugate pair, obeying the commutation relation $\left[\hat{\phi}, \hat{n}\right] = i$. However, the parabolic potential energy of the QHO is not suitable to implement a qubit. It is necessary to define a computational subspace consisting of only two energy states, where transitions can be driven without exciting other energy levels in the system. Anharmonicity can be introduced by replacing the linear inductor of the QHO with a Josephson junction (JJ), that plays the role of a nonlinear inductor [15][11].
A JJ is composed of two superconductors separated by a non superconductor layer, as shown in figure 1.4.

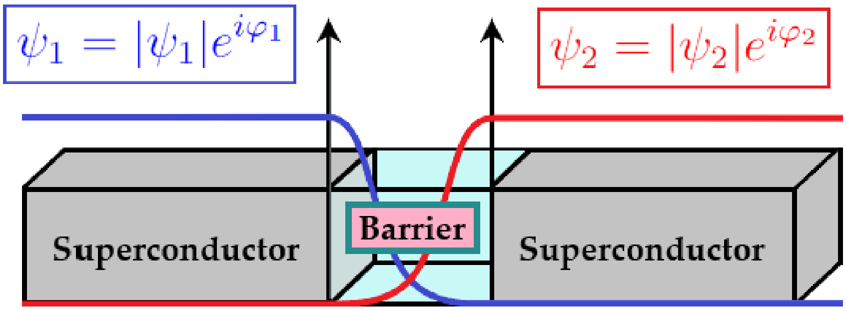

Figure 1.4: Schematic representation of a Josephson junction. The grey parts indicate the superconductors and the light blue represents the barrier between the superconducting layers. It is also shown the penetration of the macroscopic wave functions ψ_1 and ψ_2 into the right (blue line) and left (red line) superconducting electrodes, respectively. The $|\psi_i|^2$ with $i = 1, 2$ is the Cooper pair density and φ_i is the wave function phase.

If the barrier is thin enough, of the order of $1nm$ for insulating layers, tunneling of Cooper pairs from a superconductor to the other will occur due to a phase difference $\phi = \varphi_1 - \varphi_2$ between the macroscopic wave functions of the two superconductors [16]. The tunneling supercurrent I_S is described by the first Josephson equation [16]:

$$I_S = I_C \sin\phi, \tag{1.4}$$

where I_C is the critical current, i.e., the maximum supercurrent that flows through the junction and it is set by several junction parameters, like the materials and the geometry of the device [11].
The time evolution of the phase ϕ is described by the second Josephson equation [16]:

$$V = \frac{\hbar}{2e}\frac{d\phi}{dt}, \tag{1.5}$$

where $V(t)$ is the voltage across the JJ.
By combining the Josephson equations, it is possible to demonstrate that the JJ behaves as a non-linear inductor, with inductance defined as:

$$L_J = \frac{\hbar}{2eI_C \cos\phi} \,. \tag{1.6}$$

Therefore, using the equations (1.4) and (1.5), the Hamiltonian of the JJ is given by [11]:

$$H = 4E_C n^2 - E_J \cos\phi \,, \tag{1.7}$$

where $E_J = I_C\Phi_0/2\pi$ is the Josephson energy, with I_C the critical current of the junction. The cosinusoidal potential energy of the circuits allows to get different energy

transitions among the quantized levels, thus providing the possibility to isolate an artificial quantum two-level state, if properly engineered.
The system dynamics is governed by the E_J/E_C ratio [15]. If $E_J \leq E_C$, we have the so-called *Cooper pair box* (CPB), the first successful superconducting qubit, also know as charge qubit, since the quantum variable is the charge [17] [18]. If $E_J \gg E_C$, we have the flux or the phase qubit, since the quantum variable is the phase difference across the JJ [15][19].

1.2 From the Cooper Pair Box to the transmon qubit

The first successful superconducting qubit was the Cooper Pair Box (CPB), whose circuit is shown in figure 1.5 [17].

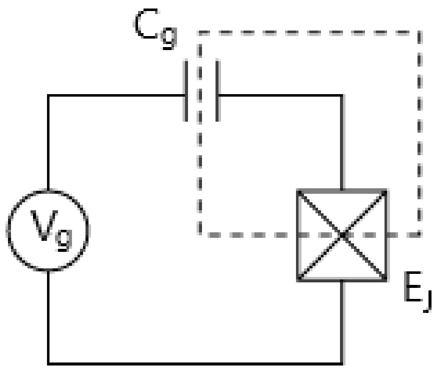

Figure 1.5: Circuit diagram of a Cooper Pair Box, with E_J the Josephson energy, C_g the coupling capacitance and V_g the signal generated by the external electronics.

The CPB is composed of a superconducting island coupled by a Josephson junction to a superconducting reservoir. The Hamiltonian of the CPB is:

$$H = 4E_C(n - n_g)^2 - E_J \cos\phi, \tag{1.8}$$

where n_g is the effective offset charge of the device, which is here the quantum observable. It is controlled by a gate electrode capacitively coupled to the island, such that:

$$n_g = \frac{Q_r}{2e} + \frac{C_g V_g}{2e}, \tag{1.9}$$

where Q_r is the environment-induced offset charge, while V_g and C_g denote the gate voltage and capacitance, respectively.

The equation (1.8) can be solved exactly in the phase basis in terms of Mathieu functions. The eigenenergies are given by [9]:

$$E_m(n_g) = E_C a_{2[n_g+k(m.n_g)]}(-E_J/2E_C), \tag{1.10}$$

where $a_\nu(q)$ denotes Mathieu's characteristic value, and $k(m, n_g)$ is a function sorting the eigenvalues. Typical E_J/E_C ratios of the CPB are well below 1 [9]. An example of the energy transition levels of a CPB is reported in figure 1.6 a) in the limit of $E_J/E_C = 1$.

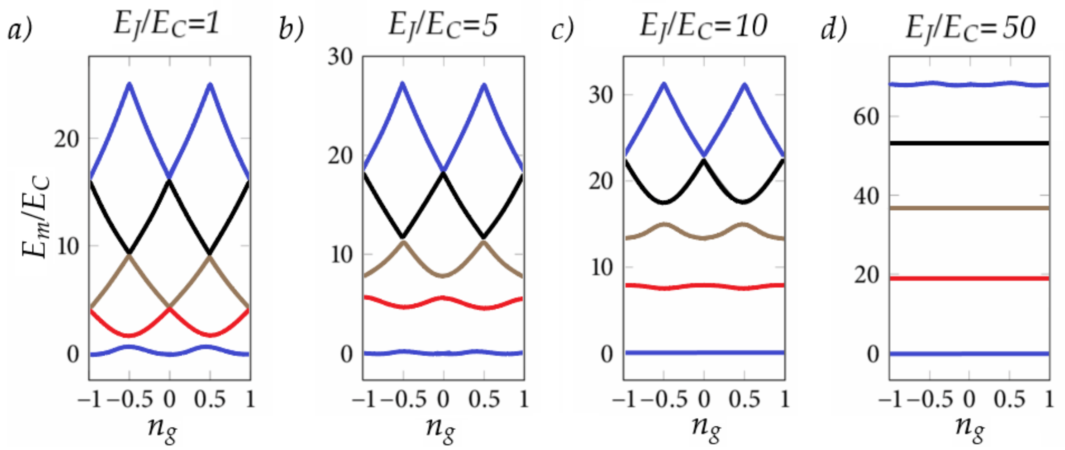

Figure 1.6: Eigenenergies E_m for $m = 0$ (lower blue line), 1 (red line), 2 (brown line), 3 (black line), 4 (upper blue line) of the qubit Hamiltonian as a function of the effective offset charge n_g for different values of E_J/E_C [20].

There are two fundamental quantities for the operation of a CPB: anharmonicity and charge dispersion of the energy levels [9]. A sufficiently large anharmonicity is needed to prevent qubit operations from exciting other transitions in the system. Typical energy scales for the anharmonicities are related to the charging energy: the larger, the higher the separation between the first two computational levels state and the other transition levels. The charge dispersion describes the variation of the energy levels with respect to environmental offset charge and gate voltage, and determines the sensitivity of the CPB to charge noise: the smaller the charge dispersion, the less the qubit frequency will change in response to charge fluctuations. These two quantities are both related to the ratio E_J/E_C: increasing this ratio the charge dispersion, and thus the sensitivity to charge noise, decreases, as shown in figure 1.6 for $E_J/E_C = 5$ (1.6 b)), $E_J/E_C = 10$ (1.6 c)) and $E_J/E_C = 50$ (1.6 d)). The coherence times of the CPB are too small for scalable quantum computation because of the charge noise sensitivity far from the so-called "sweet-spots", i.e., where $dE/dn_g = 0$ [21]. By increasing the E_J/E_C ratio around 50, we can efficiently suppress charge noise fluctuations, thus leading to the implementation of a transmon qubit, whose circuit schematic is shown in figure 1.7.

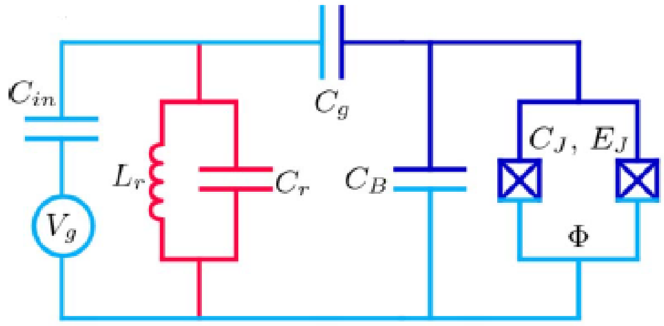

Figure 1.7: Effective circuit diagram of the transmon qubit. The two Josephson junctions in a superconducting ring (also known as DC-SQUID) with capacitance C_J and Josephson energy E_J are shunted by an additional large capacitance C_B, matched by a comparably large gate capacitance C_g. The transmon is connected to a readout resonator (in red) [9].

The crucial difference between the transmon and the CPB is the addition of a large capacitance C_B and of a readout resonator, which allows for the so-called *Quantum Non Demolition* (QND) measurement, i.e., to readout the qubit state without destroying it.
It is important to note that charge dispersion reduces exponentially by increasing the values of E_J/E_C, while anharmonicity tends to decrease polynomially with E_J/E_C. In figure 1.8, it is shown the behavior of the absolute and relative anharmonicity as a function of E_J/E_C, defined as:

$$\alpha = E_{12} - E_{01} \tag{1.11}$$

$$\alpha_r = \frac{\alpha}{E_{01}}. \tag{1.12}$$

More specifically, α_r changes sign for $E_J/E_C > 9$, which means that for larger energy ratios than those of the CPB, the transition energy E_{12} becomes smaller than E_{01} and there is a local minimum for $E_J/E_C \approx 17.5$ [9]. It is possible to find approximate forms of the anharmonicities in the $E_J/E_C \approx \infty$ limit, i.e., in the transmon limit[9], which are:

$$\alpha \simeq -E_C \qquad \alpha_r \simeq -\left(\frac{8E_J}{E_C}\right)^{-\frac{1}{2}}. \tag{1.13}$$

It is, therefore, possible to notice that for the transmon it is possible to find a suitable region of E_J/E_C for which we can efficiently suppress charge noise, without critically affect the anharmonicity.

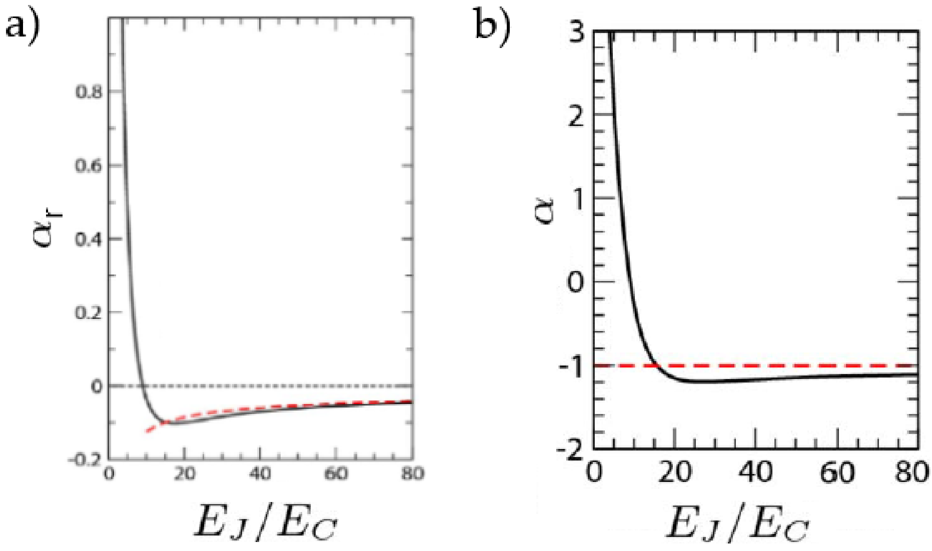

Figure 1.8: In a) relative anharmonicity of the trasmon qubit at the degeneracy point as a function of the ratio E_J/E_C; b) absolute anharmonicity at the degeneracy point as a function of the ratio E_J/E_C. The solid curves show the exact results from equation 1.10, and the dashed curves depict the perturbative result from equation 1.13. Figure adapted from [9].

1.3 Flux tunability of the transmon qubit

In the transmon qubit circuit in figure 1.7 there is a superconducting loop, interrupted by two Josephson junctions. This is a superconducting quantum interference device, also known as *dc-SQUID*. Although it is not a mandatory element in a transmon circuit, it is beneficial because it allows for the tuning of the effective E_J by changing the external magnetic flux ϕ_{ext} threading the loop [11]. The qubit frequency becomes a function of the external flux ϕ_{ext}:

$$\omega_q(\phi_{ext}) = \sqrt{8E_J(\phi_{ext})E_c} - \frac{E_c}{2}, \tag{1.14}$$

where

$$E_J(\phi_{ext}) = E_{J\Sigma} \cos\frac{\pi\phi_{ext}}{\phi_0}\sqrt{1 + d^2 \tan\left(\frac{\pi\phi_{ext}}{\phi_0}\right)^2} \tag{1.15}$$

and

$$d = \frac{E_{J1} - E_{J2}}{E_{J1} + E_{J2}}. \tag{1.16}$$

The d factor is an asymmetry parameter, that takes into account the possibility of having a SQUID with two different JJs: the bigger the asymmetry parameter d, the smoother is the variation of the qubit frequency as a function of the flux, as shown in figure 1.9.

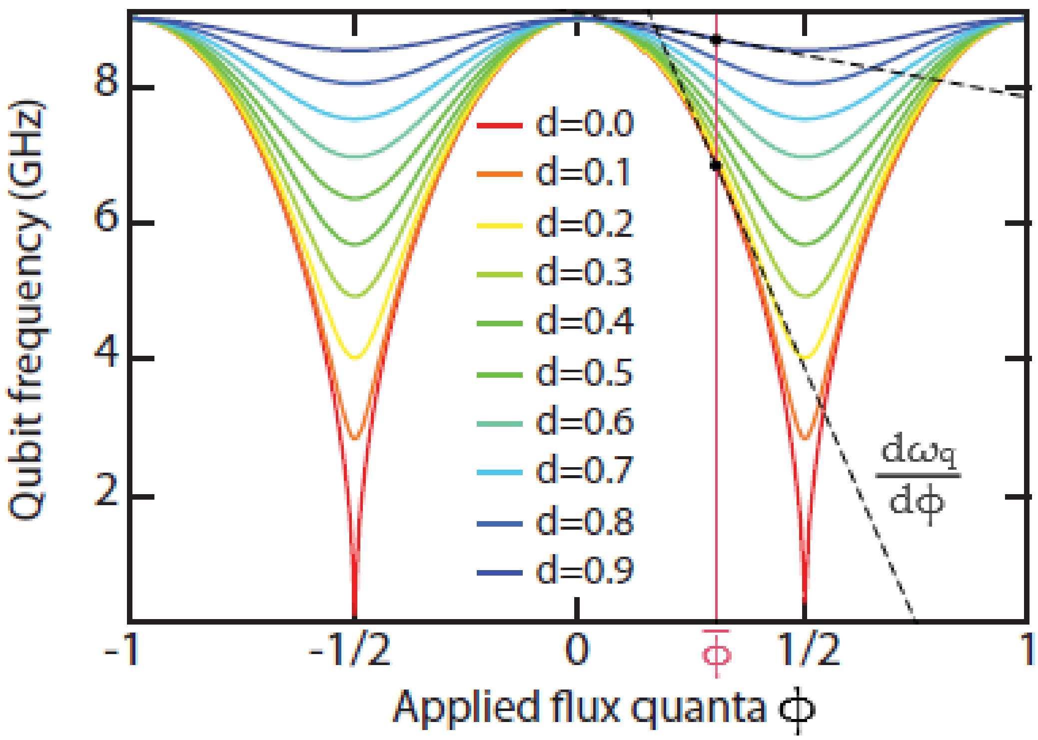

Figure 1.9: Transmon qubit frequency tuning as a function of the external flux for different values of the asymmetry parameter d. The dashed lines represent the slope $d\omega_q/d\phi$ at some specific points. For a fixed flux value $\bar{\phi}$ the slope for $d = 0.0$ is smaller than for $d = 0.9$. Therefore, when the junctions have different sizes the qubit is less sensitive to flux changes. Figure adapted from [14].

This helps in reducing the sensitivity to flux noise, which can be quantified in terms of the derivative of ω_q as a function of the flux, $d\omega_q/d\phi_{ext}$ [9]. The possibility to tune the qubit frequency is fundamental for the implementation of single- and two-qubit gates, as will be discussed in Section 2.1.

1.4 Readout of Transmon Qubit

Coherent control and readout of the transmon qubits can be achieved by operating the system in the dispersive limit, which allows for QND measurement [15]. Specifically, the transmon uses a superconducting resonator, which is represented by a harmonic LC oscillator in the limit of $\ell \ll c/f_\nu$, where ℓ is the length of the resonator and ν are the typical frequencies in the microwave regime.
The system composed of the transmon and the resonator is described by the Jaynes-Cummings (JC) Hamiltonian, given by [15]:

$$H_{JC} = \omega_r\Big(a^\dagger a + \frac{1}{2}\Big) + \frac{\omega_q}{2}\sigma_z + g\big(\sigma_+ a + \sigma_- a^\dagger\big), \tag{1.17}$$

where ω_r is the frequency of the resonator, ω_q is the frequency of the qubit, g represents the coupling between qubit and resonator, $a^\dagger$ and a are the creation and annihilation operators of the single excitation of the resonator, respectively, and σ_+ and σ_- represent the excitation and the de-excitation of the qubit. Here, the qubit has been approximated as a two-level system for simplicity. The third term of JC Hamiltonian describes the interaction between the qubit and the resonator through the factor g, which is fundamental to identify the working regime. Transmon qubits generally work in the dispersive regime, which is reached when $g \ll \Delta$, where Δ is the detuning $\Delta = |\omega_q - \omega_r|$. Developing a second-order perturbation theory with respect to g/Δ, it is possible to obtain:

$$H_{disp} = \big(\tilde{\omega}_r + \chi\sigma_z\big)\Big(a^\dagger a + \frac{1}{2}\Big) + \frac{\tilde{\omega}_q}{2}\sigma_z, \tag{1.18}$$

where $\chi = g^2/\Delta$ is the *dispersive shift*, $\tilde{\omega}_q = \omega_q + g^2/\Delta$ and $\tilde{\omega}_r = \omega_r + \chi\sigma_z$ are the renormalized frequencies.
In order to perform a QND measurement, a single-tone signal in the range of the resonator frequency interacts with the readout resonator. The response of the voltage magnitude across the resonator indicates the adsorption of photons and it is possible to see a dip corresponding to the resonance frequency of the readout resonator (see Figure 1.10). To identify the dispersive regime, readout resonator spectroscopy is performed as a function of the power of the input signal. For sufficiently low input power, we can enter the single-photon regime. Once this regime is reached, the resonance frequency of the resonator will shift positively or negatively accordingly to the detuning sign and the state of the qubit (Figure 1.10.)

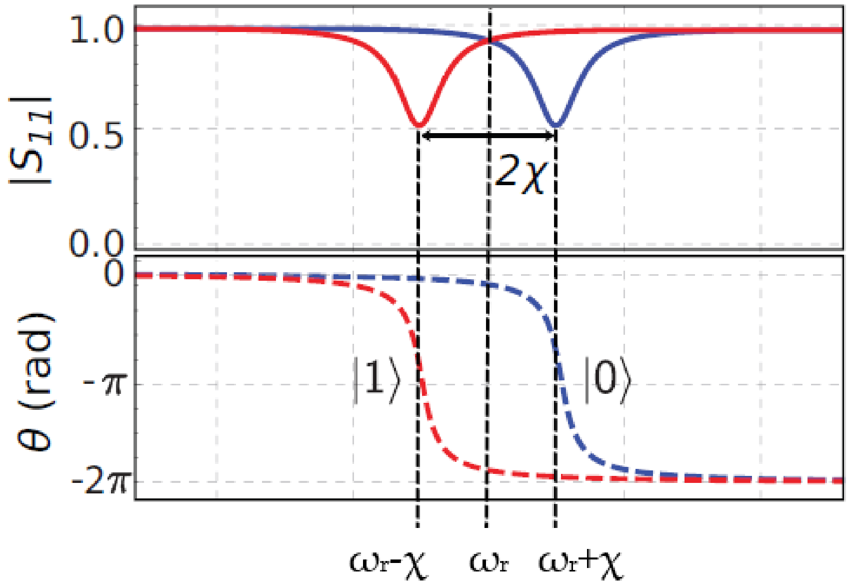

Figure 1.10: Quantum non demolitive readout of a transmon qubit. Reflected magnitude $|S_{11}|$ and phase θ response of the resonator when the qubit is in its ground state $|0\rangle$ (blue) and excited state $|1\rangle$ (red), separated by the dispersive shift frequency 2χ. Figure adapted from [15].

1.5 Qubit drive

In order to perform gate operations, it is necessary to drive the qubit along the Bloch Sphere, through an RF signal which resonates with the qubit transition frequency.
In figure 1.11 it is shown the circuit diagram of microwave drive line capacitively coupled to a transmon qubit.
The Hamiltonian of the system in equation 1.17 becomes:

$$H = H_{JC} + H_d = H_{JC} + \frac{C_d}{C_{d,\Sigma}} V_d(t)\hat{Q}, \tag{1.19}$$

where C_d is the coupling capacitance, $C_{d,\Sigma} = C + C_d$ is the total capacitance to ground and $\hat{Q}$ is the charge operator [15]. It is possible to express the latter in terms of raising and lowering operators:

$$\hat{Q} = -i\sqrt{\frac{\hbar}{2Z}}(a - a^\dagger), \tag{1.20}$$

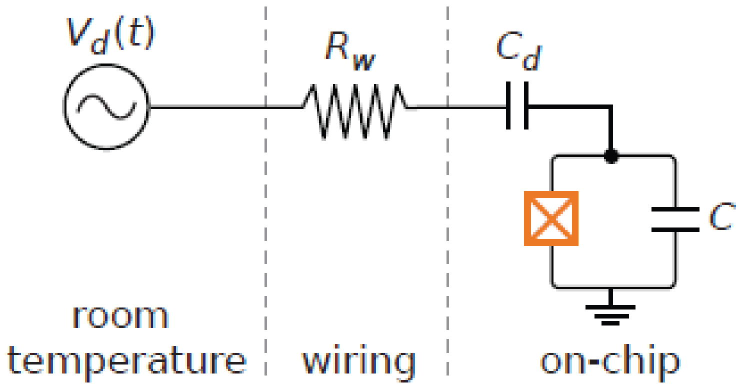

Figure 1.11: Circuit diagram of a microwave drive line capacitively coupled to a generic transmon superconducting qubit [15].

where $Z = \sqrt{L/C}$ is the impedance of the circuit to ground. Since $(a - a^\dagger) \propto \sigma_y$, the hamiltionian of the drive H_d becomes:

$$H_d = \frac{C_d}{C_{d,\Sigma}} V_d(t) \sqrt{\frac{\hbar}{2Z}} \sigma_y. \tag{1.21}$$

Using the rotating wave approximation (RWA), for which we move in the frame of reference of the qubit [22], the form of H_d is:

$$H_d = \Omega V_d(t)[\sigma_y \cos \omega_q t - \sigma_x \sin \omega_q t], \tag{1.22}$$

where $\Omega = C_d/C_{d,\Sigma}$ and $\omega_q \simeq (E_1 - E_0)/\hbar$.
We can generally assume that the drive voltage $V_d(t)$ has the generic form:

$$V_d(t) = V_0 s(t)(\cos \phi \sin \omega_d t + \sin \phi \cos \omega_d t), \tag{1.23}$$

where $s(t)$ is a dimensionless envelope function, so that the amplitude of the drive is set by $V_0 s(t)$ [15]. It is useful to define $\delta\omega = \omega_d - \omega_q$ and the *in phase* and *out of phase* components, respectively, as:

$$I = \cos \phi \tag{1.24}$$

$$Q = \sin \phi. \tag{1.25}$$

Using these definitions and the prosthaphaeresis formulae, the driving Hamiltonian takes the form [15]:

$$H_d = \frac{\Omega V_0 s(t)}{2} \Big[(Q \sin \delta\omega t - I \cos \delta\omega t)\sigma_x + (I \sin \delta\omega - Q \cos \delta\omega t)\sigma_y \Big]. \tag{1.26}$$

The last equation is a powerful tool for understanding single-qubit gates in superconducting qubits. In fact, if we assume to apply a drive pulse resonant with the qubit frequency, so that $\delta\omega = 0$, then:

$$H_d = -\frac{\Omega V_0 s(t)}{2}(I\sigma_x + Q\sigma_y). \tag{1.27}$$

This shows that an in-phase pulse performs rotations around the x-axis, while an out-of-phase pulse performs rotations around the y-axis. In figure 1.12, an example of a gate sequence is considered and the rotation around the x-axis on the Bloch sphere due to the I component is highlighted.

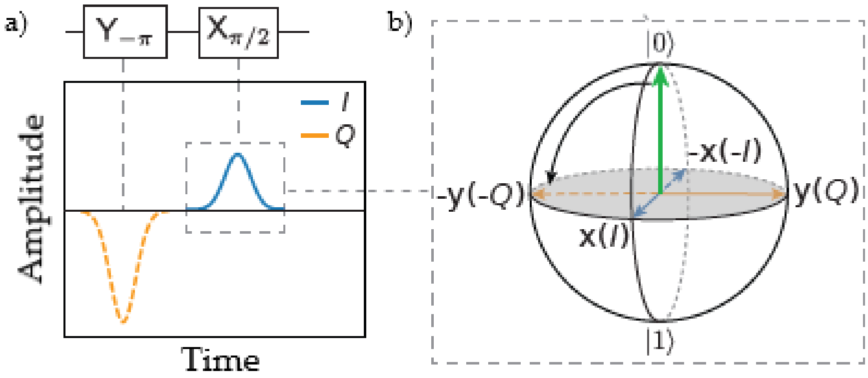

Figure 1.12: In a) an example of a gate sequence, where the blue and orange lines indicate I and Q components, respectively; b) the action of a $X(\pi/2)$ pulse on $|0\rangle$ on Bloch sphere, which put the qubit on the equator, due to the I component. Figure adapter from [15].

1.6 Noise and decoherence

Although the circuital nature of superconducting qubits allows for an easy way of implementing readout, control and tunability of circuital parameters, which are mandatory for the implementation of gates, several dissipation channels come into play, since the control of the qubit or the measurement of its state involve some uncontrollable physical processes that are sources of noise. This leads to decoherence, which affects the fidelity of the qubits and the quantum gates operations [23].

The sources of noise can be divided into two principal categories: *systematic noise*, that is traceable to a fixed control or readout error, thus it can be corrected through a calibration, and *stochastic noise*, that arises from random fluctuations of parameters that are coupled to the qubit [15][24]. This leads to decoherence phenomena, that can be divided into *longitudinal relaxation*, *transverse relaxation* and *pure dephasing*.

1.6.1 Longitudinal relaxation

The longitudinal relaxation rate Γ_1 is defined as:

$$\Gamma_1 = \frac{1}{T_1}, \tag{1.28}$$

where T_1 is the $1/e$ decay time and it is the characteristic time scale for qubit spontaneous exchange of energy with the environment, which leads the qubit to its ground state. It describes depolarization along the qubit quantization axis (z-axis), also called *longitudinal axis* [15].
The longitudinal relaxation is caused by *transverse noise*, via x or y axis, as shown in figure 1.13.

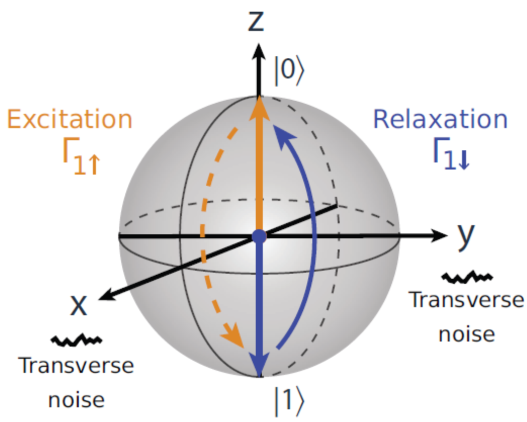

Figure 1.13: Longitudinal relaxation results from energy exchange between the qubit and its environment, due to transverse noise that couples to the qubit in the x-y plane and drives transitions $|0\rangle$ to $|1\rangle$. The blue arrow represents the relaxation process from $|1\rangle$ to $|0\rangle$, while the orange arrow represents the excitation process from $|0\rangle$ to $|1\rangle$ [15].

At the same time, spontaneous excitations from $|0\rangle$ to $|1\rangle$ may occur. If we define the relaxation rate as $\Gamma_{1\downarrow}$ and the excitation rate as $\Gamma_{1\uparrow}$, the total decay rate is:

$$\Gamma_1 = \Gamma_{1\uparrow} + \Gamma_{1\downarrow}. \tag{1.29}$$

However, since the excitation processes follow the Boltzmann statistics, for superconducting qubits the only significant contribution to longitudinal relaxation is given by $\Gamma_{1\downarrow}$ [25],

$$\Gamma_1 = \Gamma_{1\downarrow}\left(e^{-\frac{\hbar\omega_q}{k_B T}} + 1\right) \simeq \Gamma_{1\downarrow}. \tag{1.30}$$

For superconducting transmon qubits, typical T_1 values are of the order of tens or low hundreds of μs [15].
Some of the sources of stochastic noise that lead to relaxation are:

- *Spontaneous emission*, due to the fact that the qubit is coupled with the electromagnetic field inside the transmission line resonator [9];
- *Purcell effect*, that is the enhancement of spontaneous emission rates of photons when they are incorporated into the readout resonant cavity [25][26];
- *Dielectric losses*, due to the charge fluctuations in the defects or charge traps that reside in interfacial dielectrics, in the junction tunnel barrier and in the substrate of the qubit [9];
- *Quasiparticle noise*, due to thermal breaking of Cooper pairs [9][27][28];
- *Flux coupling noise*, due to the coupling of the transmon to an external magnetic flux bias that opens up additional channels for energy relaxation if they are resonant with the transition frequency of the qubit [9].

1.6.2 Pure dephasing

The pure dephasing rate Γ_ϕ describes depolarization in the x-y plane of the Bloch sphere. It is due to *longitudinal noise*, that couples to the qubit via z axis, as shown in figure 1.14.

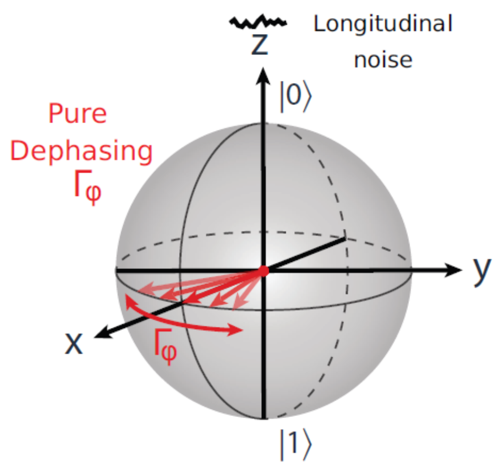

Figure 1.14: Pure dephasing in the transverse plane arises from longitudinal noise along the z axis that induces fluctuations of the qubit frequency. A Bloch vector along the x-axis will move in the equator plane due to stochastic frequency fluctuations, depolarizing the azimuthal phase with a rate Γ_ϕ [15].

This leads to fluctuations of the qubit frequency ω_q. Some of the sources of stochastic noise that lead to pure dephasing are:

- *Charge noise*, which derives from fluctuations of the charge in the superconducting islands of a JJ [9];
- *Flux noise*, that arises from the external magnetic field coupled to the qubit [9][15];
- *Critical current noise*, which is generated by trapping and detrapping of charges associated with spatial reconfigurations of ions inside the JJ [9].

It is important to notice that pure dephasing is not a resonant phenomenon, in contrast to energy relaxation. Therefore, pure dephasing is in principle reversible, by applying unitary operations. On the contrary, spontaneous energy relaxation is an irreversible process: once the qubit emits energy to environment, the quantum information is essentially lost [15].

1.6.3 Transverse relation

The transverse relaxation rate is: $\Gamma_2 = \frac{1}{T_2} = \frac{\Gamma_1}{2} + \Gamma_\phi$. It describes the loss of coherence of a superposition state and it is due to both longitudinal noise and transverse noise, as shown in figure 1.15.

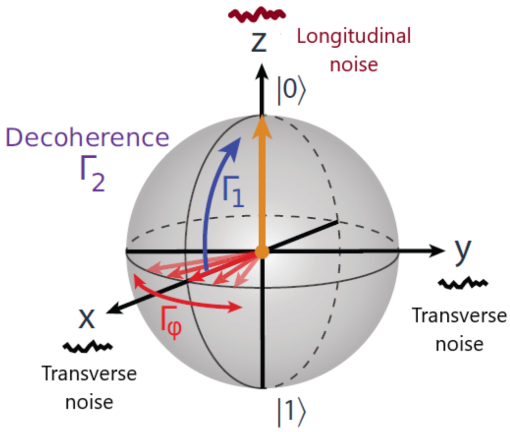

Figure 1.15: Transverse relaxation results in a loss of coherence due to a combination of energy relaxation and pure dephasing. Pure dephasing leads to decoherence of the quantum state $1/\sqrt{2}(|0\rangle + |1\rangle)$, initially pointed along the x-axis. Additionally, the excited state component of the superposition state may relax to the ground state, a phase-breaking process that induces the loss of the orientation of the vector in the x-y plane [15].

For superconducting transmon qubits, typical T_2 values are of the order of tens or low hundreds of μs [9]. In the ideal case, if $\Gamma_\phi = 0$, $T_2 = 2T_1$.

1.7 Coupling between two superconducting qubits

In order to exploit the true potential of quantum computing, two qubits gates become indispensable. They are essential in quantum computing because they enable the manipulation and entanglement of multiple qubits simultaneously, making quantum computing potentially more powerful than classical computing for certain tasks.
While the implementation of single-qubit gates requires to properly design drive pulses on one qubit, two-qubit gates rely on the engineering of a coupling between two qubits, i.e., to establish an interaction between quantum two-level systems. If H_1 and H_2 are the Hamiltonian describing two isolated qubits, the coupled system Hamiltonian H can be written as:

$$H = H_1 + H_2 + H_{int}, \tag{1.31}$$

where H_{int} is the interaction Hamiltonian. It can have different forms depending on the type of circuital coupling [15]. Some of them are shown in figure 1.16, and include the possibility to connect two qubits on a chip by direct capacitive or inductive coupling (a) and c)), or through an additional circuital element, like a coupler resonator or a qubit coupler (b) and d)).

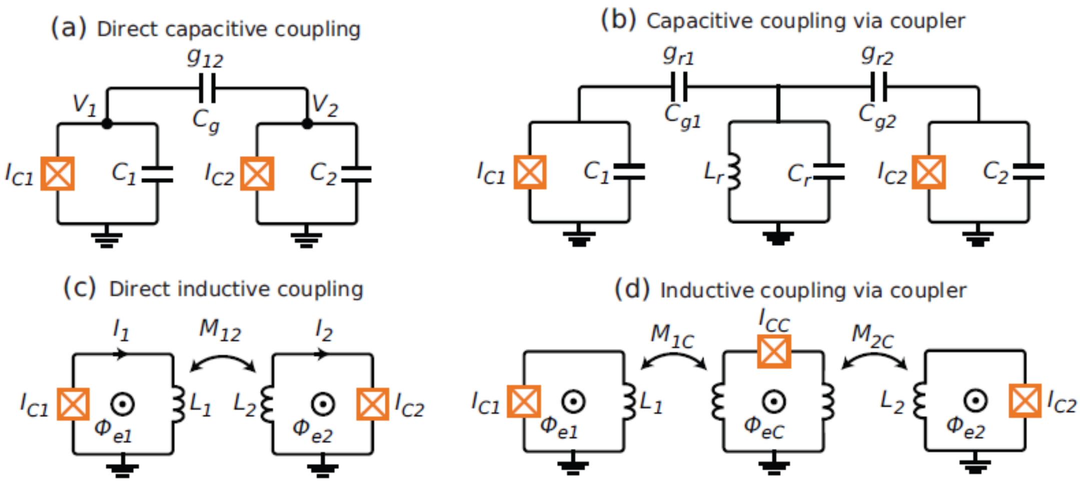

Figure 1.16: The figure shows two qubits that are coupled: a) by a capacitance C_g, b) via a resonator coupler, c) via mutual inductance M_{12}, d) via mutual inductances M_{1C} and M_{2C} to a frequency tunable coupler [15].

In this thesis, I focused my attention on a quantum chip realized with high-frequency bus resonator couplers, like those in figure 1.16b).
The effective Hamiltonian of such a system in the dispersive limit, where both qubits are far detuned from resonator coupler, can be written as [29]:

$$H_{eff} = \sum_{i=1,2} \left(\frac{\hbar\omega_i}{2}\sigma_i^z + \hbar\chi_i\sigma_i^z \right) + \hbar\omega_r a^\dagger a + \hbar J(\sigma_1^-\sigma_2^+ + \sigma_2^-\sigma_1^+), \tag{1.32}$$

where $J = \frac{g_1 g_2}{2}(\frac{1}{\Delta_1} + \frac{1}{\Delta_2})$. Here g_i is the coupling strength of qubit i and $\Delta_i = |\omega_i - \omega_r|$ is the detuning. The interaction between the qubits is described by the last term of the equation 1.32, also-called J-coupling or transverse exchange coupling [30].
The qubit-qubit interaction is a result of virtual exchange of photons with the cavity. When the qubits are non-degenerate, i.e., $\delta_q = |\omega_1 - \omega_2| \gg J$, the interaction is effectively turned off. If the qubits are set on resonance, typically by an external flux as discussed in Section 1.3, i.e., $\Delta_1 = \Delta_2 = \Delta$, an avoided level crossing of the excited qubit states occurs, with an opening of a gap in the energy spectra [30]. The size of the splitting is $J = \hbar g_1 g_2/\Delta$ and the new eigenstates of the coupled system are:

$$|\psi_s\rangle = \frac{(|01\rangle + |10\rangle)}{\sqrt{2}} \qquad |\psi_a\rangle = \frac{(|01\rangle - |10\rangle)}{\sqrt{2}}.$$

More generally, for $\delta_q \neq 0$ the eigenstates can be written as [30]:

$$|\psi_s\rangle = \sin\theta_n |01\rangle + \cos\theta_n |10\rangle \,, \tag{1.33}$$

$$|\psi_a\rangle = \cos\theta_n |01\rangle - \sin\theta_n |10\rangle \,, \tag{1.34}$$

where θ_n is defined by $\cos 2\theta_n = -\delta_q/\sqrt{4J^2 + \delta_q^2}$ and $\sin 2\theta_n = 2J/\sqrt{4J^2 + \delta_q^2}$ [30]. It is easy to see that asymptotically ($\delta_q \to \infty$) it turns out that $|\psi_s\rangle \to |01\rangle$ and $|\psi_a\rangle \to |10\rangle$. In figure 1.17 it is shown an example of a spectroscopy measurement of the avoided level crossing [30] in two coupled superconducting qubits.

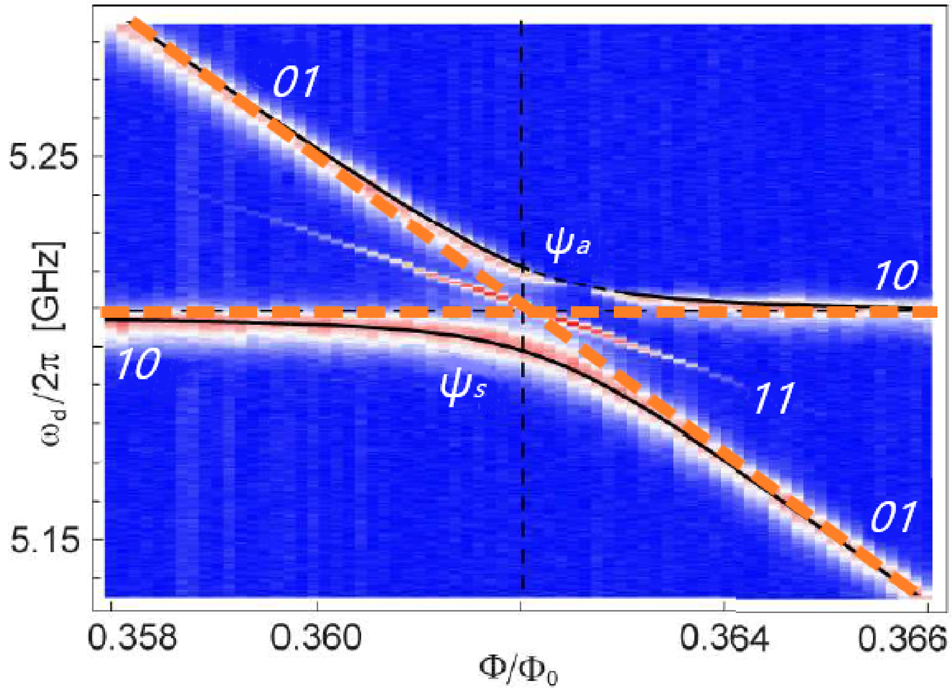

Figure 1.17: Spectroscopic measurement of the avoided level crossing as a function of normalized external flux Φ/Φ_0. The solid lines indicate energy levels calculated from the diagonalization of the two-qubit Jaynes-Cummings Hamiltonian. The orange dashed lines represent the asymptotic behavior of $|\psi_s\rangle$ and $|\psi_a\rangle$. Figure adapted from [30].

In order to observe the avoided level crossing, the first qubit is kept at a fixed frequency, while the second qubit frequency is swept across the avoided crossing by changing its flux bias. If the power of the drive is high enough, it is also possible to see a spectroscopic line centered between the upper and the lower branch. This line represents a two-photon transition from the ground state $|00\rangle$ to the doubly excited state $|11\rangle$. The possibility to establish an avoided level crossing between two qubits is fundamental for the implementation of multi-qubit gates, like the iSWAP or the CZ gates.

Chapter 2

Algorithms with superconducting qubits

Among the several superconducting platforms available in literature [31][32][33], transmon qubits have been successfully used to build gate-based processors, i.e., devices able to perform quantum algorithms. Google, IBM and Rigetti provide processors available on the cloud, offering users the possibility to construct sequences of gates or quantum circuits [34]. A quantum algorithm is defined as a sequence of gate operations able to solve a specific problem. Such operations are typically decomposed in a finite sequence of basic gates, or *quantum circuits* [35]. The gates are part of what are known as universal gate sets, which are mandatory for any quantum processor [8] (Chapter 1). In this Chapter, we will discuss how it is possible to implement single and two qubits gates on superconducting hardware, with a focus on $Hadamard$, CZ and $CNOT$ gates.

2.1 Single-qubit gates

Qubits can assume arbitrary positions on the Bloch Sphere and each state can be written as $|\psi\rangle = \alpha|0\rangle + \beta|1\rangle$. Single-qubit gates allow to move from a point on the Block Sphere to another through rotations around a particular axis, as mentioned in Section 1.5. In figure 2.1 a comprehensive list of single-qubit gates is shown.

GATE	CIRCUIT REPRESENTATION	MATRIX REPRESENTATION	TRUTH TABLE	BLOCH SPHERE
I Identity-gate: no rotation is performed.	$-\boxed{I}-$	$I = \begin{pmatrix} 1 & 0 \\ 0 & 1 \end{pmatrix}$	Input / Output $\vert 0\rangle$ / $\vert 0\rangle$ $\vert 1\rangle$ / $\vert 1\rangle$	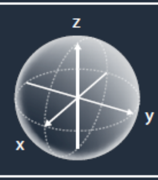
X gate: rotates the qubit state by π radians (180°) about the x-axis.	$-\boxed{X}-$	$X = \begin{pmatrix} 0 & 1 \\ 1 & 0 \end{pmatrix}$	Input / Output $\vert 0\rangle$ / $\vert 1\rangle$ $\vert 1\rangle$ / $\vert 0\rangle$	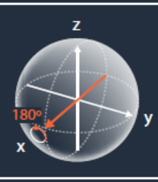
Y gate: rotates the qubit state by π radians (180°) about the y-axis.	$-\boxed{Y}-$	$Y = \begin{pmatrix} 0 & -i \\ i & 0 \end{pmatrix}$	Input / Output $\vert 0\rangle$ / $i\vert 1\rangle$ $\vert 1\rangle$ / $-i\vert 0\rangle$	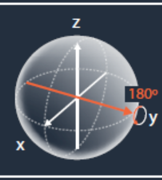
Z gate: rotates the qubit state by π radians (180°) about the z-axis.	$-\boxed{Z}-$	$Z = \begin{pmatrix} 1 & 0 \\ 0 & -1 \end{pmatrix}$	Input / Output $\vert 0\rangle$ / $\vert 0\rangle$ $\vert 1\rangle$ / $-\vert 1\rangle$	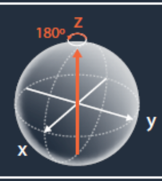
S gate: rotates the qubit state by $\frac{\pi}{2}$ radians (90°) about the z-axis.	$-\boxed{S}-$	$S = \begin{pmatrix} 1 & 0 \\ 0 & e^{i\frac{\pi}{2}} \end{pmatrix}$	Input / Output $\vert 0\rangle$ / $\vert 0\rangle$ $\vert 1\rangle$ / $e^{i\frac{\pi}{2}}\vert 1\rangle$	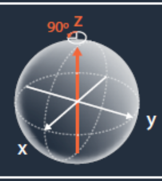
T gate: rotates the qubit state by $\frac{\pi}{4}$ radians (45°) about the z-axis.	$-\boxed{T}-$	$T = \begin{pmatrix} 1 & 0 \\ 0 & e^{i\frac{\pi}{4}} \end{pmatrix}$	Input / Output $\vert 0\rangle$ / $\vert 0\rangle$ $\vert 1\rangle$ / $e^{i\frac{\pi}{4}}\vert 1\rangle$	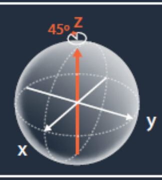
H gate: rotates the qubit state by π radians (180°) about an axis diagonal in the x-z plane. This is equivalent to an X-gate followed by a $\frac{\pi}{2}$ rotation about the y-axis.	$-\boxed{H}-$	$H = \frac{1}{\sqrt{2}} \begin{pmatrix} 1 & 1 \\ 1 & -1 \end{pmatrix}$	Input / Output $\vert 0\rangle$ / $\frac{\vert 0\rangle + \vert 1\rangle}{\sqrt{2}}$ $\vert 1\rangle$ / $\frac{\vert 0\rangle - \vert 1\rangle}{\sqrt{2}}$	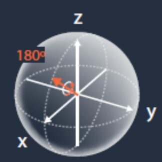

Figure 2.1: For each single-qubit gate, it is shown the circuit representation, the matrix representation, the truth table and the rotation's representation on the Bloch Sphere. Matrices are defined in the z-basis $\{\vert 0\rangle, \vert 1\rangle\}$. Figure adapted from [15].

This includes:

- *I identity gate*: it performs no rotation on the state of the qubit.
- *X/Y/Z gate*: it performs a rotation of an angle π around the x/y/z-axis.
- *S gate*: it performs a rotation of an angle $\pi/2$ around z-axis.
- *T gate*: it performs a rotation of an angle $\pi/4$ around z-axis.
- *H Hadamard gate*: generates a superposition of $|0\rangle$ and $|1\rangle$ state, i.e., it brings the qubit in the equator rotating it around an axis diagonal on the x-z plane.

2.1.1 Hadamard gate

The Hadamard gate is very important in quantum computing, since it allows to generate the superposition of the two basis states. If the qubit state is initialised in a computation state $|0\rangle$ or $|1\rangle$, the Hadamard gate puts the qubit into a superposition of $|0\rangle$ and $|1\rangle$ states. If a Hadamard gate is applied on the $|0\rangle$ state several times and the output is measured on the basis $\{|0\rangle, |1\rangle\}$, it should be observed a probability of 50% to be in the $|0\rangle$ state and of 50% to be in the $|1\rangle$ state, unless statistical errors [36]. It is fundamental to note that in this case each measurement is independent, i.e., the qubit has to be reset to $|0\rangle$ before the application of the Hadamard gate. In fact, the state of the qubit is obtained through a classical projective measurement, which erases the quantum nature of the qubit. After the measurement, the qubit is no longer in a superposition but in a well-defined state, $|0\rangle$ or $|1\rangle$.
The Hadamard gate can be obtain from native gates as:

$$H = Ph_{\frac{\pi}{2}} Y_{\frac{\pi}{2}} Z_{\pi} = i\frac{1}{\sqrt{2}} \begin{bmatrix} 1 & -1 \\ 1 & 1 \end{bmatrix} \begin{bmatrix} -i & 0 \\ 0 & i \end{bmatrix} = \frac{1}{\sqrt{2}} \begin{bmatrix} 1 & 1 \\ 1 & -1 \end{bmatrix} \tag{2.1}$$

where $Ph_{\pi/2} = e^{i\frac{\pi}{2}}\mathbf{1}$ applies an overall phase $\pi/2$ to the qubit, $Y_{\pi/2}$ and Z_{π} perform a rotation of $\pi/2$ around y-axis and π aroun z-axis, respectively [15]. This pulse sequence is shown in figure 2.2.

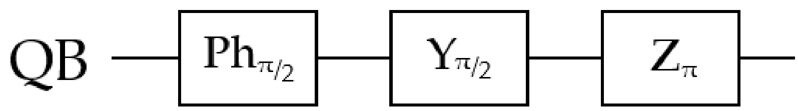

Figure 2.2: Pulse sequence to perform a Hadamard gate. A $\mathrm{Ph}_{\pi/2}$-pulse is applied, followed by a $Y_{\pi/2}$-pulse. Finally, a Z_{π} is applied. .

In figure 2.3, the pulse sequence to perform a Hadamard gate on the Bloch sphere is shown, compared to the action of the undecomposed Hadamard gate.

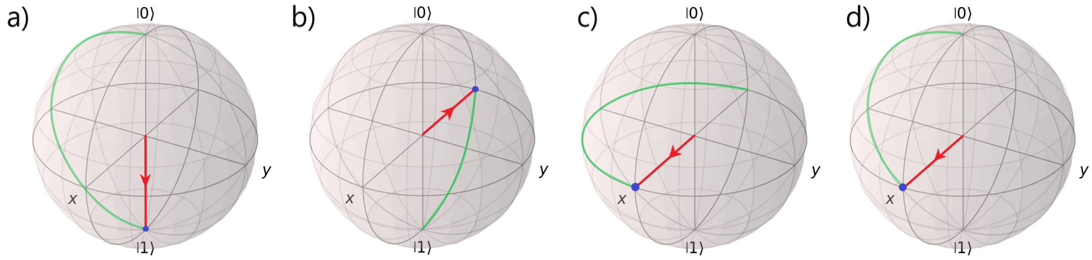

Figure 2.3: In a) the action $Ph_{\pi/2}$ gate; b) the action $Y(\pi/2)$ gate; c) the action $Z(\pi)$; d) the action of the Hadamard gate. The red arrows represent the final state, while the green lines are the gate trajectories. The panels a), b) and c) together constitute the Hadamard gate, shown in panel d).

2.2 Single-qubit gates optimization protocols

In order to implement accurate gates [41], it is necessary to calibrate the pulse drive and to address decoherence effects. Single-qubit gate optimization protocols, like *Rabi oscillations*, *Ramsey interferometry*, *AllXY* are required [14].

2.2.1 Rabi oscillations

One of the fundamental measurements is the observation of Rabi oscillations, which allows us to estimate the so-called π-pulse duration, which is the duration of the drive pulse needed to excite the qubit from $|0\rangle$ to $|1\rangle$. In this experiment, a microwave tone resonant with the qubit frequency is applied to the qubit, resulting in a rotation by some angle around the x or y-axis of the Bloch sphere. As a function of that angle, the Z-Projective measurement of the qubit state will oscillate, so as the probability of being in the excited state after the pulse [42]:

$$P = \frac{\omega_d^2}{\omega_d^2 + \Delta^2} \sin^2 (t\Omega_R), \tag{2.2}$$

where ω_d is the frequency of the drive tone, Δ is the detuning between the drive tone frequency and the qubit frequency, $\Delta = |\omega_d - \omega_q|$, and $\Omega_R = \sqrt{\Delta^2 + \omega_d^2}/2$ is the Rabi frequency [42]. The pulse sequence of a Rabi experiment is shown in figure 2.4.

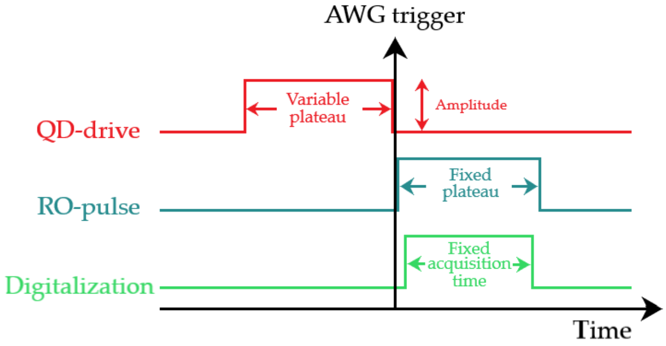

Figure 2.4: Pulse sequence used to measure Rabi oscillations.

In order to measure the Rabi oscillations, the drive signal is followed by a readout signal sent to the readout resonator. The readout and digitalization of the output must occur simultaneously. Indeed, we construct a sequence in which the digitizing pulse falls within the readout excitation pulse. It is fundamental to carefully choose the trigger so that all these signals are aligned. Typically, the power of the drive tone (i.e. the amplitude) is fixed, while its duration, called *plateau*, is variable. The oscillatory behavior of a Rabi measurement, shown in figure 2.5, is obtained by varying the duration of the drive pulse and has an half period which represents the π-pulse.

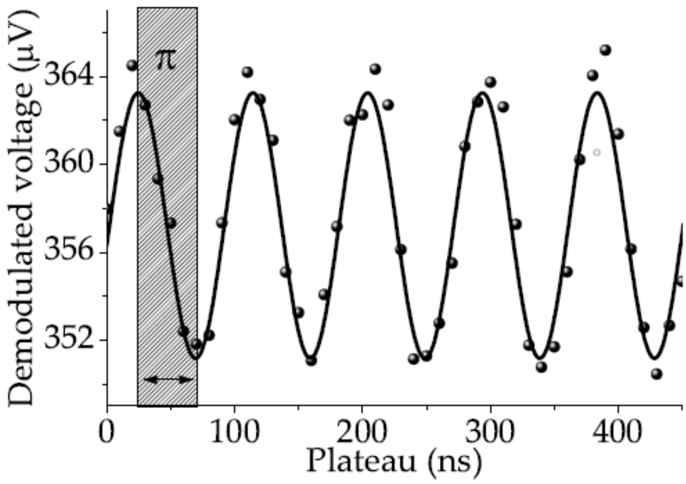

Figure 2.5: Rabi oscillations. It is highlighted the π-pulse, defined as the half period of Rabi oscillations [43].

Additionally, by changing the frequency of the drive pulse tone and therefore the detuning Δ, the Rabi oscillations change both the periodicity and the amplitude. This behavior is visible in the so-called Chevron plots in figure 2.6.

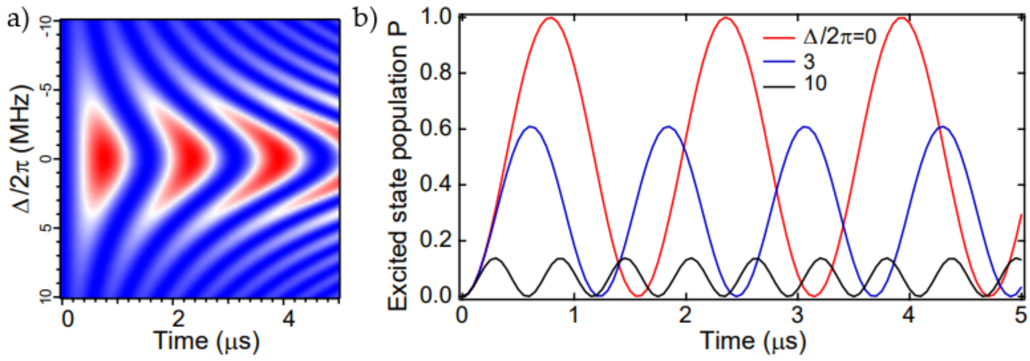

Figure 2.6: In a) the Chevron plot of the excited state population as a function of time and detuning Δ; b) three cuts from the Chevron plot at different detuning values [44].

More in detail, in figure 2.6a) it is shown the excited state population as a function of the time and detuning Δ. It is clear that if the detuning increases, the amplitude of the Rabi oscillations decreases and their frequency increases. This is more evident in figure 2.6b), where there are three cuts from the Chevron plot, showing the Rabi oscillations as a function of the drive pulse time for fixed values of the detuning. Therefore, the frequency of the drive signal must be chosen to have the maximum population probability. Furthermore, the power of the drive RF signal influences the π-pulse duration, which should be as short as possible to have the largest number of gates implemented within the coherence time of the qubit [45]. If the power increases, the Rabi oscillations become faster and consequently the π-pulse is shorter [44]. However, large drive powers can lead to higher-order transitions, affecting the quality of the gate [46]. Therefore we must find a compromise in the choice of the π-pulse power.

2.2.2 Ramsey Interferometry

Another typical time-domain protocol used for the study of the quality of a qubit is Ramsey interferometry [15]. The measurement consists in preparing the qubit on the equator sending a $\pi/2$-pulse, i.e., with half π-pulse amplitude. Then, we wait for a variable amount of time before another $\pi/2$-pulse is used to bring the qubit in the excited state. This pulse sequence is shown in figure 2.7.

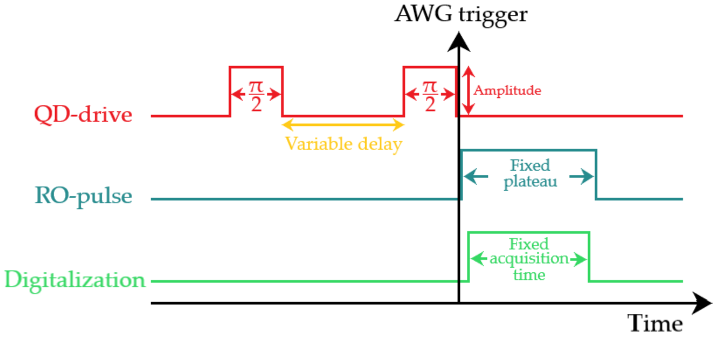

Figure 2.7: Pulse sequence used to measure the dephasing time T_2^*.

The Ramsey output signal is proportional to $\cos{(\delta\omega t)}e^{\Gamma_2^* t}$ [15]. Therefore, if we are off-resonance with the qubit frequency we expect to observe damped oscillations in the demodulated voltage that decay with a characteristic time T_2^*, as shown in figure 2.8.

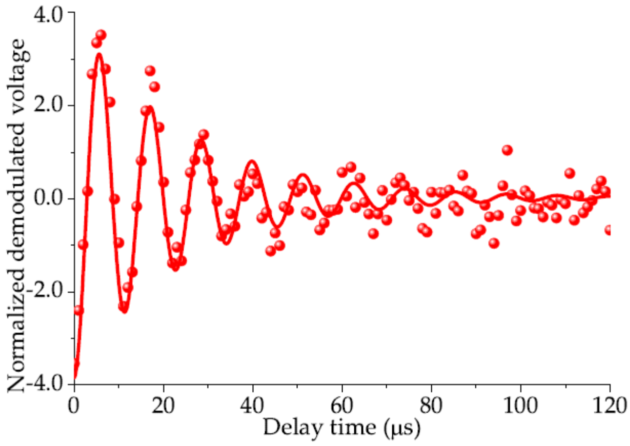

Figure 2.8: Measured exponential cosinusoidal convolution of the demodulated signal magnitude in a Ramsey experiment [43].

The * stands for the fact that the Ramsey experiment is sensitive to *inhomogeneous broadening*, i.e. it is highly sensitive to quasistatic, low-frequency fluctuations [15]. The period of these oscillations corresponds to the detuning $\delta\omega$. These oscillations reduce to a pure exponential decay if $\delta\omega = 0$. Indeed, Ramsey interferometry is used to calibrate the drive frequency, in order to resonate with the qubit frequency [47]. The on-resonance qubit frequency is determined as the center of the Ramsey fringes, as shown by an example in figure 2.9 in terms of the qubit population.

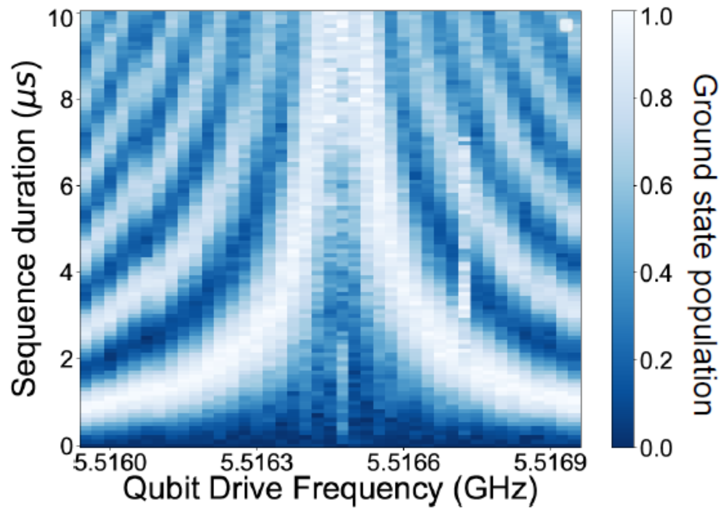

Figure 2.9: An example of Ramsey fringes from interferometry experiment, fundamental for the optimization of qubit drive frequency signal [47]. The plot shows the population of the ground state as a function of the qubit drive frequency and the sequence duration.

2.3 Optimization of the drive pulse shape: the DRAG scheme

In Section 1.5 we have implicitly assumed that it is possible to ignore the higher energy level of the transmon qubit. However, the difference between ω_{01} and ω_{12} is the anharmonicity α (equation 1.11), which is negative and typically around $200MHz$ to $300MHz$ for transmon qubit [15]. Such a low value of anharmonicity leads to leakage errors, which take the qubit out of the computational subspace, and phase errors. The first effect occurs when the qubit is excited to $|2\rangle$ by applying a π pulse to $|1\rangle$ state or directly from $|0\rangle$ state. The second effect occurs because of the repulsion between $|1\rangle$ and $|2\rangle$ levels, due to the presence of the drive pulse. This leads to the accumulation of a relative phase between $|0\rangle$ and $|1\rangle$. In order to address these issues, it is possible to implement the so-called *DRAG* scheme (Derivative Reduction by Adiabatic Gate). According to this procedure, it is applied an extra signal in the Q component. The waveform $s(t)$ in equation 1.23 is modified as:

$$s(t) \rightarrow s'(t) = \begin{cases} s(t) \text{ on I} \\ \lambda \frac{\dot{s(t)}}{\alpha} \text{ on Q} \end{cases} \tag{2.3}$$

where λ is a dimensionless scaling parameter and $\dot{s(t)}$ is the time derivative of $s(t)$ [15]. Theoretically, the best choice to reduce dephasing errors is $\lambda = 0.5$, while the

best choice to reduce leakage errors is $\lambda = 1$ [37] [38]. In practice there can be a deviation from these two optimal values, often due to pulse distortions in the lines which control the qubits. The $\lambda = 0.5, 1$ tradeoff was unambiguously demonstrated in [39] [40]. Therefore, by improving the DRAG scheme it is possible to reduce both errors simultaneously.
The effect of the DRAG procedure can be seen on the Bloch sphere. The waveform of an $X(\pi)$-pulse without DRAG modulation is shown in Figure 2.10a).

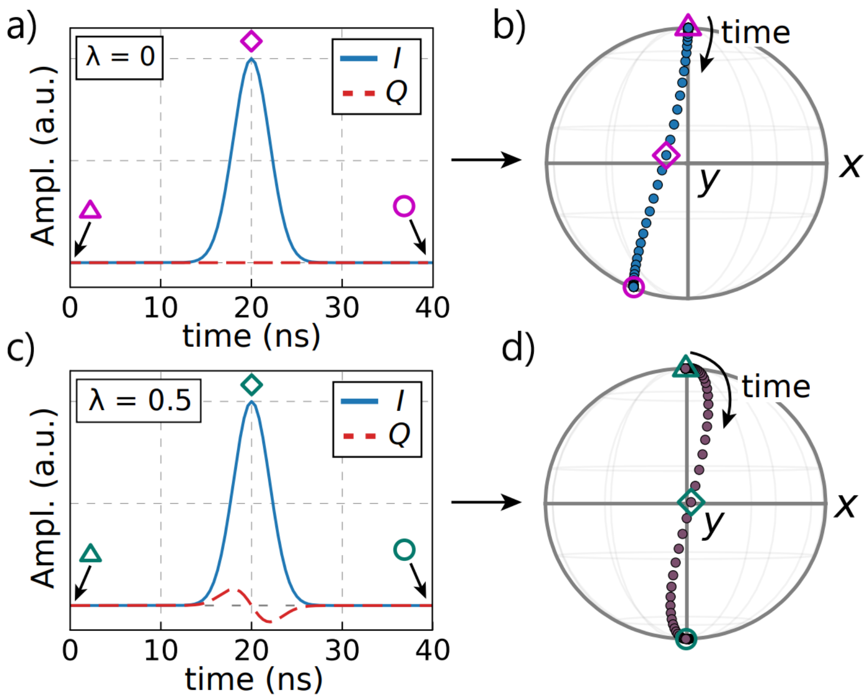

Figure 2.10: In a) waveform of a $X(\pi)$ pulse without DRAG (Derivative Reduction by Adiabatic Gate) modulation; b) effect of the waveform from a) on a qubit initialized in the $|0\rangle$ state. The dephasing error is visible as a deviation from the $|1\rangle$ after the pulse; c) waveform of a $X(\pi)$ pulse with DRAG modulation for $\lambda = 0.5$ to cancel dephasing errors; d) effect of the waveform from c) on the same qubit as b). Figure adapted from [15].

Due to the dephasing error, there will be a deviation from the $|1\rangle$ state after the pulse (Figure 2.10b)). Improving the DRAG scheme for $\lambda = 0.5$, the Q component of the $X(\pi)$ pulse assumes the shape shown in Figure 2.10c). As a result, the dephasing error is corrected, as shown in Figure 2.10d).

2.3.1 AllXY

Rabi and Ramsey calibrations are adequate tune-ups for most basic single-qubit experiments. However, higher-quality rotations are often desirable for applications where achieving a high fidelity value is the goal, such as for algorithms [48] and state tomography [49].

In order to calibrate gate operations more accurately the AllXY protocol is used [14]. This protocol involves different combinations of one or two single-qubit gates, i.e., rotations around x or y-axis by an angle of $\pi/2$ or π. Each pulse combination is sensitive to a different type of error, resulting in a deviation from the ideal response. These deviations are captured in the error syndrome [14].

By analyzing the error syndrome, it is possible to identify the nature and characteristics of the errors affecting the system [14]. In figure 2.11 there are 21 different pulse combinations with their error syndrome.

Ideal $\langle z \rangle$	First pulse	Second pulse	Power dependence	Detuning dependence
1	Id	Id	1	1
1	$X(\pi)$	$X(\pi)$	$1-8\epsilon^2+\mathcal{O}(\epsilon^4)$	$1-\frac{\pi^2\epsilon^4}{32}+\mathcal{O}(\epsilon^6)$
1	$Y(\pi)$	$Y(\pi)$	$1-8\epsilon^2+\mathcal{O}(\epsilon^4)$	$1-\frac{\pi^2\epsilon^4}{32}+\mathcal{O}(\epsilon^6)$
1	$X(\pi)$	$Y(\pi)$	$1-4\epsilon^2+\mathcal{O}(\epsilon^4)$	$1-\epsilon^2+\mathcal{O}(\epsilon^3)$
1	$Y(\pi)$	$X(\pi)$	$1-4\epsilon^2+\mathcal{O}(\epsilon^4)$	$1-\epsilon^2-\mathcal{O}(\epsilon^3)$
0	$X(\pi/2)$	Id	$-\epsilon+\mathcal{O}(\epsilon^3)$	$(1-\frac{\pi}{2})\epsilon^2-\mathcal{O}(\epsilon^4)$
0	$Y(\pi/2)$	Id	$-\epsilon+\mathcal{O}(\epsilon^3)$	$(1-\frac{\pi}{2})\epsilon^2-\mathcal{O}(\epsilon^4)$
0	$X(\pi/2)$	$Y(\pi/2)$	$\epsilon^2-\mathcal{O}(\epsilon^4)$	$-2\epsilon+\mathcal{O}(\epsilon^3)$
0	$Y(\pi/2)$	$X(\pi/2)$	$\epsilon^2-\mathcal{O}(\epsilon^4)$	$2\epsilon-\mathcal{O}(\epsilon^3)$
0	$X(\pi/2)$	$Y(\pi)$	$\epsilon-\mathcal{O}(\epsilon^3)$	$-\epsilon-\mathcal{O}(\epsilon^2)$
0	$Y(\pi/2)$	$X(\pi)$	$\epsilon-\mathcal{O}(\epsilon^3)$	$\epsilon-\mathcal{O}(\epsilon^2)$
0	$X(\pi)$	$Y(\pi/2)$	$\epsilon-\mathcal{O}(\epsilon^3)$	$-\epsilon-\mathcal{O}(\epsilon^2)$
0	$Y(\pi)$	$X(\pi/2)$	$\epsilon-\mathcal{O}(\epsilon^3)$	$\epsilon-\mathcal{O}(\epsilon^2)$
0	$X(\pi/2)$	$X(\pi)$	$3\epsilon-\mathcal{O}(\epsilon^3)$	$\frac{3\pi\epsilon^2}{8}+\mathcal{O}(\epsilon^4)$
0	$X(\pi)$	$X(\pi/2)$	$3\epsilon-\mathcal{O}(\epsilon^3)$	$\frac{3\pi\epsilon^2}{8}+\mathcal{O}(\epsilon^4)$
0	$Y(\pi/2)$	$Y(\pi)$	$3\epsilon-\mathcal{O}(\epsilon^3)$	$\frac{3\pi\epsilon^2}{8}+\mathcal{O}(\epsilon^4)$
0	$Y(\pi)$	$Y(\pi/2)$	$3\epsilon-\mathcal{O}(\epsilon^3)$	$\frac{3\pi\epsilon^2}{8}+\mathcal{O}(\epsilon^4)$
-1	$X(\pi)$	Id	$-1+2\epsilon^2+\mathcal{O}(\epsilon^4)$	$-1+\frac{\epsilon^2}{2}+\mathcal{O}(\epsilon^4)$
-1	$Y(\pi)$	Id	$-1+2\epsilon^2+\mathcal{O}(\epsilon^4)$	$-1+\frac{\epsilon^2}{2}+\mathcal{O}(\epsilon^4)$
-1	$X(\pi/2)$	$X(\pi/2)$	$-1+2\epsilon^2+\mathcal{O}(\epsilon^4)$	$-1+2\epsilon^2+\mathcal{O}(\epsilon^4)$
-1	$Y(\pi/2)$	$Y(\pi/2)$	$-1+2\epsilon^2+\mathcal{O}(\epsilon^4)$	$-1+2\epsilon^2+\mathcal{O}(\epsilon^4)$

Figure 2.11: AllXY pulse sequences. The first and second pulse are listed and ordered according to where the qubit should ideally end up (on the north pole, equator, or south pole of the Bloch sphere, as shown in the first column). The analytically calculated leading-order power and detuning error dependences of the qubit z-projection are reported in the last two columns, respectively. [14].

The pairs of gates are ordered according to the expected final position of the qubit on the Bloch sphere. First, the pulses that should return the qubit to the ground state are considered (Ideal $\langle z \rangle$ = 1), followed by those that should place it on the equator (Ideal $\langle z \rangle$ = 0), and finally those that should end up on the excited state (Ideal $\langle z \rangle$ = -1). Since pulses ending on the north or the south pole of the Bloch sphere are relatively insensitive to errors, the most significant information is given by pulses that end up on the equator [14]. The latter are ordered by their sensitivity to over-rotations, starting from being second-order sensitive to the rotation angle to being several times as sensitive as normal $\pi/2$ rotation. For example, a $X(\pi/2)$ followed by a $X(\pi)$ rotation is three times more sensitive to over-rotations compared to a single $X(\pi/2)$ rotation. Instead, the combination of a $X(\pi/2)$ and a $Y(\pi)$ is only as sensitive as $X(\pi/2)$ pulse, because the Y pulse will not rotate the qubit since it will be in an eigenstate of that operation. Rotations that end up on the north or south pole of the Bloch sphere are second-order sensitive because the expected value of z is proportional to the cosine of the angle. By ordering the pulses according to sensitivity to over-rotations, too much or too little power yields a characteristic "step" pattern, shown in figure 2.12.

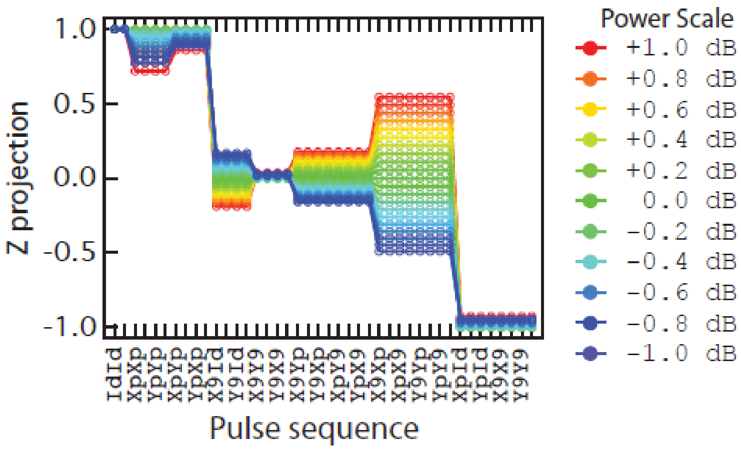

Figure 2.12: Simulated syndromes for amplitude. A calculation using unitary matrix evolution for each type of error is shown. Each error signature is distinct, making it possible to detect several error syndromes simultaneously [14].

The remaining order is given by first X rotations then Y rotations in the first pulse position. This is helpful because the two axes feel the opposite effect of detuning, giving a zig-zag pattern to detuning and the *X scale factor*, used to compensate for phase errors due to the presence of higher excited-state levels [50]. These phase errors are mainly due to two more sources of mixer imperfections, such as amplitude imbalance and skewness. These trends are shown in figure 2.13a) and 2.13b), respectively.

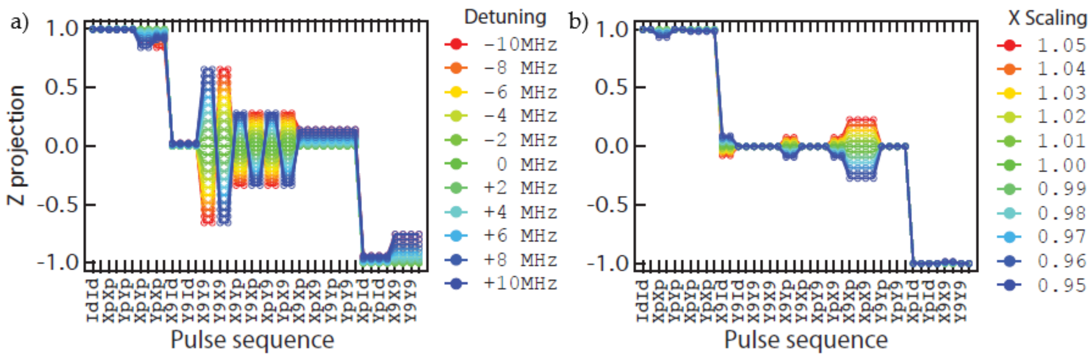

Figure 2.13: Simulated syndromes for a) detuning and b) skew-type error [14].

Syndromes are related to several physical phenomena (e.g. reflections) and, since they are linearly independent, single-qubit pulse errors can be quickly identified. In addition to the syndromes shown in figure 2.12 and 2.13, another syndrome not easily calculated but nevertheless crucial to tuning up pulses is associated with DRAG [50][51]. The lowest-order correction involves either continuously detuning the pulse as a function of its instantaneous amplitude or adding a copy of the derivative of the primary pulse to its orthogonal quadrature. In both cases, there is a scale factor for this correction. It is tuned up as a free parameter based on the observation of its syndrome in AllXY, shown in figure 2.14.

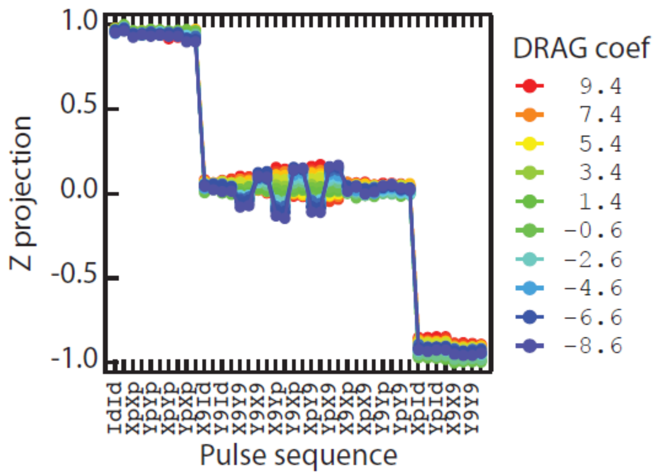

Figure 2.14: The error syndromes associated with DRAG (Derivative Reduction by Adiabatic Gate) coefficient [14].

In order to efficiently tune-up the DRAG parameter, we take two of the AllXY pulses which exhibit the opposite sign of error and we implement them on the hardware as a function of the DRAG coefficient. This yields two lines that cross at the point where the parameter is optimal. In figure 2.15 this procedure is implemented for the combinations $Y(\pi)X(\pi/2)$ and $X(\pi)Y(\pi/2)$.

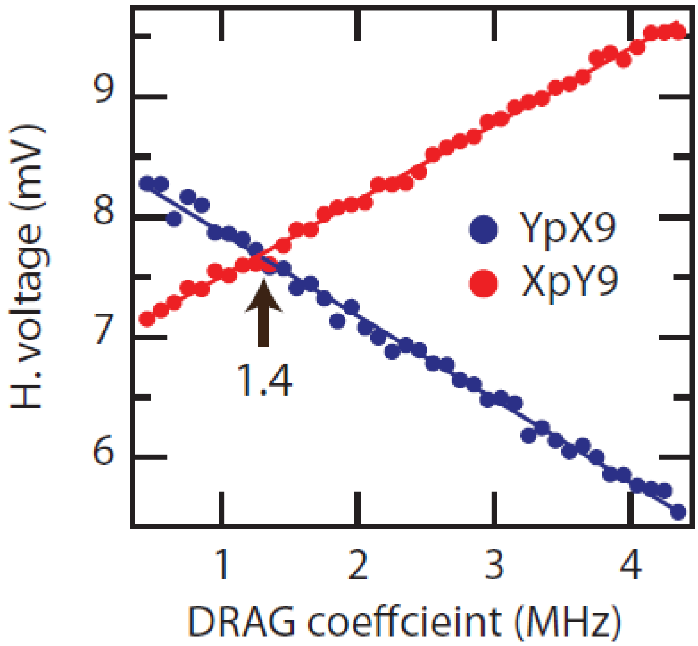

Figure 2.15: Intersection of the two lines obtained by varying the DRAG (Derivative Reduction by Adiabatic Gate) coefficient of gates combination with opposite syndrome sign. This intersection represents the optimal DRAG coefficient value [14].

2.4 Fidelity and decoherence time evolution

The evaluation of the performance of the single-qubit gates is a key study in the implementation of superconducting quantum processors. Therefore, the scientific community introduced the state and the gate fidelity to quantify the quality of the qubit performances [41]. The state fidelity measures the distinguishability of two quantum states, ρ and σ, where ρ is the experimental quantum state density matrix and σ is its theoretical expectation.

The fidelity is defined as [52]:

$$\mathcal{F}(\rho,\sigma) = Tr\left[\sqrt{\sqrt{\rho}\sigma\sqrt{\rho}}\right]^2, \tag{2.4}$$

i.e. it measures the deviation of an experimental quantum state from the theoretical expectation. If $\rho = |\psi\rangle\langle\psi|$ and $\sigma = |\varphi\rangle\langle\varphi|$ are both pure states, then $\mathcal{F} = |\langle\psi|\varphi\rangle|^2$ becomes the standard definition of quantum probability. Specifically, if the state $|\varphi\rangle$ exactly corresponds to $|\psi\rangle$, the fidelity approaches the limit value of 1, i.e. the probability of measuring $|\varphi\rangle$ after its preparation is equal to 100%. In addition to state fidelity, we can define the gate fidelity as [53]:

$$\mathcal{F}(\hat{U},\hat{\Lambda}_U) = \int d\rho F(U\rho U^\dagger, \hat{\Lambda}_U(\rho)), \tag{2.5}$$

where U represents an ideal unitary gate, $U^\dagger$ its Hermitian adjoint and $\Lambda_U(\rho)$ the imperfect realization of the gate. It measures how closely the actual gate operation performed on the qubit matches the ideal or desired gate operation. The gate fidelity is intrinsically limited by the coherence time of superconducting qubits, which is characteristic of the processor employed, and this influences the choice of the universal gate set. In general, one wants to keep the overall number of time steps in which gates are applied as low as possible, as well as the number of total gates [15]. This means that in order to minimize the synthetization time, i.e. the time required to decompose an operation, the set is chosen so to maximize the overall calculation efficiency. Some universal quantum gate sets include [15]:

- $\mathcal{G}_0 = \{X_\theta, Y_\theta, Z_\theta, Ph_\theta, CNOT\}$ where $Ph_\theta = e^{i\theta}\mathbb{1}$.
- $\mathcal{G}_1 = \{H, S, T, CNOT\}$ known as *"Clifford + T" set*.

The single-qubit gate fidelity affected by uncorrelated energy relaxation with rate T_1^{-1}, and pure dephasing with rate $T_\phi^{-1} = T_2^{*-1} - (2T_1)^{-1}$, reads as [47][54]:

$$\mathcal{F} = 1 - \frac{1}{3}\tau\Big(T_1^{-1} - T_\phi^{-1}\Big), \tag{2.6}$$

where τ is the mean gate sequence duration. Thus, it is fundamental for qubit control to estimate the characteristic decoherence times of the qubit, discussed in Section 1.6.

2.4.1 T_1 measurement

Once the π-pulse has been calibrated with Rabi oscillations measurement, it is possible to measure the relaxation time T_1 of the qubit (Section 1.6.1). This experiment consists in preparing the qubit in the excited state sending a π-pulse, and then measuring the readout of the qubit state through the readout resonator pulse, changing the so-called *sequence duration*, which is the delay between the preparation of the qubit in the excited state and the acquisition. The pulse sequence of this experiment is shown in figure 2.16.

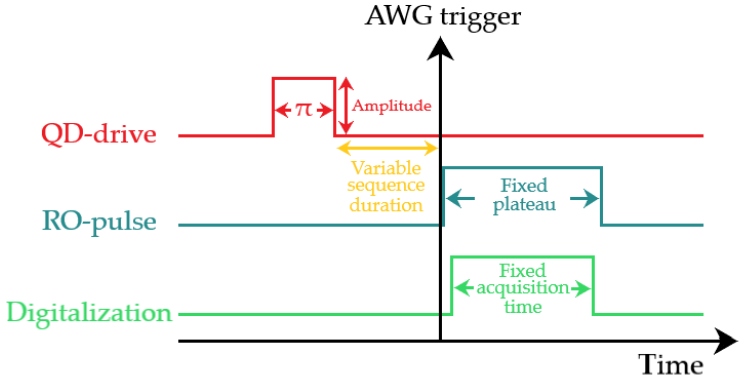

Figure 2.16: Pulse sequence used to measure the relaxation time T_1.

The longer the sequence duration, the higher the probability to decay to the fundamental state. As a consequence, an exponential decay is observed in the demodulated voltage measured as a function of the sequence duration, as shown in figure 2.17.

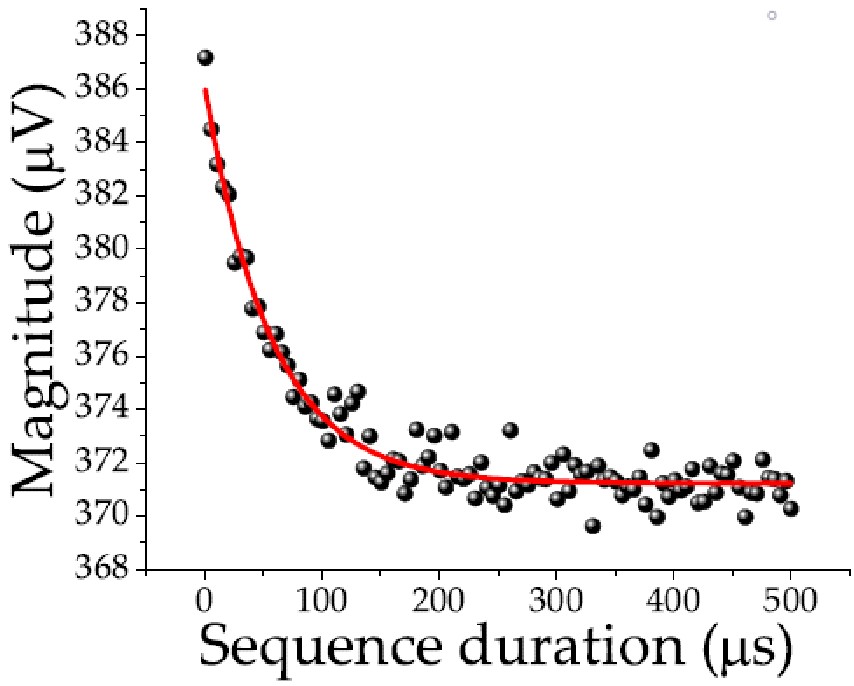

Figure 2.17: Exponential decay in the demodulated voltage measured as a function of the sequence duration [43].

The relaxation time T_1 can be obtained from experimental data through a fitting process, using the function $ae^{-x/T_1} + c$.

2.4.2 Spin Echo protocol

Another common procedure used to characterize qubits is the Hahn echo protocol [15], which allows us to determine the coherence time T_2, described in Section 1.6.3. This experiment is performed using a pulse sequence that is almost the same sequence of Ramsey interferometry, except for an additional π-pulse in the middle of the two $\pi/2$-pulses, as shown in figure 2.18.

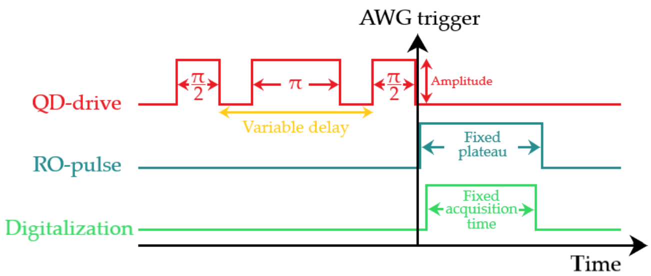

Figure 2.18: Pulse sequence of Spin Echo protocol used to measure T_2.

The π-pulse in the middle is also known as refocusing pulse. Basically, according to the pulse scheme, the qubit is prepared on the equator, then a rotation of π is performed, and finally it is excited to $|1\rangle$ state. By doing so, the quasi-static contributions to dephasing can be suppressed, leaving an estimate of T_2 that is less sensitive to inhomogeneous broadening mechanisms than the T_2^* obtained through the Ramsey protocol [15]. In figure 2.19 it is shown the characteristic exponential decay obtained from the Hanh Echo protocol.

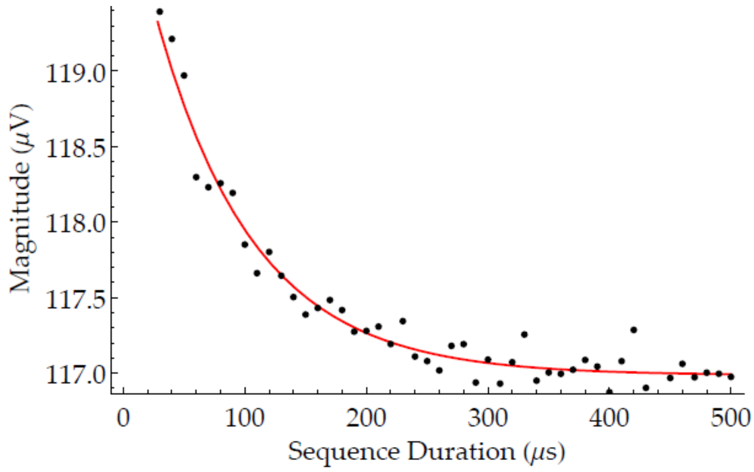

Figure 2.19: Exponential decay measured with a Hanh Echo pulse sequence to estimate T_2 [43].

The coherence time T_2^{Echo} can be obtained from experimental data through a fitting process, using the function $ae^{-x/T_2^{Echo}} + c$. It has been demonstrated that the inclusion of multiple π-pulses in the middle of the Hahn-echo sequence allows to approach the theoretical limit in the absence of dephasing for a qubit, i.e., $T_2 = 2T_1$, in agreement with what has been discussed in Section 1.6.3 [55].

2.5 Two-qubit gates

In gate-based quantum computing, two-qubit gates are generally conditional gates [15]. They take two qubits as inputs; the first is typically called *control* qubit and the second is called *target*. The latter is the one on which the gate is applied, whose action depends on the state of the control qubit. In table 2.1 fundamental two-qubit gates are reported:

- CNOT gate: it flips the state of the target qubit when the control qubit is in the excited state.

- CZ gate: it applies a Z gate on the target qubit when the control qubit is in the excited state. It can also be noticed that CZ is a symmetric gate, since it basically applies an overall phase.

- iSWAP gate: it swaps an excitation between the two qubits.

GATE	CIRCUIT REPRESENTATION	MATRIX REPRESENTATION	TRUTH TABLE	
			Input	Output
CNOT	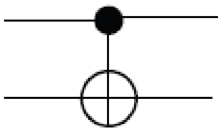	CNOT = $\begin{pmatrix} 1 & 0 & 0 & 0 \\ 0 & 1 & 0 & 0 \\ 0 & 0 & 0 & 1 \\ 0 & 0 & 1 & 0 \end{pmatrix}$	$\|00\rangle$ $\|01\rangle$ $\|10\rangle$ $\|11\rangle$	$\|00\rangle$ $\|01\rangle$ $\|11\rangle$ $\|10\rangle$
			Input	Output
CZ	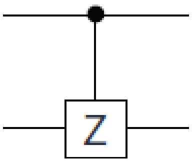	CZ = $\begin{pmatrix} 1 & 0 & 0 & 0 \\ 0 & 1 & 0 & 0 \\ 0 & 0 & 1 & 0 \\ 0 & 0 & 0 & -1 \end{pmatrix}$	$\|00\rangle$ $\|01\rangle$ $\|10\rangle$ $\|11\rangle$	$\|00\rangle$ $\|01\rangle$ $\|10\rangle$ -$\|11\rangle$
			Input	Output
iSWAP		iSWAP = $\begin{pmatrix} 1 & 0 & 0 & 0 \\ 0 & 0 & -i & 0 \\ 0 & -i & 0 & 0 \\ 0 & 0 & 0 & 1 \end{pmatrix}$	$\|00\rangle$ $\|01\rangle$ $\|10\rangle$ $\|11\rangle$	$\|00\rangle$ -$i\|10\rangle$ -$i\|01\rangle$ $\|11\rangle$

Table 2.1: For each two-qubit gate, it is shown the circuit representation, the matrix representation and the truth table. Matrices are defined in the basis $\{|00\rangle, |01\rangle, |10\rangle, |11\rangle\}$, where the first qubit is the control qubit and the second qubit is the target qubit.

2.6 The iSWAP and the CZ gate

The interaction Hamiltonian H_{int} in the total Hamiltonian $H = H_1 + H_2 + H_{int}$ (equation 1.31) can also be written as [15]:

$$H_{int} = J\sigma_{y1} \otimes \sigma_{y2}. \tag{2.7}$$

By means of external flux and the frequency tunability described in Section 1.3, we can tune a qubit to bring it on resonance with the coupled qubit, and equation 2.7 can be rewritten as:

$$H_{int} = \frac{J}{2}(\sigma_{x1}\sigma_{x2} + \sigma_{y1}\sigma_{y2}). \tag{2.8}$$

This equation shows that if two qubits are set on resonance there will be a swap of excitations between them. The unitary matrix that corresponds to this interaction is:

$$U(t) = \begin{bmatrix} 1 & 0 & 0 & 0 \\ 0 & \cos(Jt) & -i\sin(Jt) & 0 \\ 0 & -i\sin(Jt) & \cos(Jt) & 0 \\ 0 & 0 & 0 & 1 \end{bmatrix}. \tag{2.9}$$

If the qubits are tuned on resonance for a time $t = \pi/2J$, the coupling allows to implement the $iSWAP$ shown in table 2.1:

$$U(t = \pi/2J) = \begin{bmatrix} 1 & 0 & 0 & 0 \\ 0 & 0 & -i & 0 \\ 0 & -i & 0 & 0 \\ 0 & 0 & 0 & 1 \end{bmatrix} = iSWAP, \tag{2.10}$$

which simultaneously swaps an excitation between the two qubits, and adds a phase of $i = e^{i\pi}/2$ [15].

First of all, in order to perform an iSWAP experiment it is necessary to excite one of the qubit, so that the state of the system is $|10\rangle$. Then we fix the qubit with lower frequency in its sweet spot, while the higher frequency qubit can be tuned, till the two are on resonance. In figure 2.20 it is shown the pulse sequence of the iSWAP experiment.

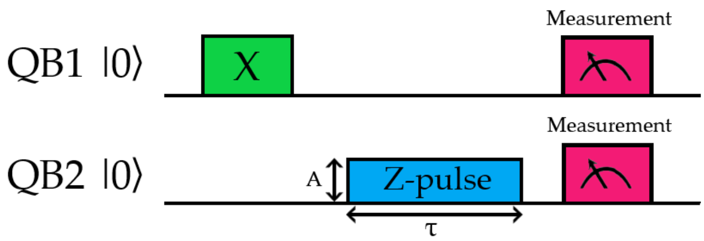

Figure 2.20: Pulse sequence of iSWAP experiment. An X-pulse is applied on qubit 1, so that the system is in $|10\rangle$ state. Then qubit 2 is tuned with a flux pulse for different values of amplitude A and duration of the pulse τ. Finally, a measurement on the qubit state is performed.

The probability to be in the $|01\rangle$ state for different values of the amplitude A and duration of the flux pulse τ on the higher frequency qubit is shown in figure 2.21.

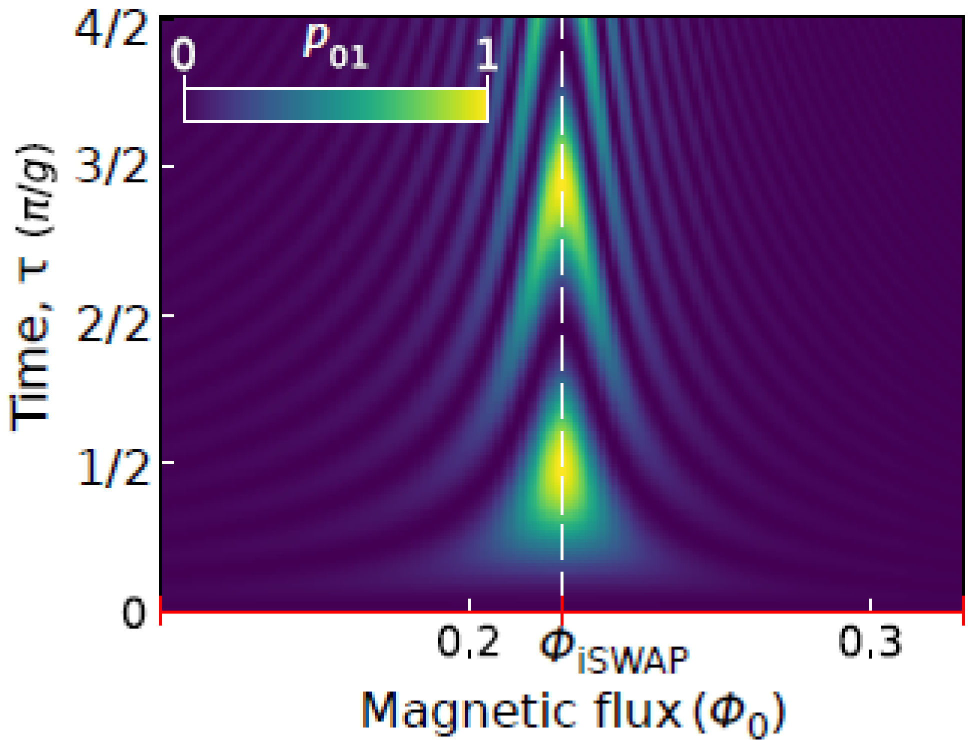

Figure 2.21: Starting from $|10\rangle$ state, it is shown the probability of swapping into the $|01\rangle$ state as a function of the duration and the amplitude of the flux pulse applied. The inspected region is the one for which an avoided level crossing between the $|01\rangle$ state and the $|10\rangle$ state is typically observed [15].

For the iSWAP gate, we assumed that the higher energy levels of the qubit could be neglected. Actually, for a transmon qubit they can be used to implement a CZ gate. Specifically, in order to implement a CZ gate the avoided level crossing must occurr between the $|11\rangle$ and the $|20\rangle$ states [15]. This is easier to understand if we consider the spectrum for two coupled transmon qubits, including levels with higher order excitations, shown in figure 2.22.

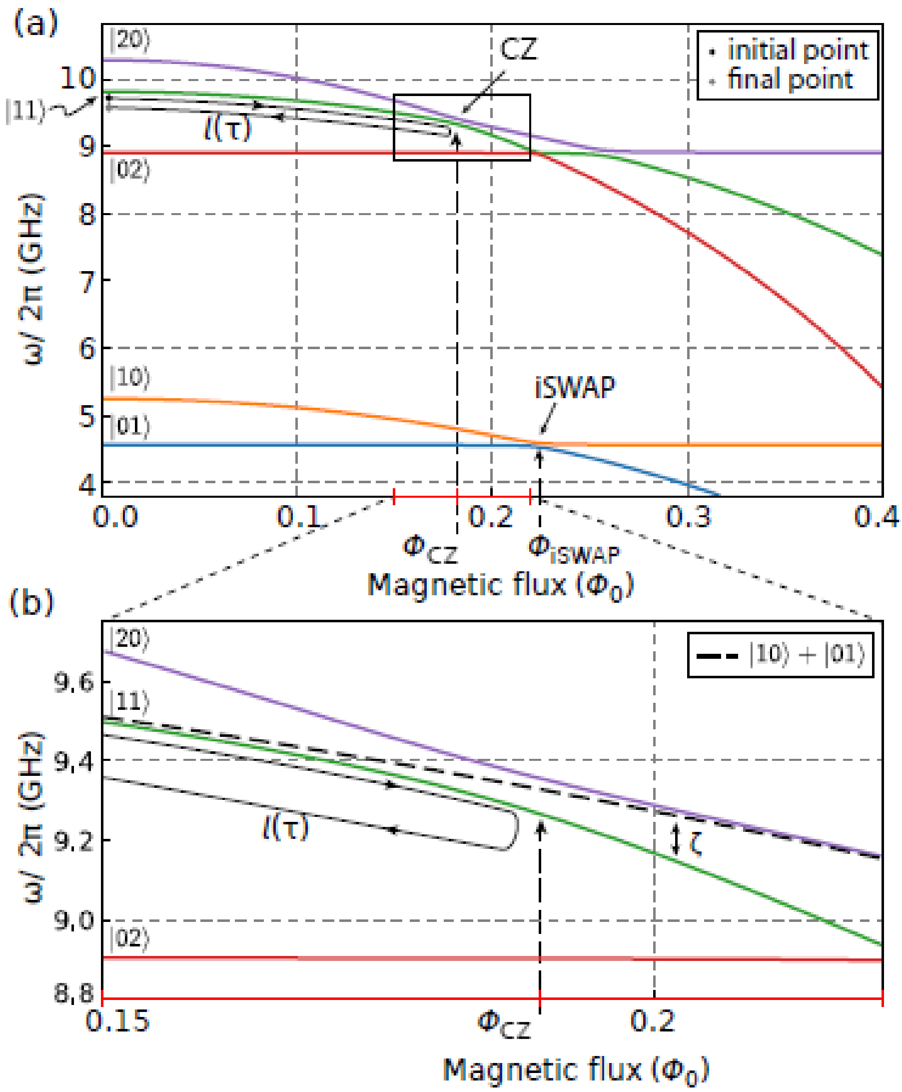

Figure 2.22: (a) Spectrum of two coupled transmon qubits as a function of the local magnetic flux for higher frequency qubit. The two lower branches corresponding to $|01\rangle$ and $|10\rangle$ are involved in the $iSWAP$ gate operation. The avoided crossing indicated in the black rectangle is used to implement the CZ gate. Black line with arrows indicates a typical trajectory used to implement a CPHASE gate (starting at the black circle and ending at the gray circle). (b) Zoom in of the $|20\rangle \leftrightarrow |11\rangle$ avoided crossing highlighted in the black box in (a) at $\Phi = \Phi_{CZ}$. The parameter ζ quantifies the difference in energy between $|11\rangle$ and $|01\rangle + |10\rangle$ and ℓ is the trajectory in (Φ, t)-space [15]

.

The Hamiltonian of the system in the $\{|00\rangle, |01\rangle, |10\rangle, |11\rangle, |02\rangle, |20\rangle\}$-basis is given by:

$$H = \begin{bmatrix} E_{00} & 0 & 0 & 0 & 0 & 0 \\ 0 & E_{01} & J & 0 & 0 & 0 \\ 0 & g & E_{10} & 0 & 0 & 0 \\ 0 & 0 & 0 & E_{11} & \sqrt{2}J & \sqrt{2}J \\ 0 & 0 & 0 & \sqrt{2}J & E_{02} & 0 \\ 0 & 0 & 0 & \sqrt{2}J & 0 & E_{20} \end{bmatrix} \tag{2.11}$$

where the $\{|02\rangle, |20\rangle \leftrightarrow |11\rangle\}$ transitions are scaled by a factor $\sqrt{2}$ due to the higher photon number [15]. By preparing the system in the state $|11\rangle$ and moving towards the avoided crossing, the resulting unitary operator in the computational basis is given by:

$$U_{ad} = \begin{bmatrix} 1 & 0 & 0 & 0 \\ 0 & e^{i\theta_{01}(\ell)} & 0 & 0 \\ 0 & 0 & e^{i\theta_{10}(\ell)} & 0 \\ 0 & 0 & 0 & e^{i\theta_{11}(\ell)} \end{bmatrix}, \tag{2.12}$$

where $\theta_{ij}(\ell(\tau))$ is the phase acquired by the state $|ij\rangle$ along the trajectory ℓ. In figure 2.22 the movement should be adiabatic, which means that it should occur slowly on the time-scale determined by J. It is possible to define the parameter ζ, also shown in figure 2.22, and the conditional phase as:

$$\zeta = \omega_{11} - \omega_{01} - \omega_{10}, \tag{2.13}$$

$$\theta_{2Q} = \theta_{11} - \theta_{01} - \theta_{10}, \tag{2.14}$$

where the ζ parameter represents the repulsion of the $|11\rangle$ due to the $|20\rangle$ state.
After the adiabatic process, it is possible to apply flux pulses to compensate the phase of single excitation states, so that $\theta_{10}(\ell) = \theta_{01}(\ell) = 0$. If it is chosen a trajectory ℓ_π so that $\theta_{11} = \pi$, the matrix 2.12 becomes:

$$U_{CZ} = \begin{bmatrix} 1 & 0 & 0 & 0 \\ 0 & 1 & 0 & 0 \\ 0 & 0 & 1 & 0 \\ 0 & 0 & 0 & -1 \end{bmatrix}. \tag{2.15}$$

The form of the matrix suggests that the CZ applies an overall phase to the qubits when both are in the excited state.
In order to perform a CZ experiment it is necessary to excite both the qubits, so that the system is in $|11\rangle$ state. As for the iSWAP, we fix the qubit at lower frequency in its flux sweet spot and we tune the higher frequency one, till they are on resonance. The pulse sequence of this experiment is shown in figure 2.23.

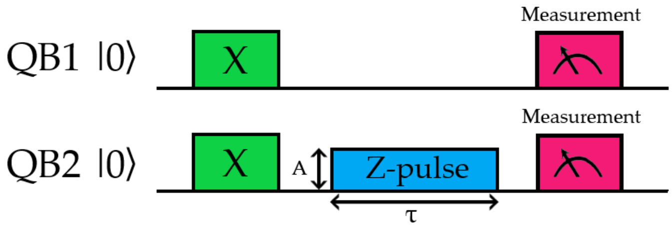

Figure 2.23: Pulse sequence of CZ experiment. An X-pulse is applied both on qubit 1 and qubit 2, so that the state of system is $|11\rangle$. Then qubit 2 is tuned with a flux pulse for differente values of amplitude A and duration of the pulse τ . Finally, a measurement on the qubit state is performed.

In order to tune up the CZ gate, it is possible to perform the conditional oscillation experiment. It can be used to measure the single-qubit phases θ_{01} and θ_{10}, the conditional phase θ_{2Q} acquired during an uncalibrated CZ gate, and to estimate the leakage L, defined as the average probability that a random computational state leaks out of the computational subspace [56]. In the conditional oscillation experiment, two variants of the same experiment are performed [57]. In the first variant (Off), a $\pi/2$-pulse is applied on the target qubit, while the control qubit is left in the ground state. After that, the CZ flux pulse is applied. Finally, another $\pi/2$-pulse is applied on the target before measuring the state of both qubits simultaneously. In the second variant (On), the control qubit is rotated into the excited state before applying the CZ gate. Then, the control qubit is pulsed back to the ground state before measuring both qubits. The pulses scheme is shown in figure 2.24.

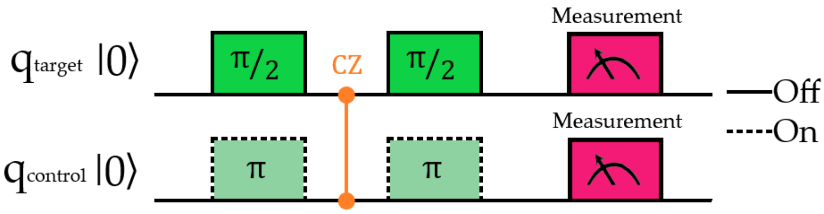

Figure 2.24: Pulse scheme for the conditional oscillation experiment. For the Off variant (solid line), the target is prepared on the equator by a $\pi/2$-pulse, then a CZ gate is performed, followed by another $\pi/2$-pulse. Finally, the states of both qubits are measured simultaneously. For the On variant (dashed line), the pulses on the target are the same as the Off variant, but on the control a π-pulse is applied each time a $\pi/2$-pulse is applied on the target.

The single-qubit phase can be measured by interchanging the roles of the target and control. The difference in phase acquired by the target in the On and Off variants yields θ_{2Q}, as shown in figure 2.25a).

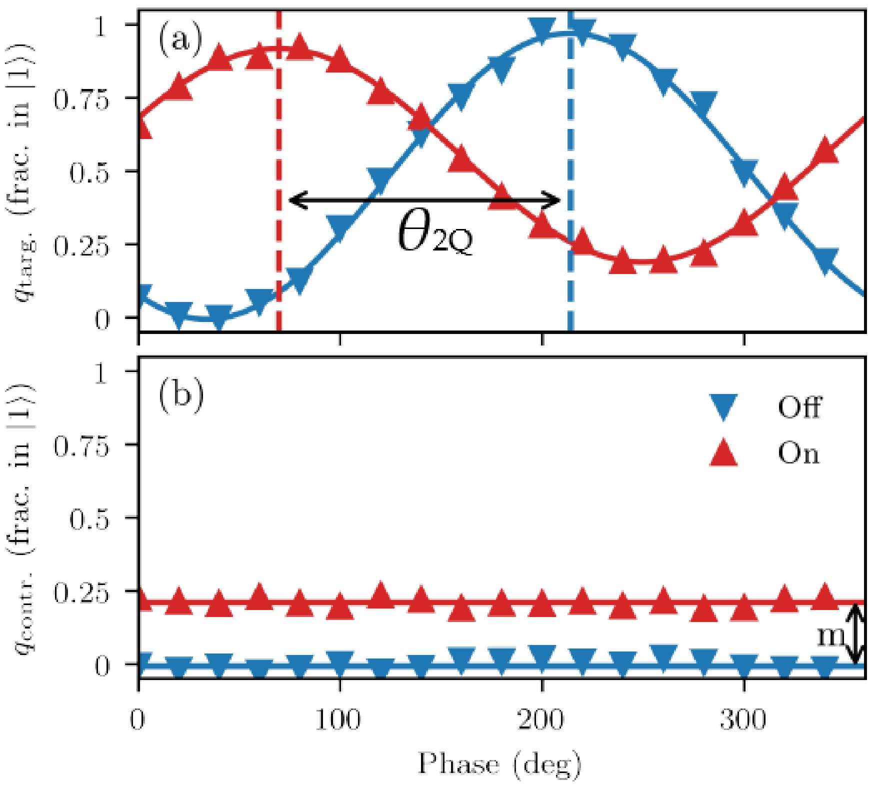

Figure 2.25: Conditional oscillation experiment. In figure a), the population of the state for the target qubit as a function of the phase is shown. The conditional phase θ_{2Q} is also highlighted. In figure b) it is shown the population of the state for the control qubit as a function of the phase. The m represents the missing fraction, used to estimate the leakage [57].

In figure 2.25b) it is shown the population difference on the control between both the variants of the experiment, defined as the missing fraction m. It allows us to estimate the leakage as $L = m/2$. In order to optimize θ_{2Q}, i.e. to have it equal to π, and to minimize the leakage, the flux pulse amplitude and duration are changed, so as the shape of the pulse [58].

2.7 The CNOT gate

The CNOT can be implemented by using both CZ and iSWAP gates [15]. By including two Hadamard gates the CNOT unitary matrix reads as:

$$U_{CNOT} = (1 \otimes H)U_{CZ}(1 \otimes H), \tag{2.16}$$

since $U_{CNOT} = |0\rangle\langle 0| \otimes \mathbb{1} + |1\rangle\langle 1| \otimes \mathbf{X}$, $U_{CZ} = |0\rangle\langle 0| \otimes \mathbb{1} + |1\rangle\langle 1| \otimes \mathbf{Z}$ and $\mathbf{HZH} = \mathbf{X}$. In figure 2.26 it is shown the circuit diagram of the CNOT in terms of a CZ.

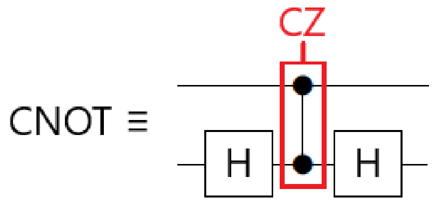

Figure 2.26: Circuit diagram of the CNOT in terms of CZ. The pulse sequence is composed of a Hadamard on target, a CZ, which is simmetric, and finally another Hadarmad on target. Figure adapted from [15].

The CNOT gate can also be implemented by stringing together two iSWAPs and several single-qubit gates, as shown in figure 2.27.

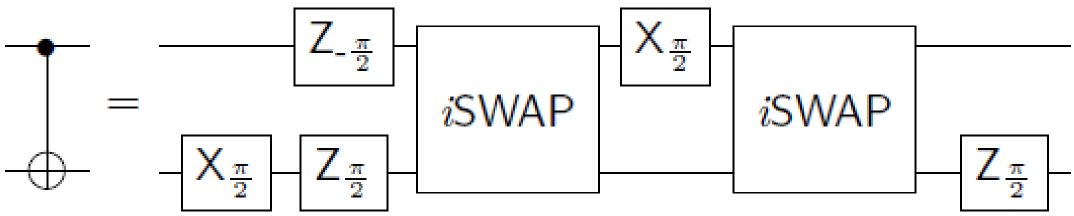

Figure 2.27: Circuit diagram of the CNOT in terms of iSWAP. The pulse sequence is composed of a $X(\pi/2)$ on target, a $Z(\pi/2)$ on target and simultaneously a $Z(-\pi/2)$ on control, an iSWAP, a $X(\pi/2)$ on control, another iSWAP, and finally a $Z(\pi/2)$ on target [15].

However, for this thesis, the first implementation with the CZ gate has been employed. The CNOT gate is called *entangling gate*, because its output state can be entangled even if the input is a separable state [15]. For example, consider two qubits A and B in the state:

$$|\psi\rangle = \frac{1}{\sqrt{2}}(|0\rangle + |1\rangle)_A |1\rangle_B \,. \tag{2.17}$$

If a CNOT gate is applied to $|\psi\rangle$, the resulting state is (table 2.1):

$$U_{CNOT} = \frac{1}{\sqrt{2}}(|0\rangle_A |1\rangle_B + |1\rangle_A |0\rangle_B) \neq (...)_A(...)_B. \tag{2.18}$$

This state is called *Bell state* and represents the simplest and maximal example of quantum entanglement [59]. Therefore, the $CNOT$ gate plays a fundamental role in quantum computation. It is important not only for creating entangled states but also for constructing quantum circuits, as it will be shown in Chapter 4. Furthermore, multiple $CNOT$ gates can be combined to perform universal quantum computation, enabling the implementation of a wide range of quantum algorithms and protocols [60].

2.8 Multiplexed single-shot readout

The last part of each protocol is the measurement of the qubit state, which is an essential feature of any quantum computer. Specifically, high-fidelity single-shot measurements are needed for determining the result of quantum computation [61], observing error syndromes in quantum error correction [62][63] and for achieving high channel capacity in quantum communication protocols such as quantum teleportation [64][65]. Moreover, quantum non-demolition measurements are used for conditioning quantum state initialization [66][67][68].
Recent progress in scaling up quantum processors based on superconducting qubits has stimulated research toward multiplexed readout architectures with the goal of reducing device complexity and enhancing resource efficiency [69][70][71]. Extensions of dispersive readout to multiple qubits can be realized by either coupling multiple qubits to a single readout resonator [72][73] or by probing several readout resonators coupled to a single feedline with a multifrequency pulse [69]. The latter approach allows for selective readout of any subset of qubits by choosing the corresponding readout frequency components in the measurement operation.
Frequency multiplexing can be used to measure the quantum states of several qubits in a single shot. Simultaneous readout of the multiple qubits provides probability distributions of multiple qubit systems, i.e., $|00\rangle$, $|01\rangle$, $|10\rangle$ and $|11\rangle$ for two-qubit states, by repeating the single-shot measurements. We quantify the performance of single-shot readout for each qubit by preparing the qubit in either the ground or the excited state and later applying a readout pulse at the corresponding readout resonator frequency. These measurements result in two Gaussian distributions, as shown in figure 2.28.

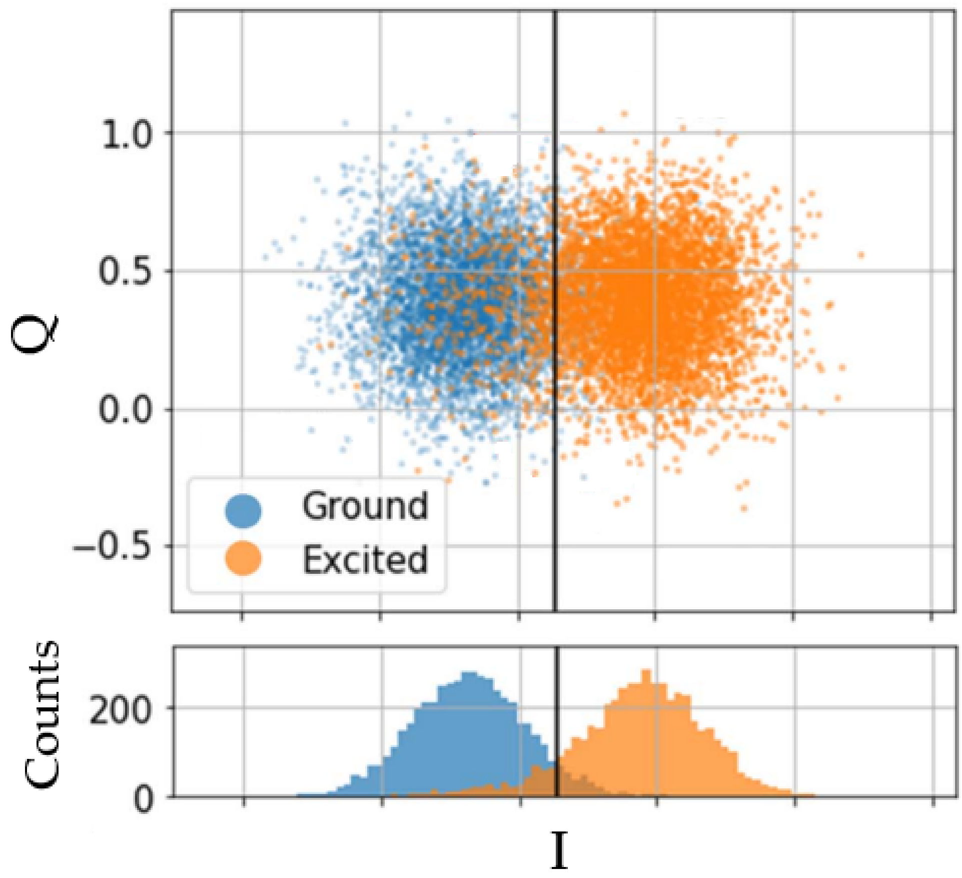

Figure 2.28: Frequency-multiplexed single-shot readout data on the IQ plane. Blue and orange dots are measured when the qubit is prepared in the ground and in the excited state, respectively. The black solid line represents the discriminator that allows for the maximum readout fidelity. Figure adapted from [74].

In order to assign a binary value corresponding to the outcome of the qubit measurement, we choose an assignment threshold, which best separates the prepared states of the qubit [74]. We quantify the fidelity of the readout by the correct assignment probability $P_c = [P(g|0) + P(e|\pi)]/2$, where π and 0 marks the state preparation with and without a π-pulse, respectively, while e and g stands for the qubit assigned as in excited and ground state, respectively. The single-shot histogram in figure 2.28 provides information on the sources of readout error [75]. First of all, due to finite SNR (Signal to Noise Ratio), the two states cannot be fully distinguished because of the overlap of the two Gaussians. Furthermore, when prepared in the excited state, the qubit may decay before or during the readout, which accounts for the remainder of the observed errors.

Chapter 3

Experimental set-up

3.1 Cryogenic system

In order to characterize and analyse superconducting quantum devices it is fundamental to thermalise them to values well below its critical temperature T_c, that for standard supercondutors in quantum devices is of the order of a few Kelvins [12]. Therefore, cryogenic systems are required in order to achieve the superconducting regime. Moreover, it is also necessary to minimise the effects of thermal noise during the measurements. In fact, thermal energy can lead to undesired transitions between energy levels separated by an energy below $k_B T$, where k_B is the Boltzmann constant and T is the electronic temperature. Specifically for superconducting qubits, if they are sufficiently below the temperature $T = \hbar\omega_{01}/k_B$, transitions between the two computational levels $|0\rangle$ and $|1\rangle$ due thermal fluctuations can be safely neglected.
The dilution fridge is a device capable of reaching temperature near absolute zero through cold temperature technology based on the thermodynamic properties of a mixture of $^3He -^4 He$ [76]. Below $800mK$, the separation of the mixture in a concentrated phase of ^3He and a diluted phase of ^3He allows to reach temperatures of about $10mK$, according to the phase diagram shown in figure 3.1.

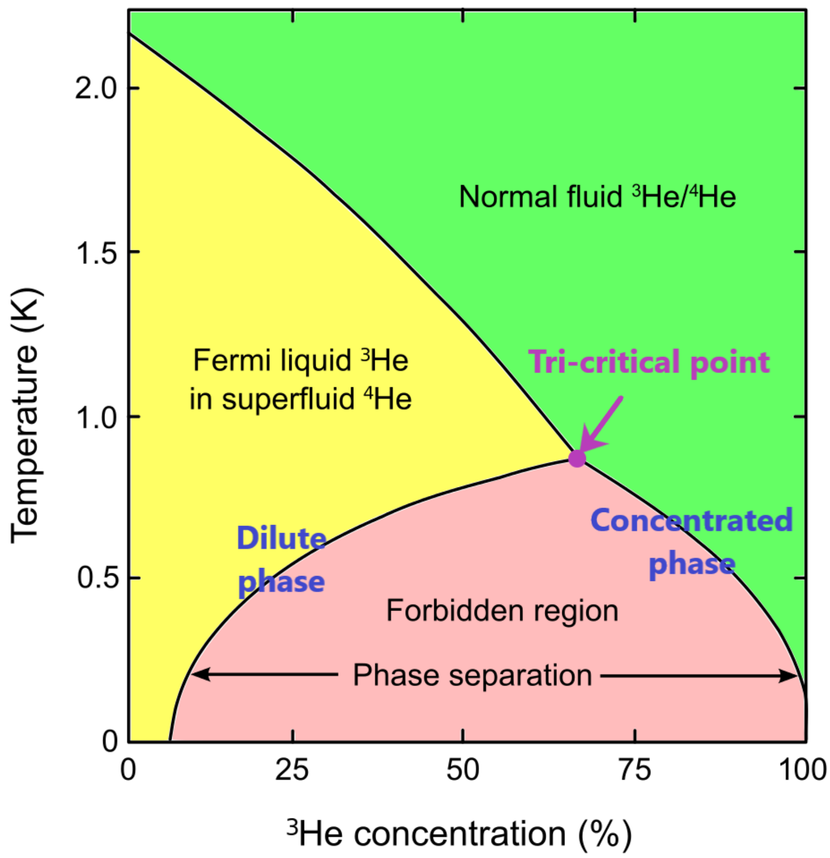

Figure 3.1: Phase diagram of ^3He and ^4He in terms of temperature and ^3He concentration of the mixture.

The feature that allows to distinguish dilution cryostats from one to another is the way they reach the mixture temperature of around $4-10K$, i.e., at the precooling stage. From this point of view, cryostats can be divided into two main categories: wet cryostats and dry cryostats. The wet type exploits an ^4He bath to reach the pre-cool temperature of the order of $4.2K$. The dry cryostats, instead, make use of a compressor, called *pulse tube refrigerator*, which cools down the mixture through a sequence of compressions that brings the system to a temperature of $10K$. Later, the mixture is passed through a sequence of pressure impedances that exploits the Joule-Thompson effect to lower the temperature of the mixture to values of the order of $1K$.
The dilution fridge employed in this thesis work is the dry *Triton 400* of the Oxford Instruments. Its structure is shown in figure 3.2.
It is composed of two units: *pre-cool unit* and *dilution unit*. The pre-cool unit is placed

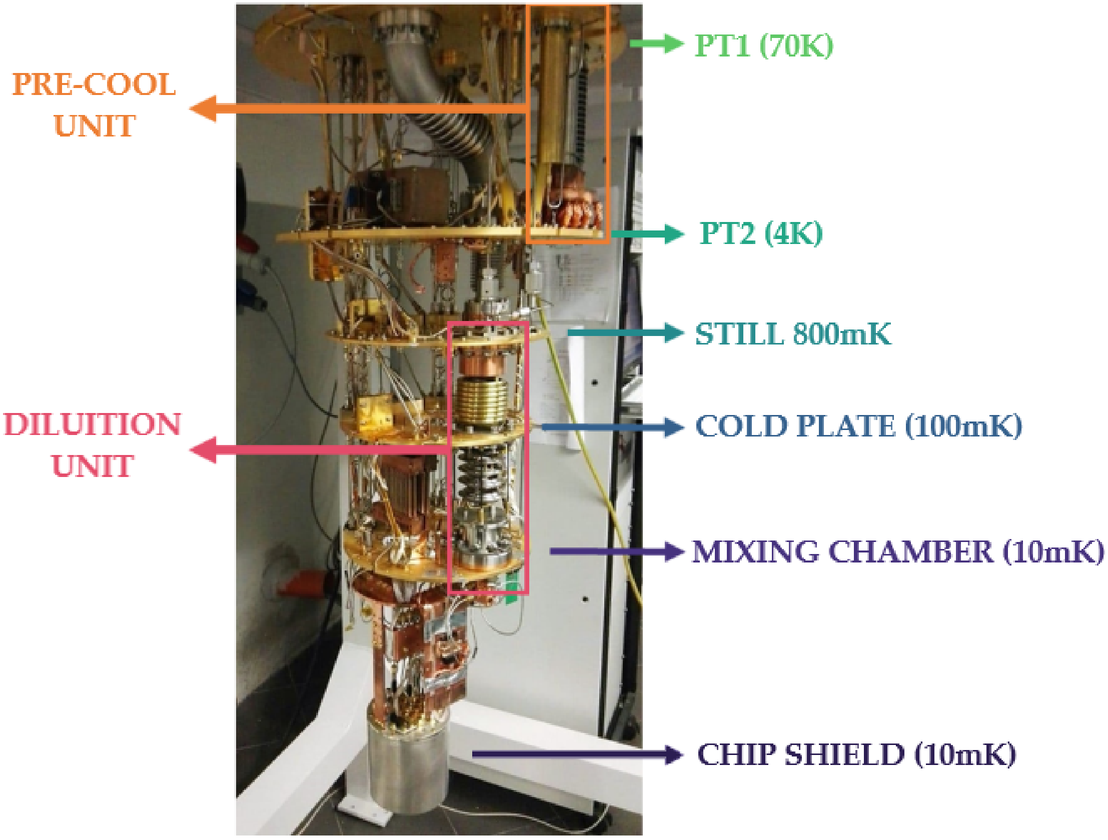

Figure 3.2: Core structure of the Triton. The labels indicate the different plates with the minimum temperature they can reach, the orange and red rectangles indicate the pre-cool unit and the dilution unit, respectively, which are the fundamental units of the Triton cooling procedure. At the bottom, anchored to the mixing chamber there is a copper extension to which the sample is anchored, and a tin shield, which screens the sample from external magnetic fields.

between the first two plates, i.e., *PT1* and *PT2*, that work at $70K$ and $4K$, respectively. The dilution unit shares the *still plate*, *cold plate* and *mixing chamber*. The first plate reaches a temperature of $800mK$. From the mixing chamber to the still plate, the mixture passes through a sequence of heat exchangers. The diluted phase in the mixing chamber, heavier than the concentrated phase, remains at the bottom of the mixing chamber and the gas of ^3He is pumped from the still chamber, thanks to a pumping system. This process is repeated till the mixture reaches $10mK$. In order to maintain the base temperature, the overall process made of condensation, dilution and evaporation is repeated in a closed cycle.

The stage containing the sample is thermally anchored to the mixing chamber through a copper extension, as shown in figure 3.2. The whole stage is then enclosed in a magnetic tin screen and a copper-coated cryoperm box (not shown) that screen from the environmental magnetic fields and are thermally anchored to the mixing chamber. The upper plates are also screened from the environment through a copper shield, for infrared radiation screening, anchored at the still plate, and two aluminum screens, anchored respectively at the $4K$-plate and the $70K$-plate.
In order to characterize superconducting qubits, coaxial cables are used, which allow operation within the microwave frequency range. The cryostat features four types of lines: input and output lines for the readout, drive lines for qubit control and flux lines for frequency tuning with an external magnetic flux. Specifically, in our case, there are 12 input lines and 2 output lines. The input lines are made of stainless steel, while the output lines are made of $CuNi$ from room temperature to $4K$ and $NbTi$ from $4K$ to $10mK$. The input lines are equipped with cryogenic attenuators, as shown in figure 3.3.

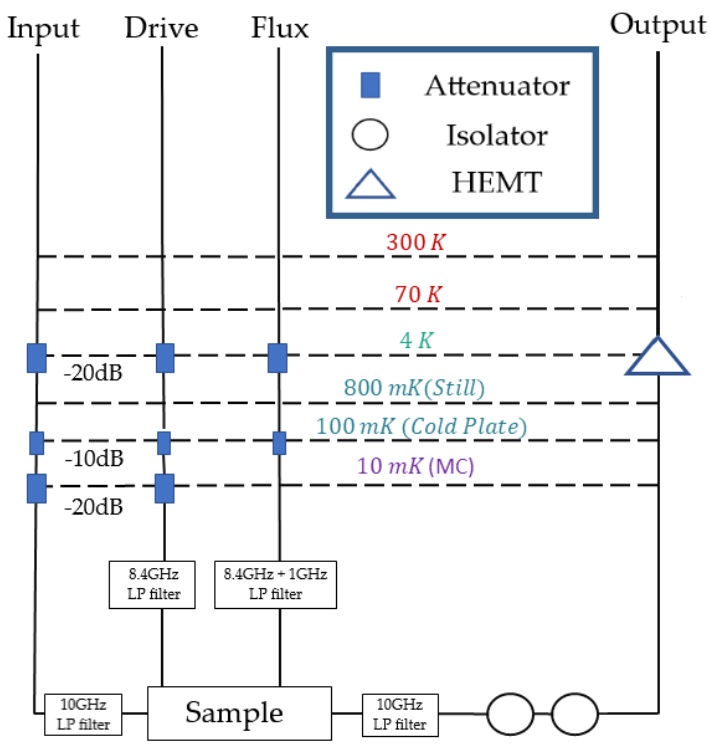

Figure 3.3: Cryogenic setup scheme, including the attenuation scheme for the input, drive and flux lines. On the output line, there are two isolators and an HEMT amplifier. Each line has a low-pass filter.

Specifically, on the feedline and drive lines, there is an overall attenuation of $-50dB$ and a low-pass filter with cutoff of about $10GHz$ and $8.4GHz$, respectively. On the flux lines, there are $-30dB$ of attenuation and two low-pass filters of $8.4GHz$ and $1GHz$. Finally, on the output lines, there is a $10GHz$ low-pass filter and two isolators, which are electronic devices that enable signal transmission in a preferred direction. Signals from the output towards the sample and reflections at the input port are attenuated nominally by a total of $40dB$. Since the output signals of the qubits are single-photon signals, amplifiers are required. However, amplifiers are noisy devices. Based on the device's properties, such as the noise temperature, it is fundamental to place them on a specific temperature plate. In our system, there are two amplification stages. There is an High Electron Mobility Transistor (HEMT) with nominal amplification of $40dB$ on the $4K$ plate, which cannot be placed on a cooler plate due to its noise temperature of $1.5K$, and three amplifiers at room temperature with nominal $16dB$ amplification each.

3.2 Room temperature electronics

The electronic set-up employed to measure and analyze the superconducting quantum processor is composed of a large variety of instruments at room temperature that play different roles, which will be described in this Section.

3.2.1 Vector Network Analyzer

To perform spectroscopy measurements we use the VNA, an instrument with two terminals (input and output) used for studying continuous signals. Mathematically, a two-port network is described by a 2×2 matrix of complex numbers that establish relations between the voltage and current across the ports, as shown in figure 3.4.

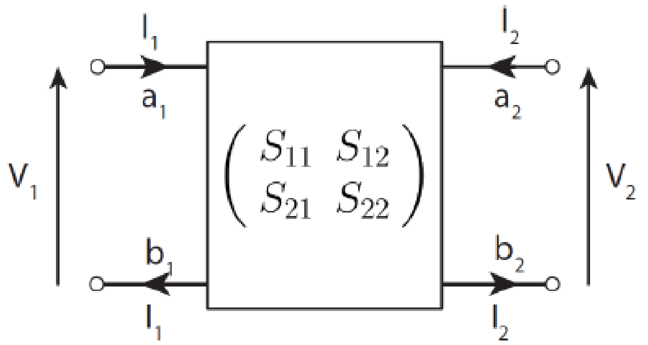

Figure 3.4: Schematic of a two-port network characterized by its scattering matrix.

The elements in the scattering matrix are called scattering parameters, each of which is a complex number. The S_{11} and S_{22} parameters represent the reflection coefficients from port 1 and port 2, while S_{21} and S_{12} are the transmission coefficients from port 1 to port 2 and vice versa. The real and imaginary parts of the transmission parameter S_{21} are the key quantities for qubit characterization, since they allow to extract the readout resonator characteristics and qubit transition frequencies.
The VNA that has been employed in this thesis is the Rohde&Schwarz Vector Network Analyzer ZVL6 (R&S ZVL) [77], which is a two port VNA. It presents a physical interface that allows setting different features related to the measurements and a display that shows the acquired data, but it is also possible to remotely control it through an ethernet LAN connection.

3.2.2 Time domain measurements

If we want to go beyond spectroscopy measurement, it is necessary to perform time-domain measurement. In time-domain experiments readout and drive tone signals are replaced by microwave pulses sequences. The microwave pulses are generated with I-Q mixers, Arbitrary Waveform Generators (AWGs) and RF signal generators. The AWG used in the experimental setup is able to generate microwave signals with frequencies up to 400MHz [78]. Since qubits and readout resonators operate typically in the $4-8GHz$ range, we need faster signals, so we combine the AWG signal (ω_{IF}) with an RF signal, called *Local Oscillator* (LO) through an I-Q Mixer. This process is called up-conversion and is shown in figure 3.5a).

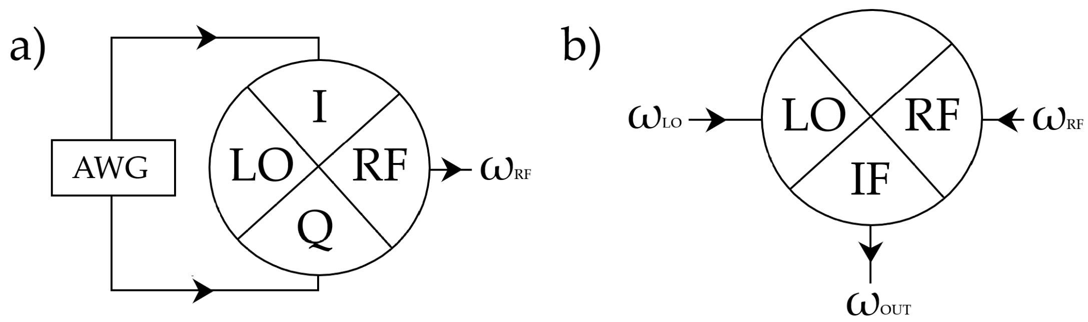

Figure 3.5: In a) up conversion scheme. The I-Q mixer combines the I and Q components of the Arbitrary Waveform Generator (AWG) signal with the Local Oscillator (LO) and gives ω_{RF} as output; b) down conversion scheme. The I-Q mixer combines the qubit output signal with the LO and gives ω_{IF} as output.

The I-Q Mixer output frequency is the input signal for the qubit and is given by:

$$\omega_{RF} = \omega_{LO} \pm \omega_{IF}. \tag{3.1}$$

We can select one of these outputs thanks to single-sideband calibration [15].
Since the output signal is of the order of several GHz, it would be very difficult for the electronics to read it properly. For this reason demodulation and down-conversion are necessary. The output signal goes in a mixer, which has only 3 ports compared to the I-Q mixer which has 4 ports, as shown in figure 3.5b). It combines with the LO signal and the resulting signal has the following frequency:

$$\omega_{IF} = \omega_{RF} \mp \omega_{LO}. \tag{3.2}$$

Then a digitizer converts the signal in the required frequency range of the order of 0-500 MHz [79]. Finally, a Fast Fourier Transform is performed by the integrated software of the digitizer in order to extract the original form of the readout signal (RO) coming from the resonators coupled to the qubits. The results are displayed and stored through the Labber software [80]. The whole process is shown in figure 3.6.

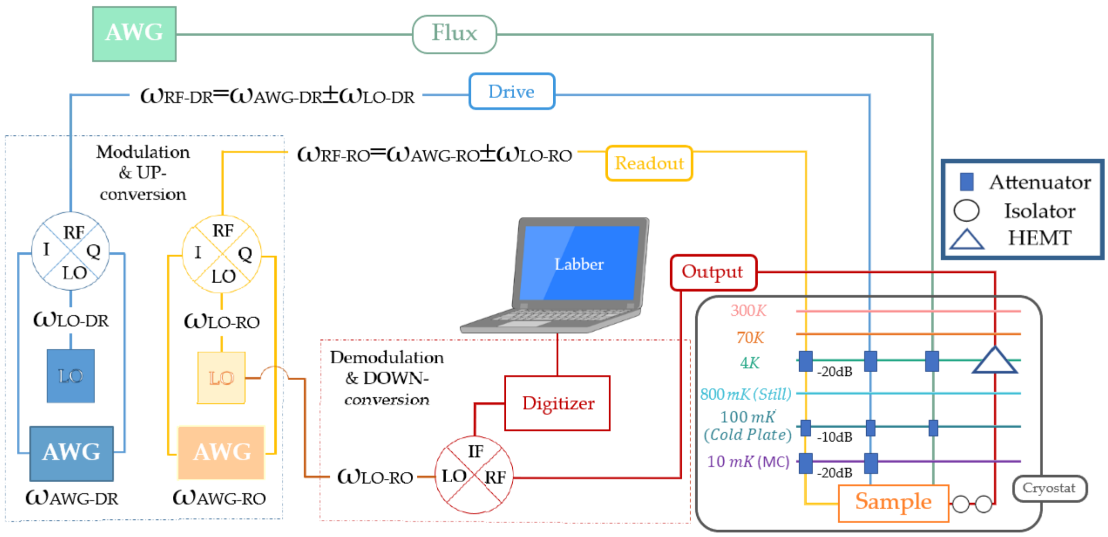

Figure 3.6: Simplified schematic of the experimental setup used for dispersive qubit readout and control. In blue it is shown the up-conversion of the drive signal, in yellow the up-conversion of the readout signal, in green the flux line and in red the down-conversion of the output signal, which is measured with the digitizer and then is stored, manipulated and visualized with Labber. Each line is connected to the cryogenic setup, whose details are shown in figure 3.3. Figure adapted from [43]

All these instruments are grouped in a PXI chassis, i.e., a multi-slot system produced by Keysight Technologies [81], shown in figure 3.7.

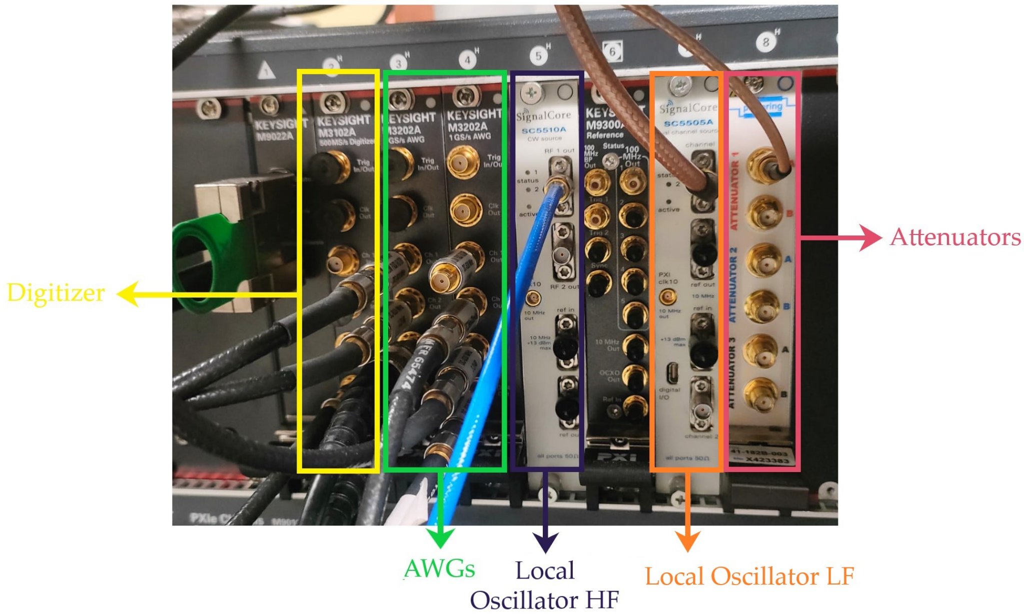

Figure 3.7: PXI chassis used to generate pulsed signals. In yellow it is highlighted the digitizer, in green the Arbitrary Waveform Generators (AWGs), in blue the local oscillators at high frequency (HF), in orange the local oscillators at low frequency (LF) and in pink the attenuators.

The slots are occupied by:

- Two Arbitrary Waveform Generators (AWGs), that generates I and Q component of the readout and control signals at frequencies (ω_{IF}), respectively;
- Digitizer, that acquires data with a sampling rate of $500MSa/s$;
- 3-channels attenuator, with an attenuation range from $0dB$ to $30dB$;
- Local Oscillators (LO), that generate a continuous signal up to $6GHz$ (LF) for the drive of the low and medium frequency qubits and up to $20GHz$ (HF) for the readout (ω_{LO}).

An additional RF generator from R&S (SMA 100B) with maximum 12.75 GHz has been used as LO for the drive of high frequency qubits [82].

In order to implement algorithms, a major control of the sequence of pulses is needed. For this reason, we have used a different instrument fully interfaceable with Python, thanks to the open source package Quantify [83]. This instrument is the Qblox cluster, shown in figure 3.8 [84].

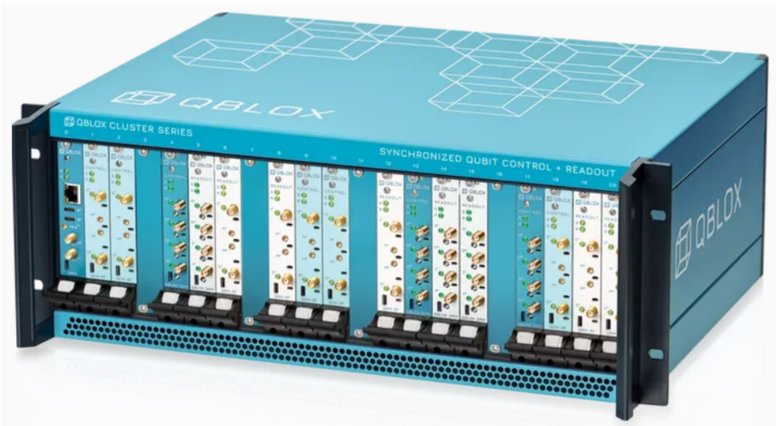

Figure 3.8: Qblox cluster [84].

The main advantage is that the modules of the Qblox rack have an up and down conversion system integrated directly into the cards. This allows for better signals calibration. The modules used for the measurements of this thesis are:

- Qubit Readout Module RF (QRM-RF), which allows output and input signals up to $18.5GHz$;
- Qubit Control Module RF (QCM-RF), which allows output signals up to $18.5GHz$;
- Qubit Control Module (QCM) for flux pulses, which generates output signals up to $400MHz$.

3.3 5-qubit quantum device

The superconducting quantum device analyzed in this thesis is a five transmon qubit chip, realized by QuantWare, spin-off company of the University of Delft [85].

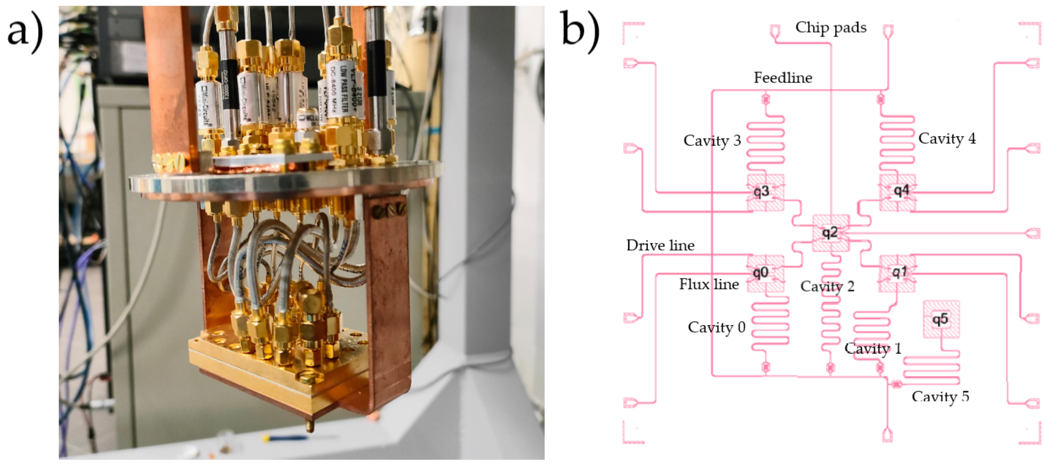

Figure 3.9: In a) chip package and microwave lines connected to the cryogenic electronic setup; b) Layout of the QuantWare chip. The chip consists of five coupled qubits with their readout resonators (from cavity 0 to cavity 5), a drive line and a flux line. Each readout resonator is coupled to the common feedline. The qubit-qubit coupling through qubit 2 is realized through high frequency coupling resonator. In the bottom right corner of the chip design, there is a single qubit for diagnostic.

The chip is composed of six qubits: one isolated qubit for test, and 5 coupled qubits. More specifically, all the qubits are connected and coupled between them through the qubit 2 in the middle. Qubit 0 and qubit 1 have the lowest resonance frequency on the chip, qubit 3 and qubit 4 have the highest resonance frequency and qubit 2 has an intermediate resonance frequency. This design is suitable for advanced quantum error detection and correction [86][87][88]. All the qubits are flux-tunable, i.e., they include a DC-squid, where the Josephson junctions are composed of aluminum electrodes and AlO_x barrier. Each of the qubits has its own flux line for qubit frequency tunability, drive line for control and a readout resonant cavity. All of them are in $NbTiN$. The latter and the readout resonators are all coupled to a common feed line. This configuration allows for multiplexing, i.e., to address multiple resonators with the single feedline by sending readout tones with different frequencies. In figure 3.9a) it is shown the sample holder of the chip and all the connections to the cryogenic electronic setup. In figure 3.9b) it is shown the design of the chip inside the sample holder.

The qubits and resonators design parameters are reported in table 3.1.

Qubit	Qubit frequency at flux SS (GHz)	Resonator frequency (GHz)	E_C (GHz)	E_J (GHz)	E_J/E_C
0	4.7	7.2	0.27	11.4	42.2
1	4.7	7.4	0.27	11.4	42.2
2	5.6	7.6	0.27	16.0	59.3
3	6.5	7.8	0.27	21.2	78.5
4	6.5	8.0	0.27	21.2	78.5
5	4.7	7.0	0.27	11.4	42.2

Table 3.1: For each qubit, it is reported the resonance frequency at the flux sweet spot (SS), the frequency of the coupled resonator, E_C, E_J and their ratio.

The cavity coupled to each transmon qubit is a coplanar waveguide (CPW) quarter wavelenght ($\lambda/4$) transmission line. It consists of a center strip of width W, separated by a gap of width G from the ground planes on each side, as shown in figure 3.10.

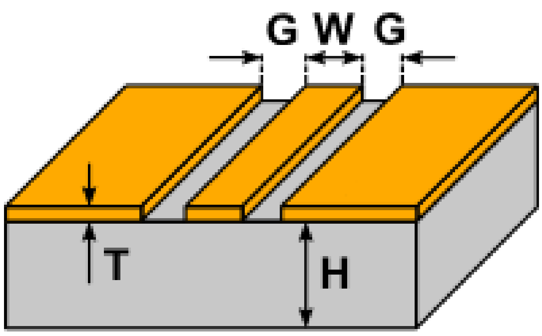

Figure 3.10: A cross section cut of a coplanar waveguide cavity. It has a center conductor strip with a width W and gaps of width G, while the thickness of the metal and of the dielectric are denoted T and H, respectively [89].

The cavity resonator is characterized by the resonance frequency f_0 and the quality factor Q, defined respectively as:

$$f_0 = \frac{c}{4l\sqrt{\varepsilon_{eff}}} \tag{3.3}$$

$$Q = \frac{\text{Stored energy}}{\text{Dissipated energy/radian}}, \tag{3.4}$$

where c is the speed of light in vacuum, l is the length of the $\lambda/4$ resonator and ε_{eff} is the effective dielectric constant.
It is possible to distinguish between the intrinsic quality factor Q_I, that accounts for the energy dissipated into the substrate and the resonators materials, and the coupling quality factor Q_C, that accounts for the energy lost to the external circuit connected to the resonator [89]. Thus, the total Q_l-value can now be expressed in terms of these two contributions:

$$\frac{1}{Q_l} = \frac{1}{Q_I} + \frac{1}{Q_C}. \tag{3.5}$$

Chapter 4

Experimental results and discussion

In this Chapter, we report the experimental results on single qubits and two coupled qubits, which are part of a 5-qubit processor. The data have been acquired by using the techniques described in Chapter 2 on the pair composed of qubit 0 and qubit 2. The aim of the analysis is to assess the ability of the processor to give high fidelity output of different single- and two-qubit quantum circuits. Therefore, the ultimate outcome of the analysis will be the estimation of the so-called Hellinger fidelity. Its measurement allows us to estimate how similar two classical expectation values probability distributions are: the output of the real NISQ (Noise Intermediate Scale Quantum) processor and the ideal expected output of the implemented quantum circuits. The estimation of the Hellinger fidelity requires a systematic single- and two-qubit characterization of the device. Single-qubit characterization is carried out to estimate the resonant frequencies of readout resonators and qubits, as well as the coherence times described in Section 1.6. Moreover, Hellinger fidelity calculation relies on fundamental optimization protocols such as Rabi oscillation, Ramsey interferometry, AllXY and Motzoi calibration, which have been employed for the calibration of single-qubit pulses. The pulse calibration has also been performed on the two-qubit CZ gate, within the conditional oscillation experiment. Finally, quantum circuits were implemented after calibrating the pulses, involving both single-qubit and two-qubit gates. Once optimal conditions for single- and two-qubit gates have been realized, we have compared the ideal output of these circuits and the measured output, and we have quantified the quality of the quantum circuits output using the Hellinger fidelity. We will demonstrate that high-fidelity quantum circuits strongly rely on the quality of the single- and two-qubit gates in the sequences.

4.1 Resonators characterization

As a first step for the single qubit characterization, the readout resonators coupled to the qubits must be fully characterized. A single-tone signal in the range of the resonator frequencies is sent through the feedline. When the resonator absorbs photons, it is possible to measure a dip in the S_{21} signal, corresponding to the resonance frequency of the readout resonator (Section 1.4). Once the frequencies of the resonators have been identified, sweep in power of the feedline input signal is performed in order to reach the single-photon regime. These measurements were performed using the VNA for resonator 0, coupled to qubit 0, and resonator 2, coupled to qubit 2 (figure 3.9b)). In both cases, there was an additional attenuation of $-30dB$ at the input and $3 \times 16dB$ at the output given by three amplifiers at room temperature (Section 3.1). The outcomes are shown in figure 4.1.

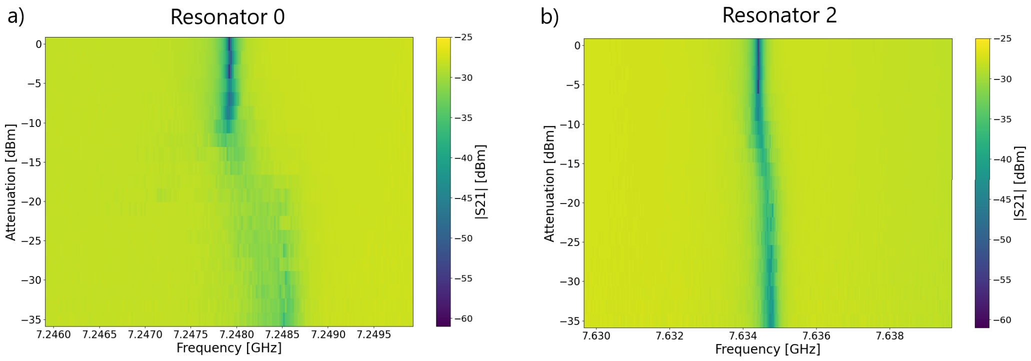

Figure 4.1: Dispersive shift colormap for a) resonator 0 and b) resonator 2. On the y-axis, Vector Network Analyzer (VNA) input power in dBm, on the x-axis readout tone frequency. The color scale identifies the magnitude of the S_{21} parameter.

In figure 4.2a),we identify the bare state (-3.5 dBm) and the single-photon state (-35dBm) for resonator 0 at zero external magnetic field. The low-photons shift for res-

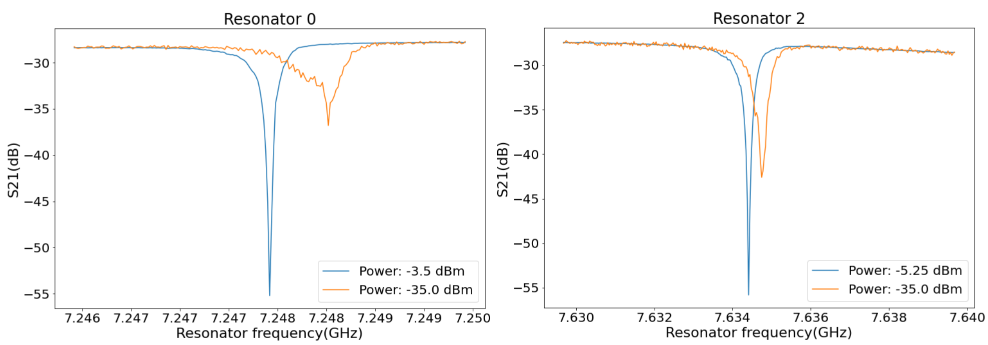

Figure 4.2: Dispersive shift for a) resonator 0 and b) resonator 2. The blue line represents the bare state, while the orange line the low-photon state.

onator 0 is $\chi = 649 \pm 19kHz$. For resonator 2, shown in figure 4.2b), it is $\chi = 342 \pm 95kHz$. This experiment allows to identify the readout resonator frequency in the low-photon regime, which is $7.249 \pm 0.001GHz$ for resonator 0, and $7.635 \pm 0.001GHz$ for resonator 2. The same measurements were repeated with the Qblox instrument in time domain, which allows to apply larger voltages across the qubit dedicated flux lines compared with the Keysight electronics. Indeed, the Keysight AWGs apply DC offset ranging from -1.5 to $1.5V$, while QuBlox allows to generate up to 2V, which guarantees to increase the flux modulation bandwidth of the qubits frequency.
In order to estimate the resonators parameters, we perform a fit of S_{21} using the Python package *resonator_tools* [90][26], as shown in figure 4.3.

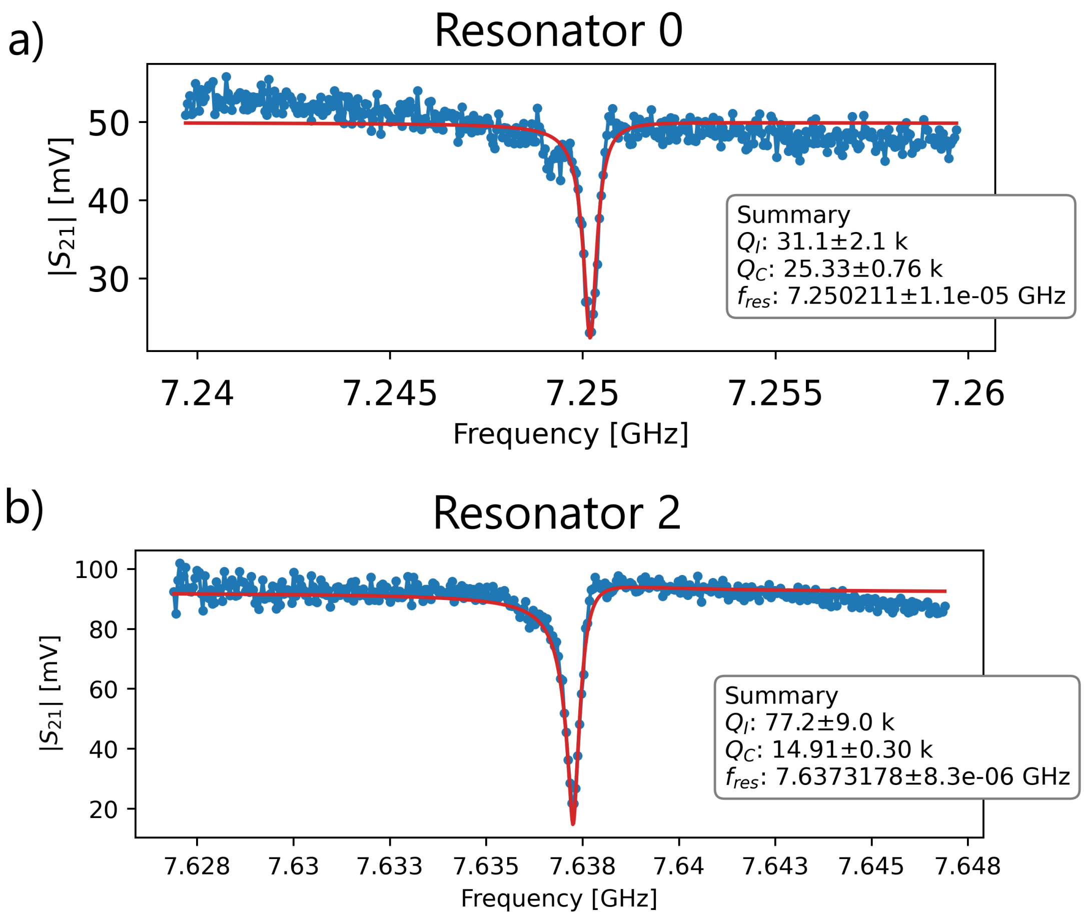

Figure 4.3: Spectroscopy measurement for a) resonator 0 and for b) resonator 2. The blue line represents the measured magnitude of the S_{21} parameter, while the red line represents the fit used to estimate the resonator parameters, such as internal quality factor Q_I, the external quality factor Q_C and the resonant frequency f_{res} in the legends.

The intrinsic quality factor Q_I, the coupling quality factor Q_C and the total quality quality factor Q_l are related by the relation in equation 3.5. In our case, the internal quality factor Q_I is larger than the coupling quality factor Q_C, so the resonator is not limited by internal losses. In the case of niobium compounds superconducting resonators, these numbers comply with the literature [91] and allow to perform the readout of the qubit state.

4.2 Qubit spectroscopy and avoided level crossings

For the single qubit characterization, it is necessary to set the parameters of the readout resonators, i.e. the frequency and the power, in order to be in the low-photon regime (Section 4.1). We first provide a measurement of the qubit frequency through two-tone spectroscopy. The two-tone signal is composed of an RF signal that is close to the frequency of the readout resonator resonance in the dispersive regime and is sent through the feedline to excite the resonator (readout tone), and an RF signal that sweeps in frequency, which excites the qubit (drive tone). The latter is sent through the dedicated qubit drive line. By applying an external flux field through the dedicated flux lines, spectroscopy is performed on qubit 0 and qubit 2. The results are shown in figure 4.4a) and 4.4b), respectively.

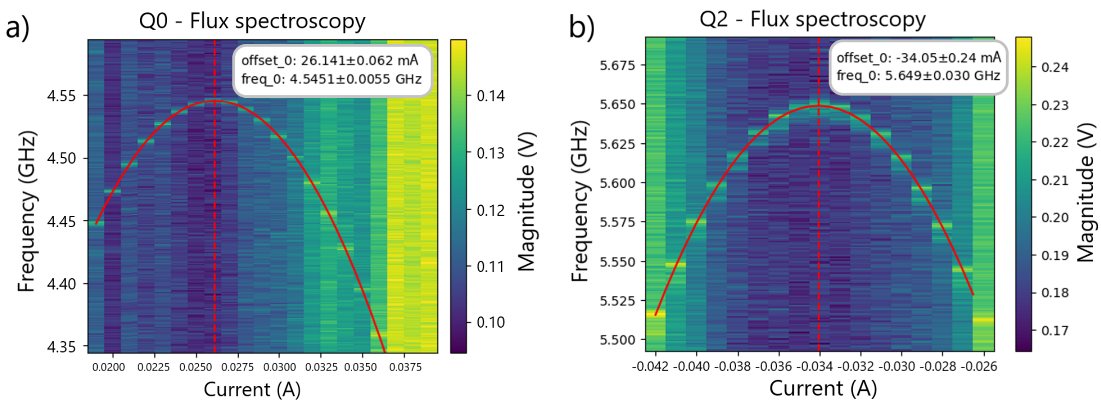

Figure 4.4: Flux modulation of the resonance frequency of a) qubit 0, coupled to resonator 0, and b) qubit 2, coupled to resonator 2. The x-axis is the current applied across the flux line, the y-axis is the qubit frequency, and the color scale identifies the output magnitude.

On the x-axis, we show the current passing through the dedicated flux bias lines of the two qubits. For each of these values, two-tone spectroscopy provides a measure of the magnitude of the readout voltage signal acquired at fixed readout resonator frequency as a function of the microwave drive tone, sent through the dedicated control line of the two qubits. When this tone enters on resonance with the qubit transition frequency, a peak in the readout voltage occurs (yellow in the colorbar scale). This peak follows a cosinusoidal modulation as a function of the flux, as predicted in Section 1.3. Therefore, by fitting the qubit frequencies as a function of the flux we identify the required flux value to bring the qubit to the sweet spot (SS).
In Figure 4.5, we report the magnitude of the demodulated readout output voltage as a function of the qubit drive frequency and the qubit drive power across the dedicated drive line for qubit 0 and qubit 2, in panels $a)$ and $b)$.

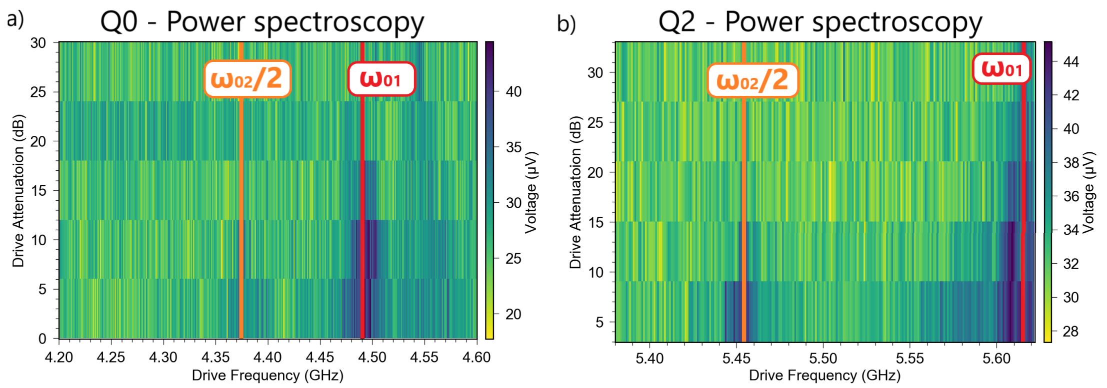

Figure 4.5: In a) qubit 0 spectroscopy; b) qubit 2 spectroscopy. On the x-axis, the qubit drive frequency, on the y-axis the attenuation of the qubit drive signal, which has to be combined with the attenuation along the line. The color scale identifies the demodulated voltage magnitude in μV of the readout resonator.

In both cases, the two coupled qubits were set in frequency far from each other: specifically, qubit 0 spectroscopy has been performed by setting qubit 2 in its flux modulation minimum, and qubit 0 at 88% of the SS. The frequency of the fundamental transition $|0\rangle \rightarrow |1\rangle$ for qubit 0 at this flux point is $\omega_{01} = 4.498 \pm 0.001 GHz$, while for qubit 2 we expect from the design specifications a frequency of the order of $5.7 GHz$, i.e. above ω_{01} for qubit 0. Therefore, we performed the spectroscopy measurement for qubit 2, setting qubit 0 and qubit 2 at 88% and 89% of their maximum flux modulation, respectively. This guaranteed that the qubits were detuned of at least $1 GHz$, thus complying with the single-qubit regime. For qubit 2, $\omega_{01} = 5.620 \pm 0.001 GHz$. Here the errors are maximum errors given by the resolution bandwidth of the drive tone.

In figure 4.5, there is more than one peak. This indicates that, for sufficiently high power levels, we can also observe higher order energy levels. Specifically, due to the negative anharmonicity of the transmon, the highest frequency peak corresponds to ω_{01}. By increasing the power, the first peak occurring at lower drive frequencies is the 2-photon assisted $|0\rangle \to |2\rangle$ transition at $\omega_{02}/2$ energy level, and the $|1\rangle \to |2\rangle$ transition ω_{12} energy [9]. If we take into account the expression of the anharmonicity discussed in Section 1.2, we can compute it by using the measured ω_{01} and ω_{02} as $\alpha = 2(\omega_{01} - \omega_{02}/2)$. Given for qubit 0 $\omega_{02} = 4.375 \pm 0.001 GHz$, the anharmonicity is $\alpha = 246 \pm 2MHz$. For qubit 2, $\omega_{02} = 5.455 \pm 0.001 GHz$, hence the anharmonicity is $\alpha = 330 \pm 2MHz$. These values are in agreement with what is typically expected in the transmon regime [9].
Finally, since one of the final goals of this thesis is to implement two-qubit gate circuits, it is necessary to establish the flux range for which the qubits coherently couple one to each other, as described in Section 1.7. More specifically, the implementation of the CZ gate requires identifying the avoided level crossing between the 2-qubit states $|11\rangle$ and $|02\rangle$. For this reason, a spectroscopy measurement is performed on qubit 0, while tuning the flux on qubit 2, in a range of drive frequencies able to excite both the ω_{01} and the $\omega_{02}/2$ of qubit 0, and it is shown in Figure 4.6.
In this experiment, the qubit 0 is set to its SS. The avoided level crossing between the $|01\rangle$ and $|10\rangle$ levels is highlighted in orange, while the avoided level crossing between the $|11\rangle$ and $|02\rangle$ levels in yellow. Because of the high power applied to observe the $|11\rangle - |02\rangle$ transition, the $|01\rangle - |10\rangle$ transition becomes significantly broadened. It is possible to verify that in this measurement the $|01\rangle$ transition has a full width at half maximum consistent with the one estimated from the spectroscopy measurements in Figure 4.5, which is about $16.62MHz$. Moreover, a rough estimation of the coupling strength of the $|11\rangle - |02\rangle$ transition yields a value of $g_{|11\rangle - |02\rangle}$ in the range of tens of MHz. Consequently, the ratio of g/α is approximately 0.05. This value is reasonable, given that to achieve a high fidelity CZ gate, the parameter regime for direct qubit-qubit coupling requires $g/\alpha < 0.24$ [92].

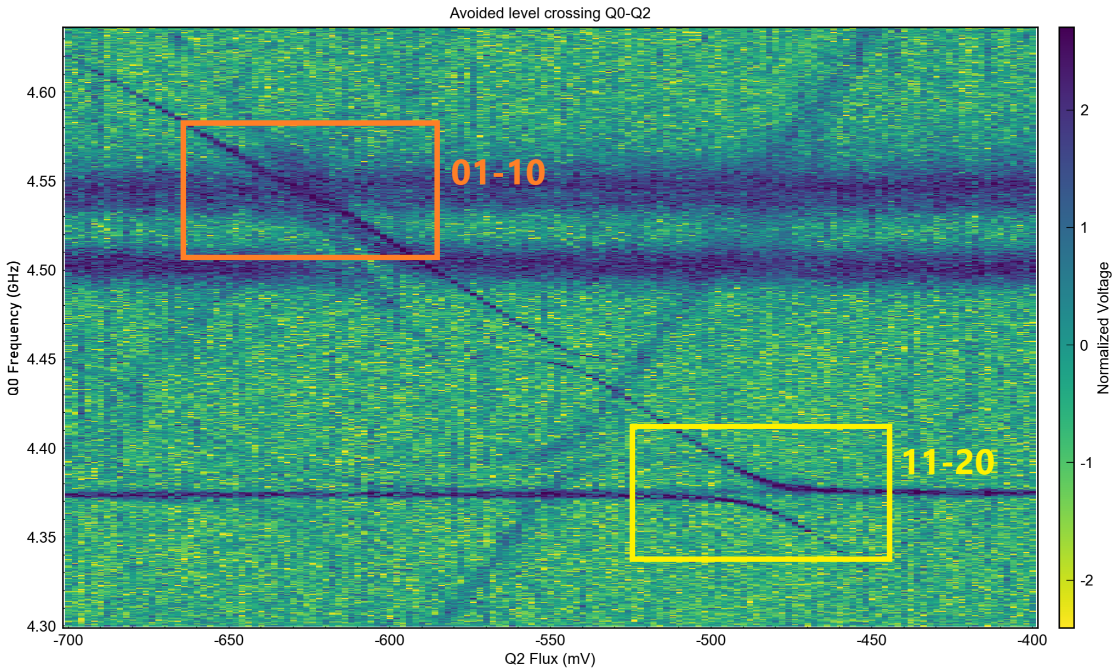

Figure 4.6: Avoided level crossing for qubits 0 and 2: on the x-axis the applied flux on qubit 2, on the y-axis the qubit frequency of qubit 0 and the color scale is the normalized voltage measured on the readout resonator 0. The orange box highlights the avoided level crossing between the $|01\rangle$ and $|10\rangle$ levels, while the yellow one highlights the avoided level crossing between the $|11\rangle$ and $|20\rangle$ levels.

4.3 Decoherence times

In order to fully characterize the qubits, it is necessary to estimate the relaxation time T_1 and the coherence time T_2, by using the protocols reported in Section 2.4.1 and 2.4.2, respectively. For the latter, we employed both the Hahn-Echo [15] and the Ramsey Interferometry protocols [15] (Section 2.4.2 and 2.2.2, respectively).
In order to apply the pulses involved in these protocols, it is mandatory to define the π-pulse. Using the Rabi oscillation protocol described in Section 2.2.1, we estimated the π-pulse duration. The measured outputs of this Rabi protocol for qubit 0 and qubit 2 are shown in figure 4.7. The function used for the fit of Rabi oscillation is $a \sin(bx + c) + d$. The π-pulse plateaus are π-pulse$_{Q0} = (55 \pm 1)$ ns for qubit 0 and π-pulse$_{Q2} = (17 \pm 1)$ ns for qubit 2. The faster π-pulse measured for qubit 2 than for qubit 0 is consistent with the larger drive power strenght sent through the qubit 2 dedicated drive line: the attenuation on qubit 0 is $18dB$, while on qubit 2 is $15dB$.

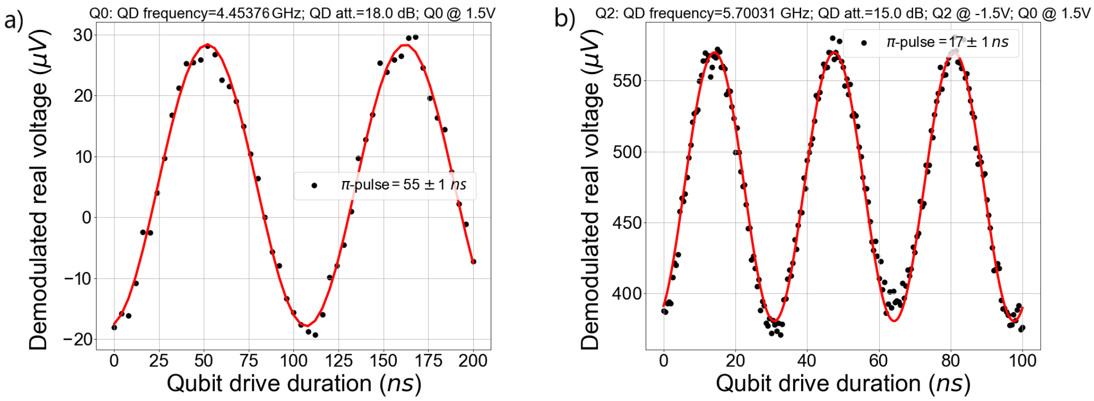

Figure 4.7: The Rabi oscillation for a) qubit 0 and b) qubit 2 by changing the plateau duration. The red line represents the fit used to estimate the π-pulse plateau. For the measurement in figure a), the drive frequency is $4.454GHz$, along with an $18dB$ attenuation on the drive line and $1.5V$ applied by the dedicated flux line for qubit 0. In figure b), the measurement employs a drive frequency of $5.700GHz$, an attenuation of $15dB$ on the drive line, and $1.5V$ and $-1.5V$ applied by the dedicated flux lines for qubit 0 and qubit 2, respectively.

For the π-pulses, we have optimized the amplitude of pulse, while keeping 20 ns as the π-pulse duration both the qubits. An example of the π-pulse amplitude estimation through Rabi oscillation fitting is reported in figure 4.8.

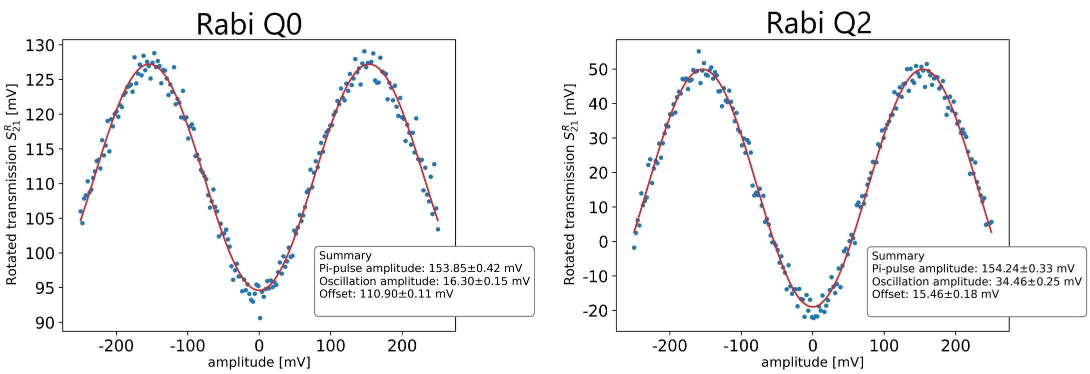

Figure 4.8: The Rabi oscillations for a) qubit 0 and b) qubit 2 by changing the π-pulse amplitude. The red line represents the fit used to estimate the π-pulse amplitude.

Once the π-pulse is obtained, it is possible to estimate the decoherence times of the two qubits. We show in figure 4.9 a comparison between the demodulated voltage output as a function of the sequence duration in the T_1 (blue) and T_2^{Echo} (black) protocols for both the qubits.

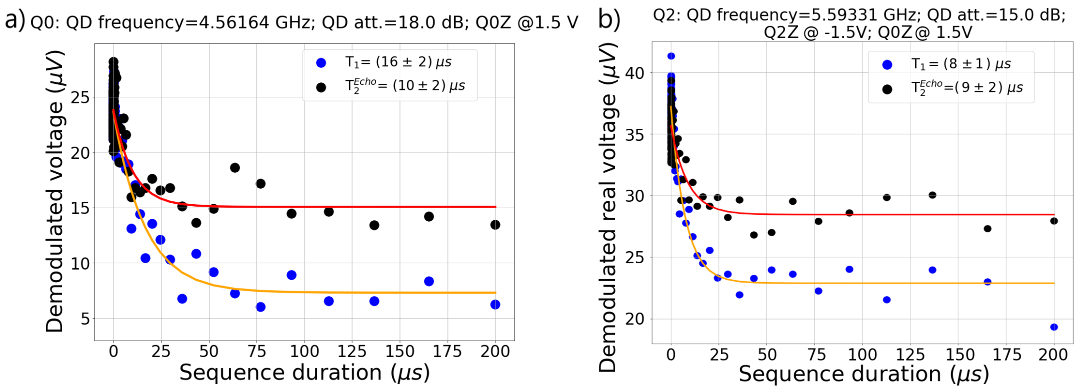

Figure 4.9: T_1 and T_2^{Echo} measurements for a) qubit 0 and b) qubit 2: the x-axis represents the sequence duration, while the y-axis represents the demodulated voltage output. The black dots and solid red line correspond to the measured values and the fit for T_2^{Echo}, respectively. Similarly, the blue dots and solid orange line correspond to the measured values and the fit for T_1. For the measurement in figure a), a drive frequency of $4.56164 GHz$ is used, along with an $18 dB$ attenuation on the drive line and $1.5V$ applied by the dedicated flux line for qubit 0. In figure b), the measurement employs a drive frequency of $5.59331 GHz$, an attenuation of $15 dB$ on the drive line, and $1.5V$ and $-1.5V$ applied by the dedicated flux lines for qubit 0 and qubit 2, respectively. The legends shows the results of T_1 and T_2^{Echo} estimated from the fitting procedure.

Using the Python package *lmfit*, we fit the measured results and estimate T_1 and T_2^{Echo} for both qubits. The function used for fits is $ae^{-x/b} + c$, where b is the relaxation time T_1 or the decoherence time T_2^{Echo}, according to the implemented protocol. One-shot relaxation and Hahn-Echo times are $T_1 = (16 \pm 2)\mu s$ and $T_2^{Echo} = (10 \pm 2)\mu s$ for qubit 0, while $T_1 = (8 \pm 2)\mu s$ and $T_2^{Echo} = (9 \pm 2)\mu s$ for qubit 2. A more physical estimation of these values must be derived from a statistical measurement of the relaxation and decoherence times. Hence, we performed repeated measurements of T_1 and T_2^{Echo}, for a time period of 12 hours, in order to obtain their statistical values. In figure 4.10a), the results of the T_1 measurements on qubit 0 as a function of time are shown, while in figure 4.10b), the counts of T_1 have been collected in a count distribution with binning of 20.

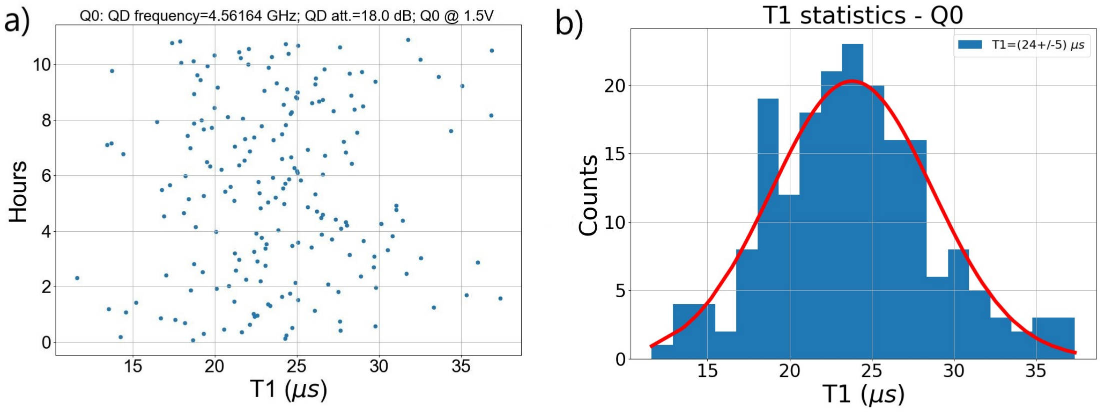

Figure 4.10: In a) T_1 measurements repeated in 12 hours for qubit 0; in b) counts of T_1 values obtained from the a) measurement. The distribution used for fitting is a Gaussian distribution, which is represented by the red line.

The same analysis has been done for qubit 2, and it is reported in figure 4.11.

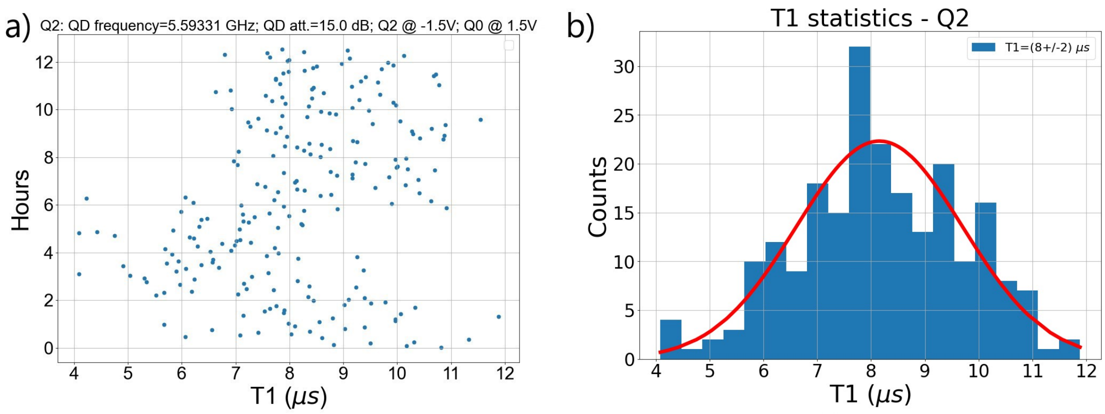

Figure 4.11: In a) T_1 measurements repeated in 12 hours for qubit 2; in b) counts of T_1 values obtained from the a) measurement. The distribution used for fitting is a Gaussian distribution, which is represented by the red line.

According to Section 1.6, the relaxation time T_1 and the coherence time T_2 are affected by stochastic noise as a result of relaxation and pure dephasing phenomena. Therefore, in order to estimate T_1 and T_2, the normal distribution was employed [15], whose mean value is defined as $\mu = \frac{1}{N}\sum_{i=1}^{N} x_i$, where x_i are the individual values sampled from the distribution and N is the number of samples, and the error is given by the standard deviation, defined as $\sigma = \sqrt{\frac{1}{N}\sum_{i=1}^{N}(x_i - \mu)^2}$. The statistical values of T_1 are $T_1 = (16 \pm 2)\mu s$ for qubit 0 and $T_1 = (8 \pm 1)\mu s$ for qubit 2. The same procedure has been repeated for T_2^{Echo} and the results are shown in figure 4.12.

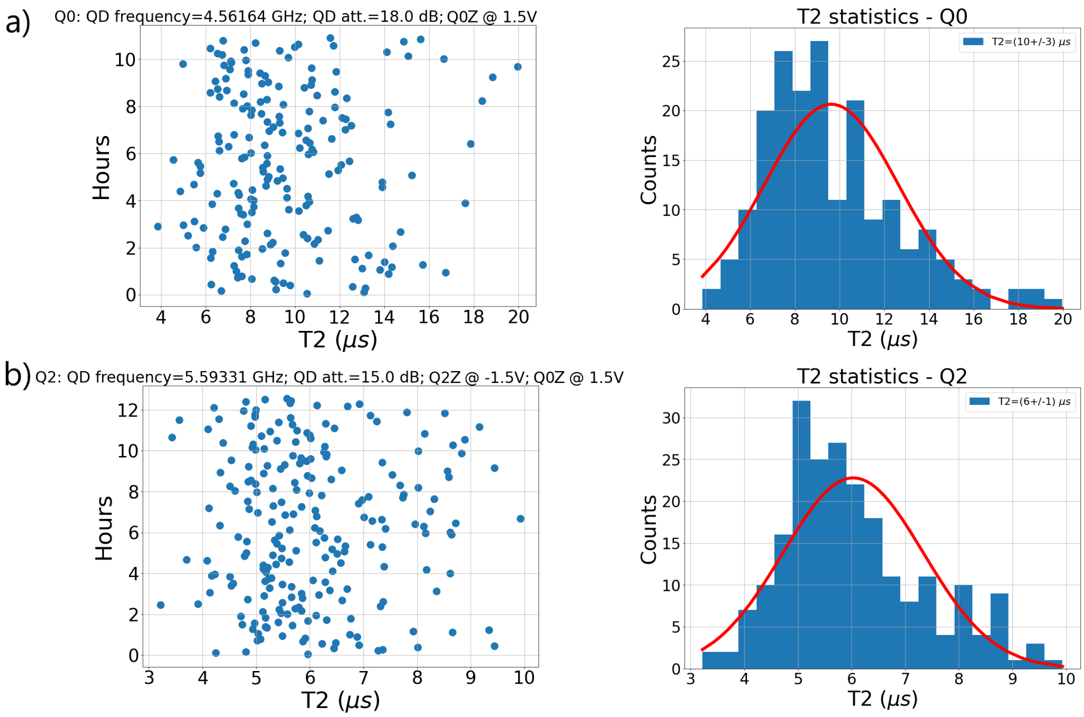

Figure 4.12: In a) T_2 measurements repeated in 12 hours for qubit 0; in b) counts of T_2 values obtained from the data in a); c) T_2 measurements repeated in 12 hours for qubit 2; d) counts of T_2 values obtained from the data in c). The distribution used for fitting is a Gaussian distribution, which is represented by the red line.

The statistical values of T_2 obtained are $T_2 = (10 \pm 2)\mu s$ for qubit 0 and $T_2 = (9 \pm 2)\mu s$ for qubit 2. From the comparison between T_1 and T_2 for both qubits, it is evident that is not verified the condition $T_2 \simeq 2T_1$ (Section 1.6.3). This indicates that the longitudinal decay is determined by the dephasing time. Moreover, when comparing T_1 and T_2^{Echo} between the two qubits, it is possible to notice that the relaxation and coherence times of qubit 0 are higher than those of qubit 2. This is due to the fact that qubit 2 is connected to all the other four qubits, which open dissipation channels, while qubit 0 is only connected to qubit 2.
Additionally, using the Ramsey Interferometry protocol (Section 2.2.2), we estimated T_2^*. The experimental results of this protocol is shown in figure 4.13.

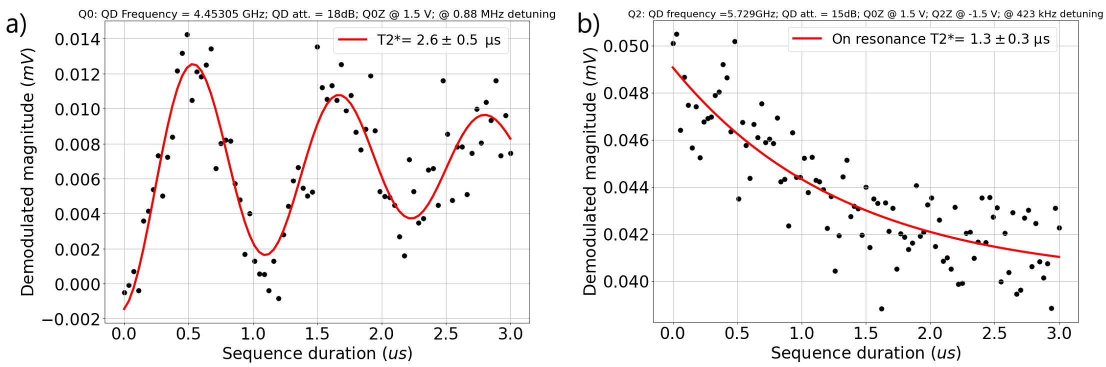

Figure 4.13: Ramsey oscillation for a) qubit 0 at 0.88 MHz of detuning and b) qubit 2 a 423 kHz of detuning. The red line is the fit of the measured data, used to estimate T_2^*.

More in detail, in figure 4.13a) it is shown the off-resonance Ramsey oscillations for qubit 0 at $0.88MHz$ of detuning. According to Section 2.2.2, the oscillations are those of a damped oscillator that decay over time with a characteristic time T_2^*. In Figure 4.13b), the on-resonance Ramsey oscillation for qubit 2 is shown. Since the drive pulse frequency is close to the qubit resonance frequency, an exponential decay is observed. The function used for the fit is $(a\sin(bx+d)^2+c)e^{(-x/e)}+f$. The T_2^* values estimated from the two measurements are $T_{2-Q0}^* = (2.6 \pm 0.5)\mu s$ for qubit 0 and $T_{2-Q2}^* = (1.3 \pm 0.3)\mu s$ for qubit 2.
Finally, repeating the same procedure used for T_1 and T_2^{Echo}, the statistical value of T_2^* for both qubit has been calculated, as shown in figure 4.14.

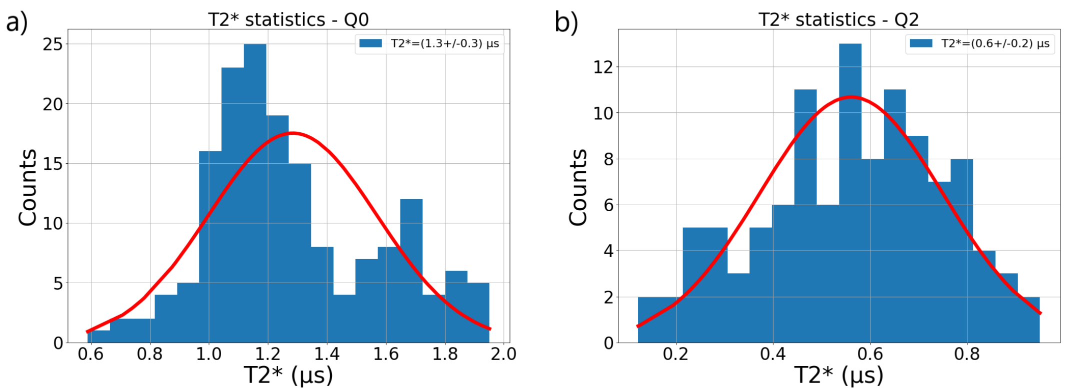

Figure 4.14: Counts of T_2^* values obtained for a time period of 6 hours, in a) for qubit 0 and b) qubit 2. The distribution used for fitting is a Gaussian distribution, which is represented by the red line

Also in this case, the Ramsey decoherence time for qubit 0 appears to be larger than for qubit 2. This is also explained by the larger connectivity of qubit 2 compared to qubit 0. A summary of the decoherence times analysis is reported in table 4.1.

	$T_1(\mu s)$	$T_2^{Echo}(\mu s)$	$T_2^*(\mu s)$	Stastistic $T_1(\mu s)$	Stastistic $T_2^{Echo}(\mu s)$	Statistic $T_2^*(\mu s)$
Qubit 0	16 ± 2	10 ± 2	2.6 ± 0.5	29 ± 5	10 ± 3	1.3 ± 0.3
Qubit 2	8 ± 1	9 ± 2	1.3 ± 0.3	8 ± 2	6 ± 1	0.6 ± 0.2

Table 4.1: Relaxation time T_1, Hanh echo T_2 time, T_2^* time and their statistical values for both qubit. The errors in this table are of the statistical type.

4.4 Towards quantum circuits: single-qubit gate calibration

In order to perform single-qubit gates with high fidelity, it is necessary to:

1. calibrate the π-pulse,
2. calibrate the qubit frequency,
3. calibrate the shape of the control pulses.

For what concerns the calibration of the π-pulse, we exploit the Rabi protocol in Section 2.2.1. This can be achieved by both fixing the amplitude and the power of the control signal, and changing its duration, as reported in Section 4.3, or by fixing the control pulse duration and changing the pulse amplitude. Once the π-pulse has been calculated through Rabi oscillations fitting, we use the Ramsey protocol (Section 4.3), which is sensitive to the detuning between the drive and the qubit frequency in order to optimize the drive frequency. This is more evident in Figures 4.15a) and 4.15c), where the Ramsey fringes for qubit 0 and qubit 2 are shown, respectively. The red lines highlight on-resonance Ramsey interferometry, while the orange lines represent examples of off-resonance. In Figures 4.15b) and 4.15d), it is possible to observe the cross-section of the measurements highlighted in red and orange in panels a) and c).

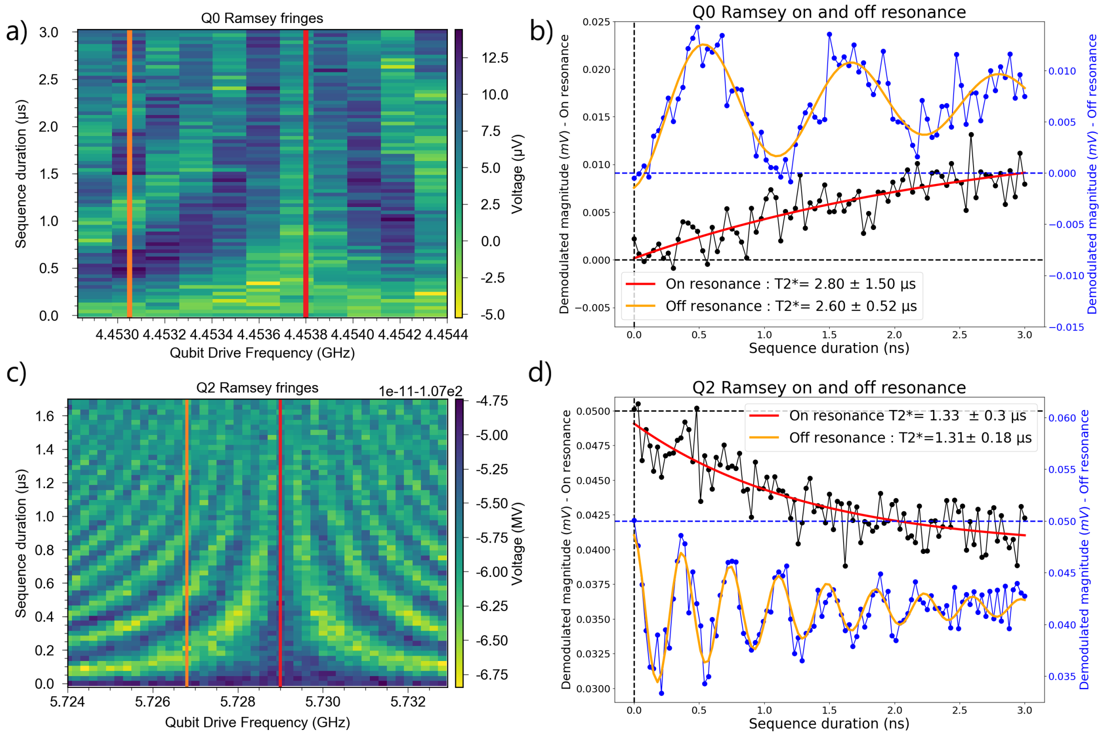

Figure 4.15: In a) Ramsey fringes for qubit 0; b) cross sections at the frequencies highlighted in panel a); c) Ramsey fringes for qubit 2; d) cross sections at the frequencies highlighted in panel c). In panels a) and c), the red lines represent the on-resonance Ramsey interferometry, while the orange lines are examples of off-resonance Ramsey interferometry. In panel b), the black and blue lines represent the measured voltage of the on and off resonance cross-sections highlighted in panel a), respectively. In panel d), the black and blue lines represent the measured voltage of the on and off resonance cross-sections highlighted in panel c), respectively. In panels b) and d), the red and orange lines represent the fit of the on and off resonance cross sections, respectively. The blue y-axis on the right represents the demodulated magnitude for the off-resonance cross section, while the black y-axis on the left represents the on-resonance cross section.

Finally, the last protocol used for pulse calibration is the AllXY. This protocol involves applying different combinations of one or two single-qubit gates. By analyzing the error syndrome, i.e. the deviation from the ideal response, it is possible to identify the nature and characteristics of the errors affecting the system, as discussed in Section 2.3.1. The AllXY performed on qubit 0 and qubit 2 are shown in figure 4.16a) and 4.16b), respectively.

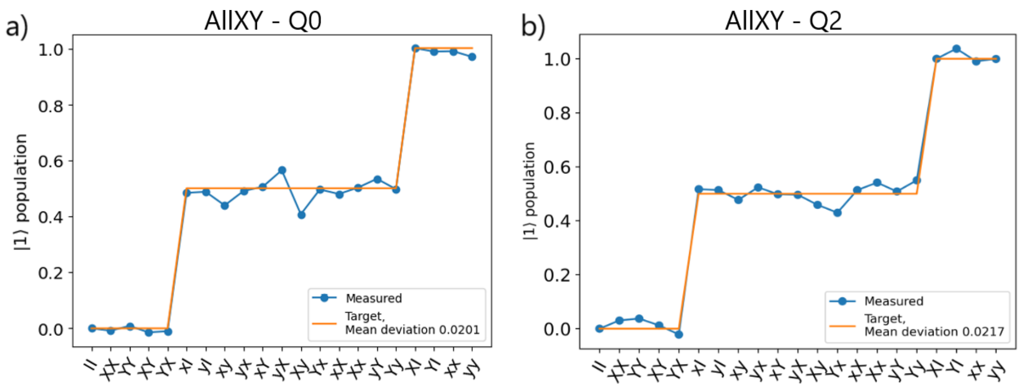

Figure 4.16: AllXY protocol for a) qubit 0 and b) qubit 2. On the x-axis, there are the gates combinations, while on the y-axis there is the population of the first excited state. The blue line is the measured output and the orange line the ideal output. Please note that we use uppercase letters for control pulses with rotation angles of π, and lowercase letters for $\pi/2$ rotations.

According to Section 2.3.1, the zig-zag-like behavior arising in the center of the plot indicates a detuning-related error syndrom [14], which occurs when the qubit frequency fluctuates due to external noise. This error is consistent with the fact that during these measurements external flux was applied on qubit 0 and qubit 2, respectively. The cryostat's flux lines are not superconducting, resulting in an increase in its base temperature and leading to frequency fluctuations. This phenomenon is demonstrated by the frequency distribution in Figure 4.17, which shows how the resonance frequency changes over time under identical experimental conditions.

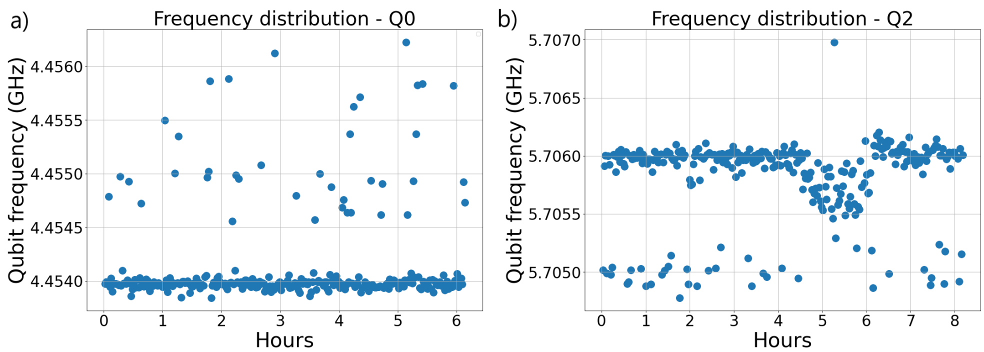

Figure 4.17: Statistical distribution of the detuning for a) qubit 0 and b) qubit 2 for a time period of 6-8 hours, under the same experimental conditions.

Using the AllXY protocol, it is also possible to estimate the DRAG coefficient, known as the *Motzoi coefficient*. For this measurement, it is necessary to identify two gate combinations with different syndrome signs. Considering the two combinations $X(\pi)Y(\pi/2)$ and $Y(\pi)X(\pi/2)$ with different detuning syndrome signs, according to table 2.11 in Section 2.3.1, the optimal Motzoi coefficient is given by the intersection between the slopes of the readout voltage magnitude measured for the two pulses sequences (blue and red in Figure 4.18, respectively), as a function of the DRAG scaling factor.

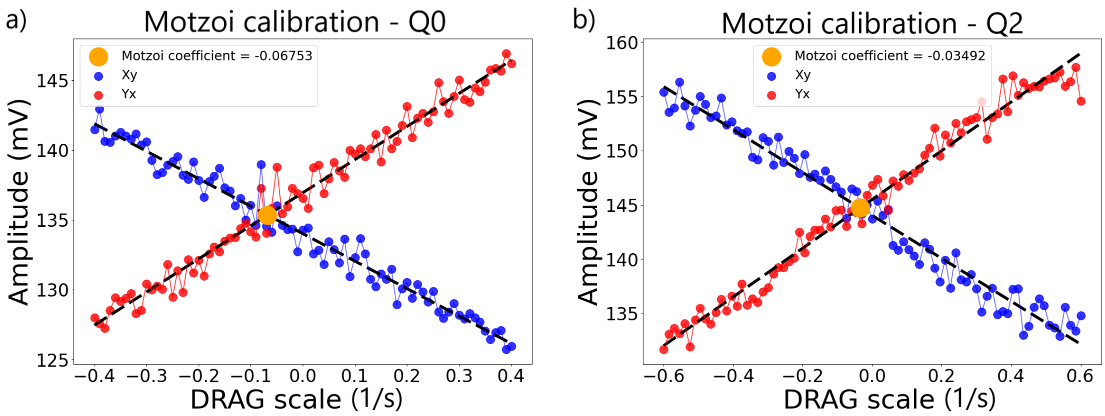

Figure 4.18: Example of Motzoi coefficient calibration. Intersection of the two lines obtained by varying the DRAG (Derivative Reduction by Adiabatic Gate) coefficient of gates combination $X(\pi)Y(\pi/2)$ and $Y(\pi)X(\pi/2)$ with opposite syndrome sign for a) qubit 0 and b) qubit 2. The intersections represent the optimal DRAG coefficient values.

All the described protocols have been iteratively implemented at least 2 or 3 times, as it is tipically done also in literature [14], and the finals Motzoi values are are $-0.0746 \cdot 1/s$ for qubit 0 and $-0.0409 \cdot 1/s$ for qubit 2.

4.5 Two-qubit gates calibration: the CZ gate

Once the single-qubit gate pulses have been properly calibrated, we performed the pulse calibration of the CZ gate. The CZ experiment requires to excite both the qubits, so that the system is in $|11\rangle$. We fix the qubit 0 in its flux SS and we change the flux pulse amplitude and duration on qubit 2. The results of this experiment measuring the qubit 0 and qubit 2 are shown in panels a) and b) of figure 4.19.

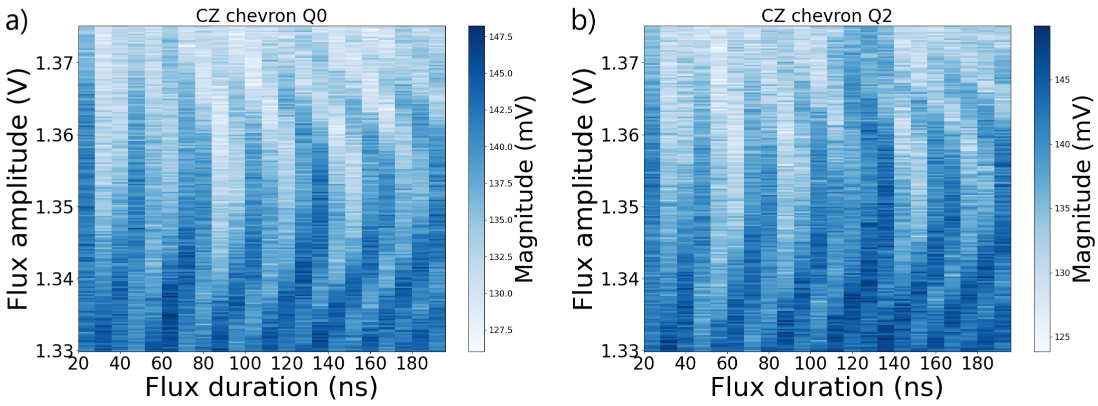

Figure 4.19: Chevron plots for the CZ experiment. On the x-axis the duration of the flux pulse on qubit 2, on the y-axis the magnitude flux applied and the color scale is the demodulated magnitude of the readout resonators of a) qubit 0 and b) qubit 2. We perform a simultaneous measurement of both qubits.

The measurements are conducted simultaneously on both qubits by sending a two-tone signal into the feedline. The first tone is tuned to resonate with resonator 0, and the second tone with resonator 2. We extrapolate the oscillations at a fixed flux voltage pulse amplitude, as shown in figure 4.20a).

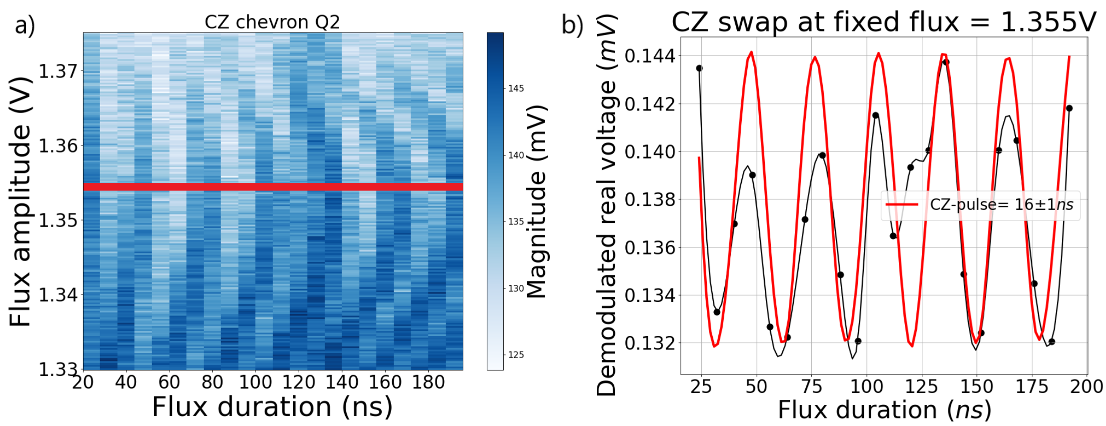

Figure 4.20: In a) the Chevron plot for the CZ experiment measured on qubit 2. The red line identifies the line-cut corresponding to $1.355V$; b) line-cut plot, which is fitted with a Rabi-like function in order to get an estimation of the CZ gate duration time. The resolution of experimental data in b) is limited by the room-temperature electronics time-grid signal generation of $4ns$.

We use the approach of Rabi oscillations to find an estimation of the CZ gate duration time. Hence, we fit with $a \sin(bx + c) + d$ and results are reported in figure 4.20b). The oscillations between the $|11\rangle$ and $|02\rangle$ states happen approximately in $(16 \pm 4)ns$. The oscillations shown in figure 4.19 are actually corrected from distortions, using an hardware solution called *Cryoscope* [93], which employs a series of filters. The distortions can be due to many factors. A very common problem is the shape of the signal that we use for the flux biasing. The pulse used to implement the CZ gate is an unipolar pulse [57], which has a finite rise time. Moreover, the electronics generates signals which are not exactly square pulses and this can cause deviations in the measured response. This behaviour becomes particularly important when the CZ duration is short.
Finally, in order to optimize the CZ pulse parameters, we perform a conditional oscillation experiment. According to Section 2.6, the conditional oscillation experiment consists in two variants of the same experiment. For the Off variant, the target qubit, i.e. qubit 0, is prepared on the equator by a $\pi/2$-pulse, while the control qubit is left in the ground state. Then the CZ flux pulse is applied, followed by another $\pi/2$-pulse. Finally, the states of both qubits are measured simultaneously. For the On variant, the pulses on the qubit 0 are the same as the Off variant, but on the control, i.e. qubit 2, is applied a π-pulse each time a $\pi/2$-pulse is applied on qubit 0 (Section 2.6). If the phase difference between the readout signals measured on the target in the two configurations is not 180 degrees, the parameters of the CZ gate are iteratively changed until this value is achieved. At the same time, the measurement on the control allows us to estimate the leakage, i.e. the probability that a random computational state leaks out of the computational subspace. The optimal amplitude and duration parameters of the CZ pulse are the ones for which the phase difference is as close as possible to 180 degrees, while at the same time minimizing the leakages. The result of the best measurement for the conditional oscillation experiment is shown in figure 4.21.

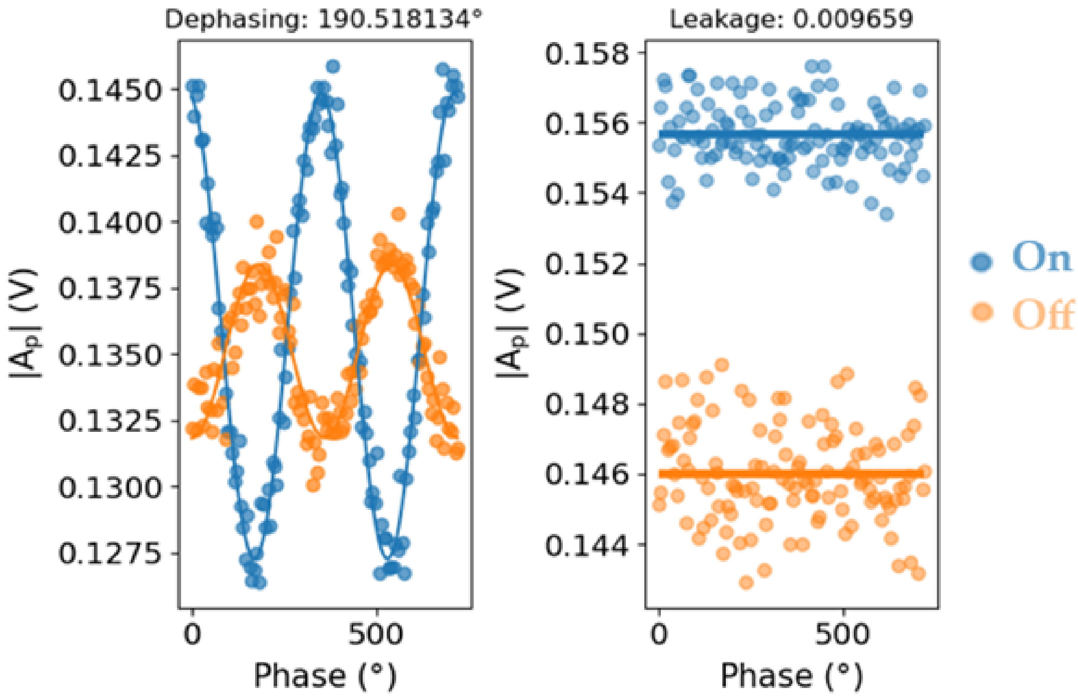

Figure 4.21: The measured voltage as a function of the phase on the qubit 0 on the left and on qubit 2 on the right. The blue lines represent the measured values for the On variant, while the orange lines the measured values for the Off variant.

The phase difference $\theta_{2Q} \simeq 191^{\circ}$ and the leakage $L \simeq 9.66mV$.

4.6 Readout of qubit state

Before analyzing quantum circuits, it is necessary to read out the qubit states. The states $|0\rangle$ and $|1\rangle$ can be measured in the I-Q plane for both qubits. According to Section 2.8, in order to assign a binary value corresponding to the outcome of the qubit measurement, we choose an assignment threshold, which best separates the prepared states of the qubit. To choose the threshold, we prepare the qubit in the $|0\rangle$ state and then in the $|1\rangle$ state. The outputs obtained are two blobs, in blue and orange in Figure 4.22, respectively. The midpoint of the line connecting the centers of the two blobs allows to define a discrimination line (dashed line in Figure 4.22), which identifies a threshold.

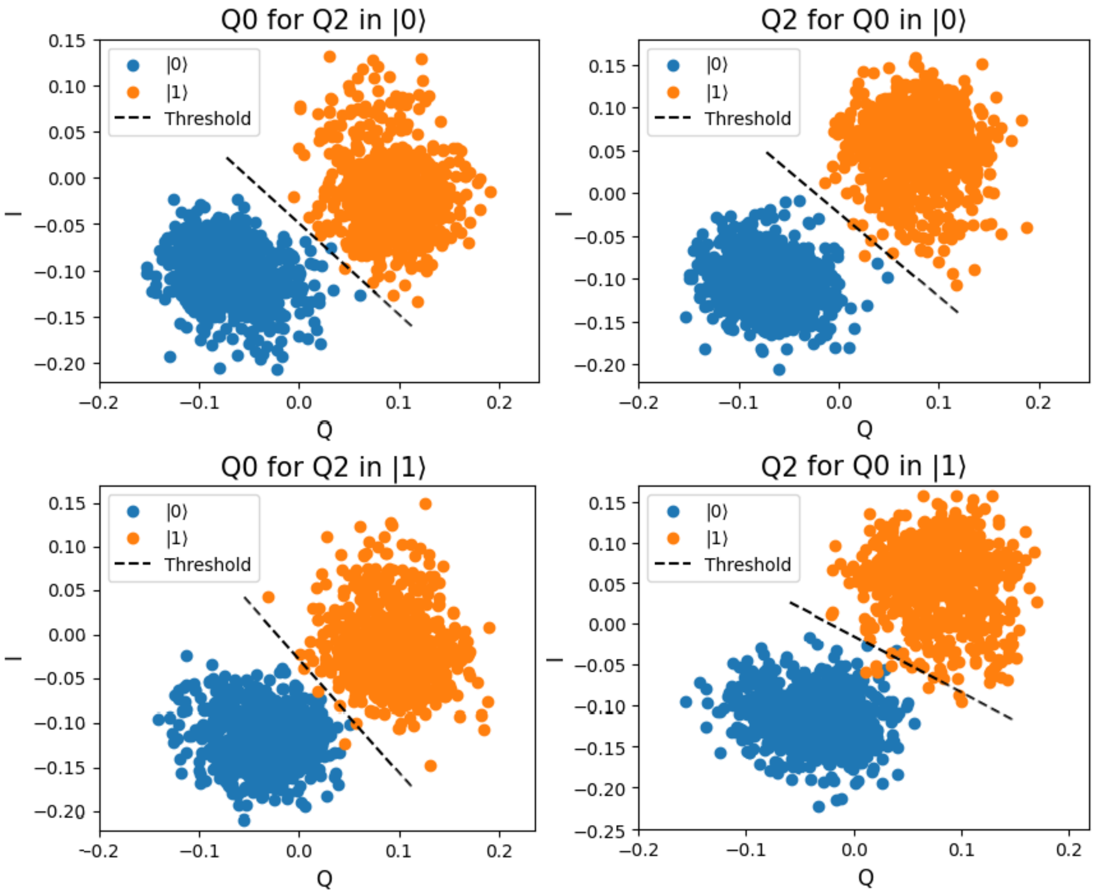

Figure 4.22: In figure the measurement and threshold choosing process is shown for a) qubit 0 with qubit 2 in the ground state, b) qubit 2 with qubit 0 in the ground state, c) qubit 0 with qubit 2 in the excited state, d) qubit 2 with qubit 0 in the excited state. The blue and the orange dots correspond to the measurements of the qubit prepared in the ground and excited states, respectively. The black dashed line represents the threshold.

For single qubit initialization, each qubit is first prepared in the ground state and then in the excited state, keeping the coupled qubit in the ground or excited states. In both cases, the output state is measured simultaneously on the two qubits. This experiment and all the following ones were conducted with 760 shots. The single-qubit readout measurements when preparing the coupled qubit in either the ground or excited states should be equal, as the preparation of one qubit in a state should not affect the other. This approximate equality is demonstrated in Figure 4.23a) and b), and c) and d) for qubit 0 and qubit 2, respectively.

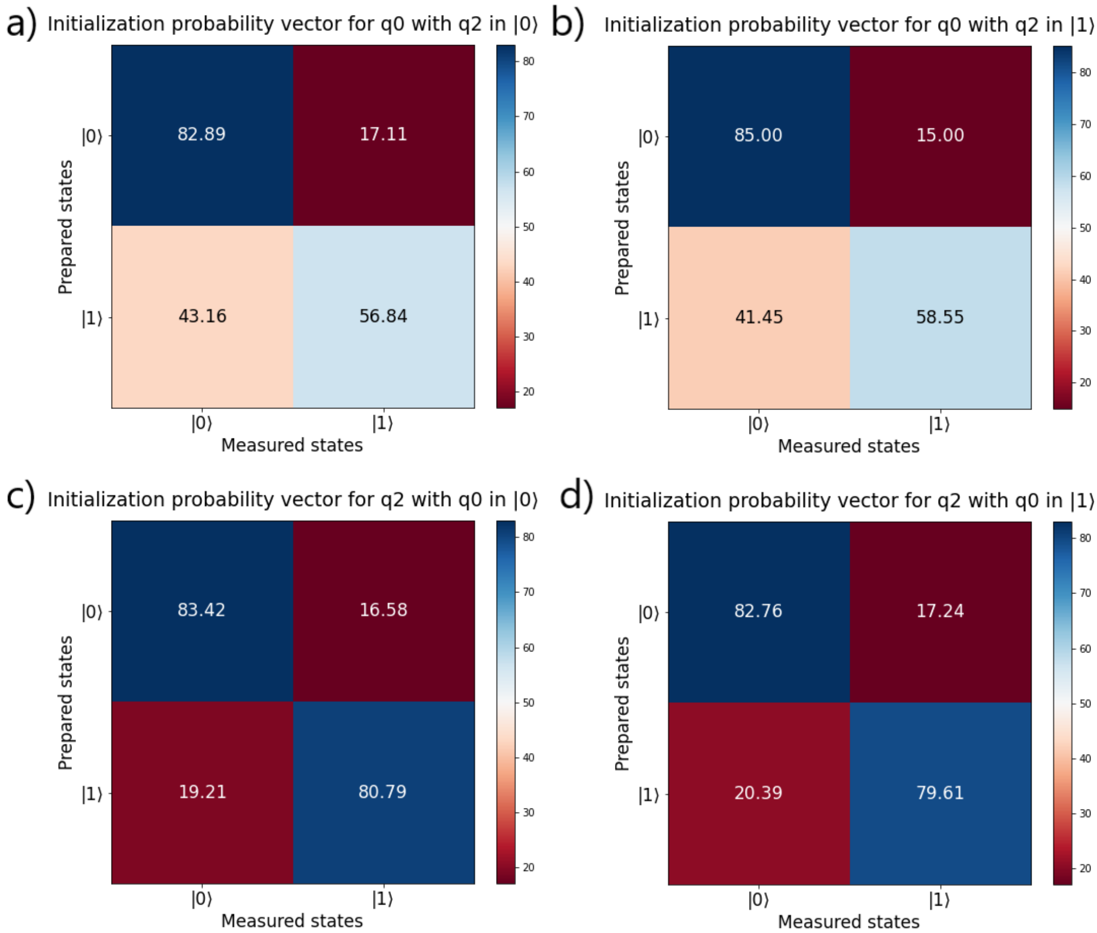

Figure 4.23: Probability matrices for single qubit initialization. At the top of the figure, qubit 0 is initialized with qubit 2 in a) the ground state and b) the excited state, while at the bottom, qubit 2 is initialized with qubit 0 in c) the ground state and d) the excited state.

More in detail, in Figure 4.23a), it is possible to see that if qubit 0 is prepared in the ground state, the probability of measuring the ground state as the output is 83%, while the probability of measuring the excited state is 17%. This is in agreement with literature, where the typical values of readout fidelity range from $\sim 70\%$ to $\sim 99\%$ [94][95]. However, if qubit 0 is prepared in the excited state, the probability of measuring the ground state as the output is 43%, and the excited state is 57%. As a result, the readout fidelity is sufficiently high when the qubit is prepared in the ground state, but it is lower when it is prepared in the excited state. This result is confirmed in Figure 4.23b). At the time of this work, the dependence of the readout fidelity on the initial state preparation of qubit 0 is unclear. Further studies must be done in order to outline the motivations behind this effect. For qubit 2, as shown in Figures 4.23c) and 4.23d), the probability of measuring the prepared state is $\sim 80\%$ for both the ground and the excited states, regardless of the preparation of qubit 0. Therefore, the fidelity for qubit 2 is in agreement with literature [97]. Finally, for what concerns two-qubit initialization, reported in Figure 4.24, the states in which the system can be prepared are $|00\rangle, |01\rangle, |10\rangle$ and $|11\rangle$, where the first label refers to qubit 0 and the second to qubit 2. In this case as

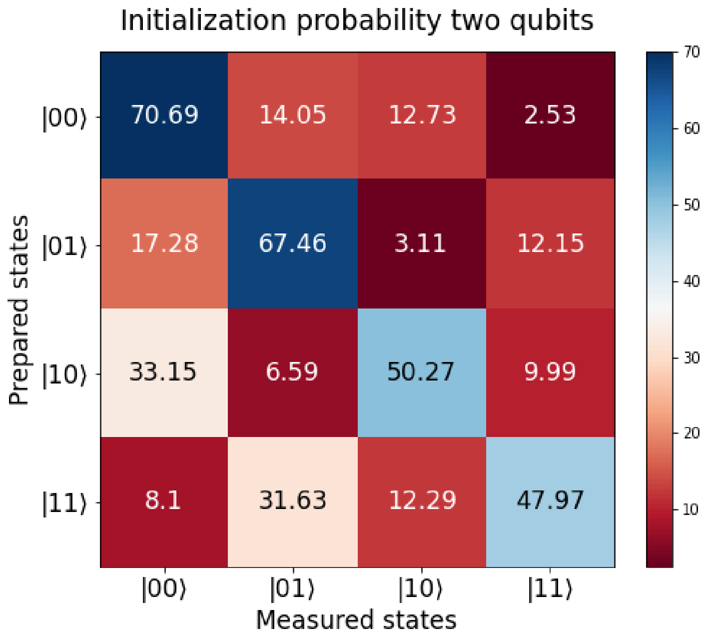

Figure 4.24: The probability matrix for two-qubit initialization. The first label is referred to qubit 0, while the second to qubit 2.

well, we can observe that as long as qubit 0 is prepared in the ground state, we have a readout fidelity that is roughly in agreement with the results reported in the literature [97]. Indeed, if we prepare the system in the state $|00\rangle$, we have a 70% probability of measuring the state $|00\rangle$, while if we prepare the state $|01\rangle$, we have a 67% probability of measuring the state $|01\rangle$. On the other hand, if we prepare qubit 0 in the excited state, the readout fidelity drops even below 50%. As we will see in Section 4.7.2, this will influence the efficiency of the quantum circuits that we will implement.

4.7 Quantum circuits and Hellinger fidelity

After qubit characterization and pulses calibration, the final aim is to estimate the Hellinger fidelity [96] for the quantum circuits implemented, which is analogous to the fidelity for classical probability distributions. The Hellinger fidelity is defined as [96]:

$$H(p,q) = \left[\sum_{i=1}^{n} \sqrt{p_i q_i}\right], \tag{4.1}$$

where p and q are the two probability distributions, and can be written in terms of the Hellinger distance HD as [96]:

$$H(p,q) = (1 - HD^2)^2, \tag{4.2}$$

where HD is defined as:

$$HD = \frac{1}{\sqrt{2}} \sqrt{\sum_{i=1}^{n} (\sqrt{p_i} - \sqrt{q_i})^2}. \tag{4.3}$$

According to literature, typical values of Helliger distance range between 0.1 and 0.4, which leads to an Hellinger fidelity between $\sim 98\%$ and $\sim 70\%$ [97]. Specifically, the Hellinger fidelity is calculated in terms of the experimental probability readout state vector output of a quantum circuit for the device and the expected theoretical probability readout state vector for the same quantum circuit. The probability readout state vector is measured following the technique reported in Section 4.6. First, we will show the results on the quantum circuits with single-qubit gates and two-qubit gates. Then, the results will be discussed and compared.

CNOT circuit

The first quantum circuit implemented is the CNOT circuit, whose pulse scheme is shown in figure 4.25. This pulse sequence is repeated initializing the system in each of the four possible states of the computational basis $\{|00\rangle, |01\rangle, |10\rangle, |11\rangle\}$. It is crucial to note that the states of the system are represented as $|CT\rangle$, where C stands for control and T for target. Specifically, qubit 0 works as the target qubit, and qubit 2 as the control qubit. This choice explicitely takes into account the coherence times of the two qubits analyzed (Section 4.3). The control qubit in the CNOT gate defines the final outcomes of the gate: if prepared in $|0\rangle$, indipendently on the target state, the output is ideally unchanged; however, if prepared in $|1\rangle$, it induces a bit-flip in the target state. Therefore, the probability of success of the gate strongly depends on the coherence stability of the target qubit, which must not uncoherently change its state during the gate time.

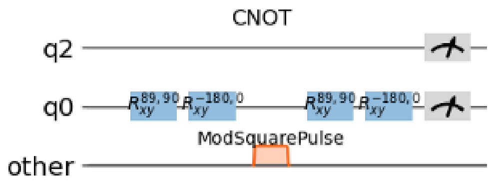

Figure 4.25: The CNOT circuit pulse scheme. An $Y(\pi/2)$ is applied on qubit 0, followed by a $X(\pi)$. Then, a CZ gate is performed. Once again, $Y(\pi/2)$ and $X(\pi)$ are applied on qubit 0. Finally, the state of both qubits is simultaneously measured. The CZ pulse is represented by the orange square pulse.

In the two-qubit register here analyzed, qubit 0 has longer coherence times than qubit 2 (Section 4.3). The ideal probability matrix for the CNOT circuit for each initial state is shown in Figure 4.26a), while in panel b), the measured probability matrix for the same experiment is shown.

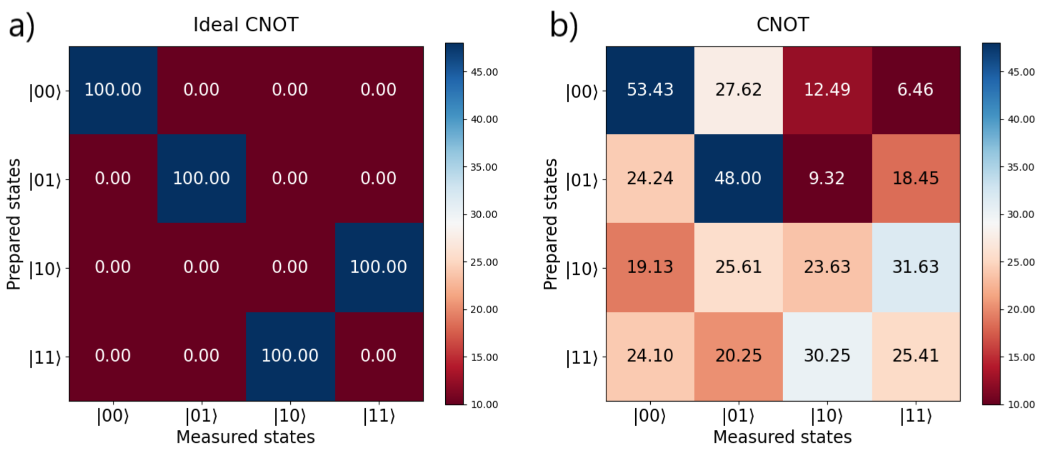

Figure 4.26: In a) the ideal probability matrix and b) the measured probability matrix for the CNOT experiment. The color bar represents the probability distribution. The first label of the states refers to qubit 2, while the second to qubit 0.

According to Figure 4.26a), if we prepare the system in $|00\rangle$, the probability of measuring the same state is 100%. However, this state is measured with a 53% probability, as shown in Figure 4.26b). Moreover, as expected from readout fidelity (Section 4.6), when the qubit 0 is prepared in the excited state, the probability of measuring the expected states drops to $\sim 30\%$ (Figure 4.26b)). Fidelities of this order of magnitude suggest that we have incorrect results in almost the majority of cases.

CNOT+H circuit

Another circuit implemented is the CNOT+H circuit, whose pulse scheme is shown in figure 4.27.

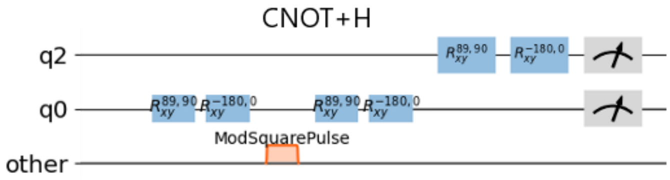

Figure 4.27: The CNOT+H circuit pulse scheme. The CNOT pulse scheme is composed of $Y(\pi/2)$ and an $X(\pi)$, applied on qubit 0, then a CZ gate is performed, and once again, $Y(\pi/2)$ and $X(\pi)$ applied on qubit 0. The Hadamard gate, applied on qubit 2, is composed of an $Y(\pi/2)$, followed by $X(\pi)$. The CZ pulse is represented by the orange square pulse.

The ideal and the measured probability matrix for the CNOT+H experiment performed on each state of the system are shown in figure 4.28.

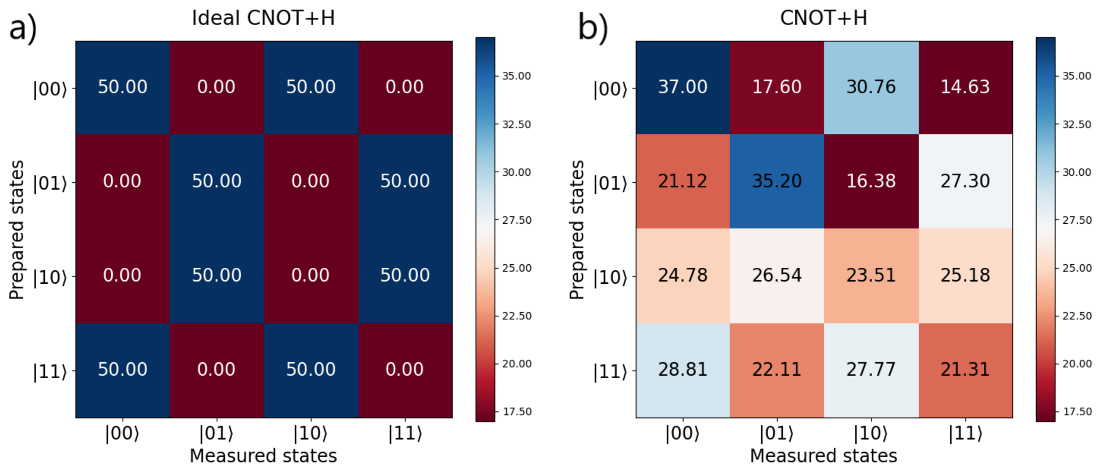

Figure 4.28: In a) the ideal probability matrix and b) the measured probability matrix for the CNOT+H experiment. The color bar represents the probability distribution. The first label of the states refers to qubit 2 and the second to qubit 0.

According to Figure 4.28a), if we prepare the system in $|00\rangle$, we expect to measure $|00\rangle$ and $|10\rangle$ states, both with a probability of 50%. The $|00\rangle$ and $|10\rangle$ states are measured with a probability of 37% and 31%, respectively, as shown in Figure 4.28b). Using equation 4.2, it is possible to obtain the Hellinger fidelity. Therefore, when the system is prepared in $|00\rangle$, $|01\rangle$, $|10\rangle$ and $|11\rangle$, the Hellinger fidelietis are 68%, 62%, 52% and 57%, respectively. These values are fairly close to the ones typically found in literature [97]. Even if the CNOT+H quantum circuit uses nominally the same CNOT gate as in the CNOT circuit, its Hellinger fidelity is counterintuitevely larger. Indeed, one would expect to accumulate control errors when increasing the number of gates in a quantum circuit, thus reducing the quality of the output. Qualitatively, the relative improvement of the Hellinger fidelity may be accounted for the introduction of the Hadamard gate at the end of the sequence, which induces a superposition between $|01\rangle$ and $|11\rangle$ states for the initial state $|10\rangle$, and between $|00\rangle$ and $|10\rangle$ for the initial state $|11\rangle$. The CNOT experimental output in Figure 4.26b) suggests that the system naturally tends to reach a superposition state, as the one predicted for the CNOT+H circuit in Figure 4.28b). Further studies are required in order to understand the origin of this effect.

First random single-qubit gate circuit

The first random single-qubit gate circuit is composed of single-qubit gates generated randomly from a set of Clifford single-qubit gates [98]. According to the pulse scheme, shown in figure 4.29, $Y(\pi/2)$ pulse is applied on qubit 0, followed by an $X(\pi)$ pulse. After that, a $Y(\pi)$ pulse is applied on qubit 2.

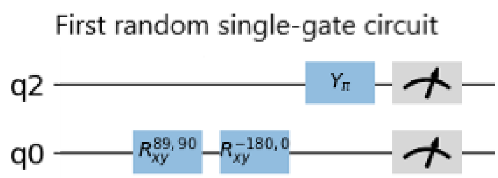

Figure 4.29: First random single-qubit gate circuit pulse scheme. An $Y(\pi/2)$ pulse is applied on qubit 0, followed by an $X(\pi)$ pulse. After that, on qubit 2 is applied an $Y(\pi)$ pulse. Finally, the state of both qubit is simultaneously measured.

The ideal and measured probability matrix for the random single-gate experiment performed on each state of the system are shown in figure 4.30.
According to Figure 4.30a), if we prepare the system in $|00\rangle$, we expect to measure $|01\rangle$ and $|11\rangle$ states, both with a probability of 50%. The $|01\rangle$ and $|11\rangle$ states are measured with a probability of 36% and 34%, respectively, as shown in Figure 4.30b). The estimated Hellinger fidelities are 70%, 72%, 70% and 72% for $|00\rangle$, $|01\rangle$, $|10\rangle$ and $|11\rangle$, respectively. These values are in agreement with the ones typically found in literature [97].

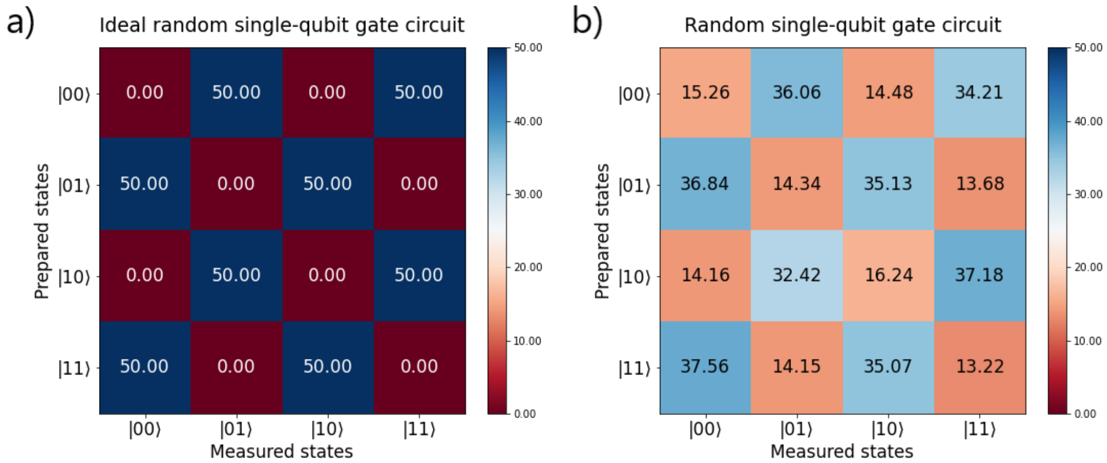

Figure 4.30: In a) the ideal probability matrix and b) the measured probability matrix for random single-qubit gate circuit. The color bar represents the probability distribution. The first label of the states refers to qubit 0 and the second to qubit 2.

Second random single-qubit gate circuit

The second random single-qubit gate circuit is also composed of single-qubit gates generated randomly from a set of Clifford single-qubit gates [98]. According to the pulse scheme, shown in figure 4.31, a Hadamard gate is performed on qubit 0. After that, on qubit 2 is applied an $X(\pi/4)$ pulse, followed by $X(\pi)$ pulse.

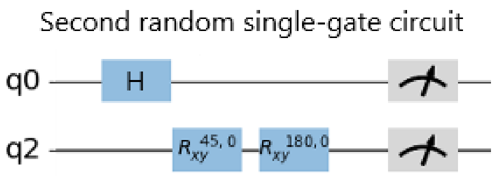

Figure 4.31: Second random single-qubit gate circuit pulse scheme. A Hadamard gate is applied on qubit 0. After that, on qubit 2 is applied an $X(\pi/4)$ pulse, followed by $X(\pi)$ pulse. Finally, the state of both qubit is simultaneously measured.

The ideal and measured probability matrix for the second random single-gate circuit performed on each state of the system are shown in figure 4.32.

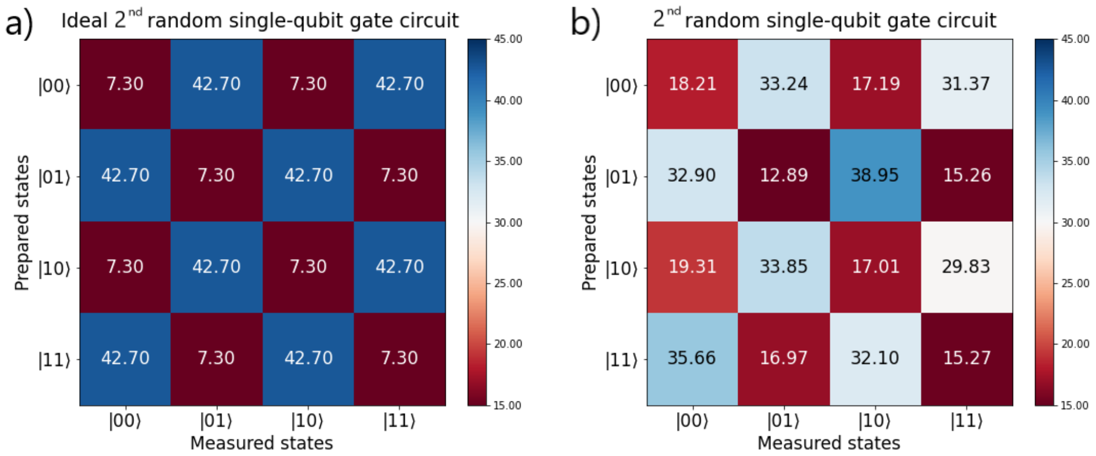

Figure 4.32: In a) the ideal probability matrix and b) the measured probability matrix for the second random single-qubit gate circuit. The color bar represents the probability distribution. The first label of the states refers to qubit 0 and the second to qubit 2.

According to Figure 4.32a), if we prepare the system in $|00\rangle$, we expect to measure $|00\rangle$ and $|10\rangle$ states, both with a probability of 7%, and $|01\rangle$ and $|11\rangle$, both with a probability of 43%. The measured probability are 18%, 33%, 17% and 31% for $|00\rangle$, $|01\rangle$, $|10\rangle$ and $|11\rangle$, respectively, as shown in Figure 4.32b). The corresponding Hellinger fidelities are 94%, 97%, 94% and 96%. Hellinger fidelities above 90% are indicative of high-quality quantum circuits output [97].

4.7.1 Bell circuit

The last circuit implemented is the one used to create Bell states, which are four specific maximally entangled quantum states of two qubits [100]. They are in a superposition of $|0\rangle$ and $|1\rangle$. More specifically, the Bell states are [101]:

$$\left|\Phi^+\right\rangle = \frac{1}{\sqrt{2}}(|0\rangle \otimes |0\rangle + |1\rangle \otimes |1\rangle), \tag{4.4}$$

$$\left|\Phi^-\right\rangle = \frac{1}{\sqrt{2}}(|0\rangle \otimes |0\rangle - |1\rangle \otimes |1\rangle), \tag{4.5}$$

$$\left|\Psi^+\right\rangle = \frac{1}{\sqrt{2}}(|0\rangle \otimes |1\rangle + |1\rangle \otimes |0\rangle), \tag{4.6}$$

$$\left|\Psi^-\right\rangle = \frac{1}{\sqrt{2}}(|0\rangle \otimes |1\rangle - |1\rangle \otimes |0\rangle). \tag{4.7}$$

The circuit used to generate the Bell states is composed of a Hadamard gate applied on the control qubit, followed by a CNOT gate, as shown in figure 4.33.

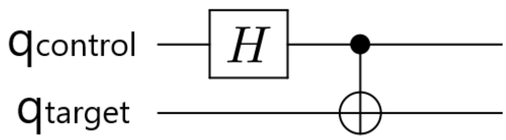

Figure 4.33: The pulse scheme of the Bell states circuit. A Hadamard gate is applied on the control qubit, followed by a CNOT gate.

Specifically, the circuit used to reproduce Bell states is an equivalent circuit, whose pulse sequence is shown in figure 4.34.

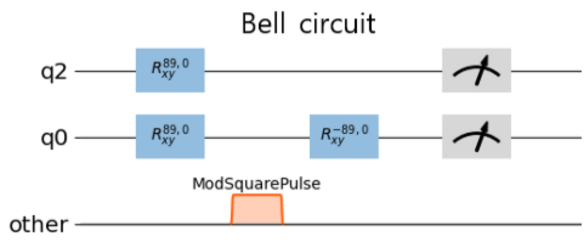

Figure 4.34: Pulse scheme of the equivalent circuit of the Bell state circuit. On qubit 2, an $X(\pi/2)$ is applied. Then, a CNOT gate is performed, using an $X(\pi/2)$ pulse on qubit 0, CZ pulse and an $X(3\pi/2) = X(-\pi)$ on qubit 0. The CZ pulse is represented by the orange square pulse.

The Hadamard gate on the control qubit in the original Bell circuit is replaced by $X(\pi/2)$. Moreover, remembering that the CNOT is implemented using two Hadamard gates and a CZ gate in the middle of them, it is fundamental to notice that the first Hadamard in the CNOT has been replaced by a $X(\pi/2)$ pulse, while the second by a $X(3\pi/2) = X(-\pi)$. This replacement is supported by other cloud platforms, such as Quantum Inspire [102].
In order to obtain the Bell states, the Quantum State Tomography was carried out with 1024 shots. The pulse used to implement the CZ gate is the Sudden Net Zero (SNZ), shown in figure 4.35.

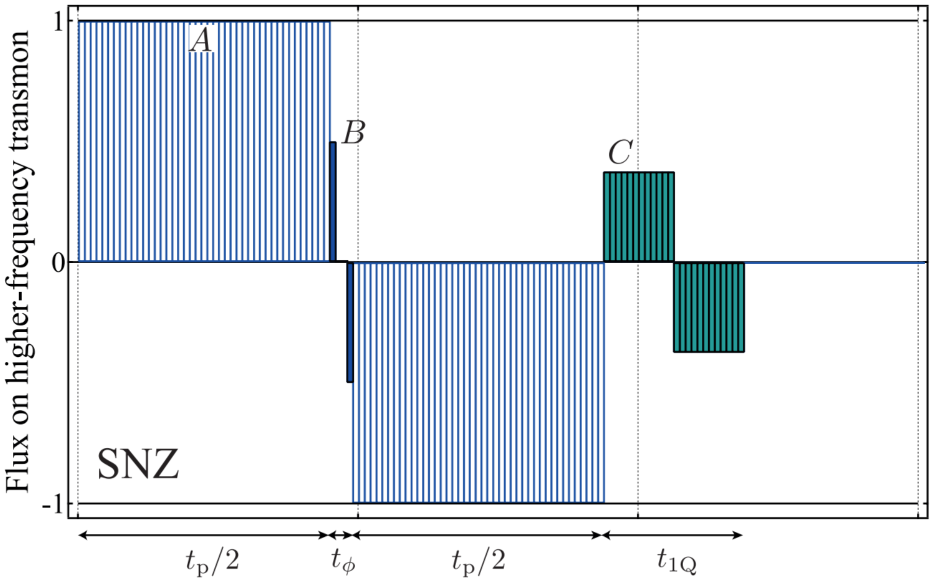

Figure 4.35: The Sudden Net Zero (SNZ) pulse consists of two back-to-back strong half-pulses of duration $t_p/2$ each (in blue), followed by weak bipolar pulses of total duration t_{1Q} to null single-qubit phases (in dark green). t_ϕ is the intermediate idling period. The amplitude ($\pm A$) is jointly tuned to set the conditional phase θ_{2Q} at minimal leakage L. The amplitude $\pm B$ of the first and last sampling points in t_ϕ and the number of intermediate zero-amplitude points provide fine and coarse control of this relative phase, respectively. The amplitude $\pm C$ of the weak pulses is used to null the single-qubit phase on the higher-frequency transmon. Adapted from [99].

It consists of two back-to-back strong half-pulses of duration $t_p/2$ each, followed by weak bipolar pulses of total duration t_{1Q} to null single-qubit phases. Also, an intermediate idling period t_ϕ is added to accrue relative phase ϕ between $|02\rangle$ and $|11\rangle$.
The Bell experiment uses Quantum State Tomography [103][104], a process used to determine the density matrix of the quantum state of an unknown quantum system. It involves measuring a complete set of observables, whose expectation values determine the quantum state [105][106]. In figure 4.36, the real parts of the measured density matrices of the two-qubit system are shown, which provide information about the probability of finding the quantum system in a specific quantum state. More in detail, the state tomography shows that if the system is prepared in $|00\rangle$ and a Bell experiment is performed, the output state is a combination of $|00\rangle$ and $|11\rangle$ (as shown in figure 4.36a)).

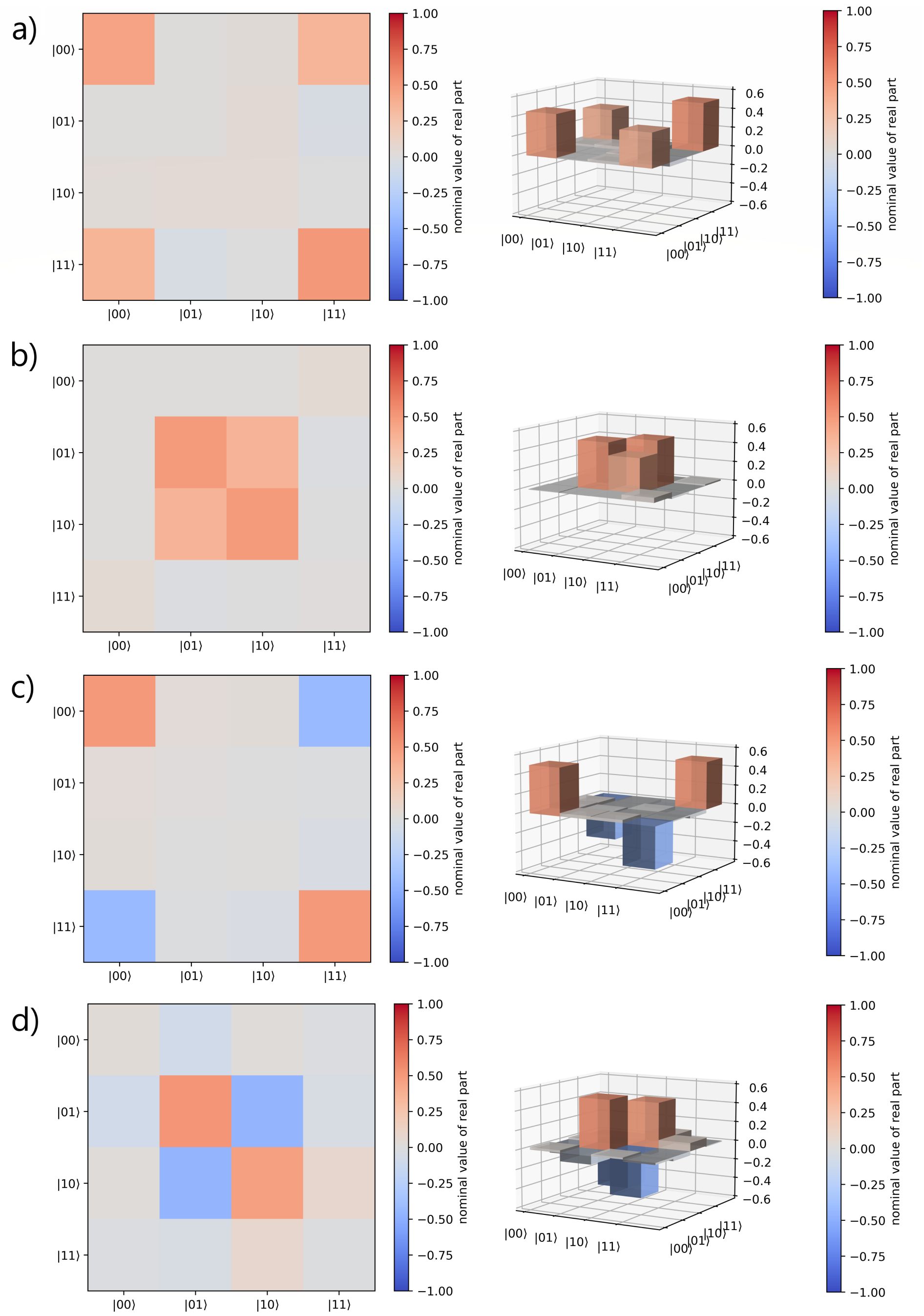

Figure 4.36: Bell state tomography. On the left, the real parts of the measured density matrices in 2D for Bell state a) Φ^+, b) Ψ^+, c) Φ^- and d) Ψ^-. On the right, the same measurement in 3D.

If the system is prepared in $|10\rangle$, the output is composed of the same previous states, but $|00\rangle$ and $|11\rangle$ have different signs, as shown in figure 4.36c). On the other hand, if the system is prepared in $|01\rangle$ or $|11\rangle$, the output states in both cases are $|01\rangle$ and $|10\rangle$. In the first case, the $|01\rangle$ and $|10\rangle$ have the same signs (figure 4.36b)), while in the second they have opposite signs (figure 4.36d)). These results are in agreement with the equation 4.4, 4.5, 4.6 and 4.7 when system is prepared in $|00\rangle$, $|01\rangle$, $|10\rangle$ and $|11\rangle$, respectively. From the real part of the density matrix, it is possible to roughly estimate the probability matrix for the Bell circuit and, consequently, the Hellinger fidelity. The ideal and estimated probability matrix for the Bell circuit performed on each state of the system are shown in figure 4.37.

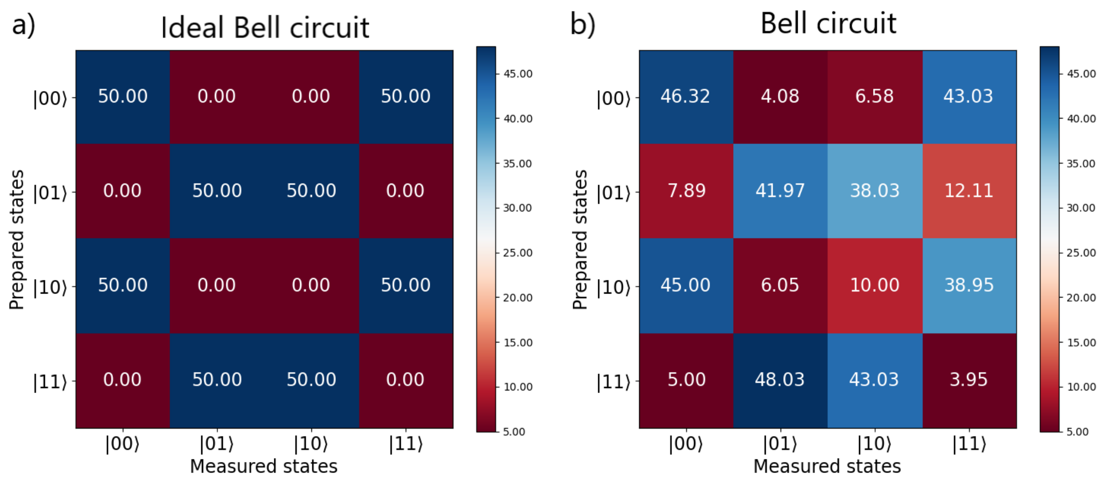

Figure 4.37: In a) the ideal probability matrix and b) the estimated probability matrix for the Bell circuit. The color bar represents the probability distribution. The first label of the states refers to the control and the second to the target.

4.7.2 Quantum circuits summary

In table 4.2, the results of the calculated Hellinger Fidelity for the quantum circuits are reported.

	Circuit	Prepared state			
		$\|00\rangle$	$\|01\rangle$	$\|10\rangle$	$\|11\rangle$
Hellinger fidelity for	CNOT	53.43%	48.00%	31.63%	30.25%
	CNOT+H	67.62%	62.25%	51.70%	56.57%
	1^{st} random single-qubit gate	70.25%	71.96%	69.52%	72.61%
	2^{nd} random single-qubit gate	94.09%	97.05%	93.56%	95.52%
	Bell	89.31%	79.95%	83.84%	90.98%

Table 4.2: The Hellinger fidelity for CNOT, CNOT+H, 1^{st} random single-qubit gate, 2^{nd} random single-qubit gate and Bell experiment.

According to literature, typical values of Hellinger fidelity range between $\sim 98\%$ and $\sim 70\%$ [97]. For the CNOT+H, random single-qubit gate and Bell circuits, the Hellinger fidelity is fairly close to the ones typically found in literature, while for the CNOT circuit the Hellinger fidelity is slighlty above 30% when preparing the control in the excited state, and around 50% when preparing the control qubit in the ground state. Fidelities of this order of magnitude suggest that we have incorrect results in almost the majority of cases. This can be related to different problems. First of all, the readout fidelity when qubit 0 is excited is just of 50% (see figure 4.24). Secondly, the spread in the qubit frequency in figure 4.17 due to frequency fluctuations and decoherence possibly cause an insufficient quality of single-qubit gate circuits. This, together with the low coherence times of qubit 2, makes the system sensitive to dissipation channels. However, for the single-qubit gate circuits, the Hellinger fidelities are larger than the ones measured when including CNOT gates. Remarkably, for the second random single-qubit gate circuit, the fidelity reaches values above 95%. This suggests that the lower Hellinger fidelities for two-qubit gate circuits is mostly related to the quality of the CNOT gate. Specifically, for these circuits we have used unipolar CZ flux pulses. However, it has been demonstrated that unipolar flux pulses are less efficient than other variants of the same gate, which uses more complicated flux pulse shaping [57][99]. This becomes evident in the Bell experiment, where the SNZ pulse was used instead of the unipolar pulse. The obtained fidelity turns out to be even higher than that of the 1^{st} random single-qubit gate circuit, reaching a fidelity ranging between approximately 80% and 91%. This is an important result, considering that for two-qubit circuits (CNOT and CNOT+H), the maximum fidelity is 67%. Therefore, one possible way to improve the efficiency of quantum circuits can be to explore novel CZ flux pulses shaping and calibration in the near future.

Conclusion

In this thesis, two coupled superconducting transmon qubits in a matrix of 5 coupled qubits have been characterized. Low temperature microwave spectroscopy has been exploited in order to define the readout tone parameters for multiplexed readout on the 2-qubit register: the resonant frequency in the low-photon regime of the dedicated coupled readout resonators, as well as the power needed to guarantee optimal signal to noise ratio and dispersive quantum non demolitive coupling. Moreover, spectroscopy characterization has identified the frequency spectrum of the two qubits when far detuned one to each other (single-qubit regime), and when coupled. Qubit anharmonicities of the order of 200-300MHz, and frequecies of the order of 4.5 GHz to 5.5 GHz, respectively for the two qubits, ensure the typical transmon regime parameters [110]. Specifically, these electrodynamics parameters have been estimated close to the flux-sweet spots, i.e. where sensitivity to flux noise is suppressed.
Time-domain pulsed microwave experiments, instead, are fundamental for single- and two-qubit gates implementation, as well as for the study of the coherence properties of the device. For sufficiently fast single-qubit control gates (few tens of nanoseconds), state-of-the-art relaxation and coherence times range within tens to hundreds of microseconds [111][112]. Rabi oscillation experiments have confirmed the possibility to achieve in our device π-control pulses, i.e. able to excite the qubit from the ground to the excited states, ranging from 20 to 50ns. For these pulses, we have performed statistical and repeated measurements of the relaxation time T_1, and the coherence times T_2^{Echo} and T_2^*, measured through spin Echo and Ramsey interferometry experiments, respectively. The statistical values estimated are $T_1 = (29 \pm 5)\mu s$, $T_2^{Echo} = (10 \pm 3)\mu s$ and $T_2^* = (1.3 \pm 0.3)\mu s$ for the lowest frequency qubit, and $T_1 = (8 \pm 2)\mu s$, $T_2^{Echo} = (6 \pm 1)\mu s$ and $T_2^* = (0.6 \pm 0.2)\mu s$ for the highest frequency qubit. One important conclusion of this work is that the relaxation and coherence times depend on the qubit connectivity: minimal connectivity ensures coherence and relaxation times larger than those measured for maximum connectivity. This is related to the fact that multiple connections between qubits open additional dissipation channels, which affects the coherence.
Control pulses optimization plays a fundamental role in the implementation of gate sequences on a quantum register, which is the main goal of this work. The Ramsey in-

terferometry has been used to optimize the drive frequency since it is more sensitive to detuning between the drive and the qubit frequency compared to the Rabi protocol. The shape of the control pulses has been optimized with state-of-the-art AllXY technique, which involves applying different combinations of one or two single-qubit gates and analyzing the error syndrome, i.e. the deviation from the ideal response. This allows to identify the nature and characteristics of the errors affecting the system. As a result, in our device we have identified a detuning-related error syndrome, which is consistent with resonance frequency fluctuations caused by flux noise.

Once the single-qubit gate pulses have been properly calibrated, we performed the pulse calibration of the CZ gate, one of the most used two-qubit gates in superconducting devices [113][114]. In order to optimize the CZ pulse parameters, we have performed a conditional oscillation experiment, which allows to minimize leakages to non-computational states due to spurious energy interactions between coupled superconducting transmon qubits. All these calibration procedures described above are fundamental to correctly execute quantum gates.

Several sequences of quantum gates, also called *quantum circuits*, have been implemented on the 2-qubit register after calibrating the pulses, involving both single-qubit and two-qubit gates. In order to evaluate the efficiency of our processor, the Hellinger fidelity has been calculated for all the quantum circuits implemented. For single-qubit circuits, fidelities of about 95%, guarantee optimal implementation of the quantum circuit [97]. However, quantum circuits including two-qubit CNOT gates, decomposed in terms of Hadamard and CZ gates, have shown fidelities ranging from 30% to 67%, mostly due to the quality of the CNOT gate. By using more efficient variants of CZ flux pulses that use Sudden Net Zero (SNZ) pulses instead of standard unipolar flux pulses, we have demonstrated through Quantum State Tomography (QST) that the processor allows to reproduce Bell states. This is an important achievement as it's not guaranteed that a processor can generate highly entangled states. The Bell circuit has provided a Hellinger fidelity ranging from 80% to 91%, i.e. it has been demonstrated that improving the quality of the CZ gate is possible to improve the output of two-qubit quantum circuits. In conclusion, in order to guarantee optimal computing performances of superconducting quantum processors, single- and two-qubit gates calibration protocols are mandatory.

Future perspectives include the possibility to address readout and control errors through a comprehensive study of quantum gates and circuits. Indeed, the ability to improve both control and readout techniques through active engineering of the gates sequences in a quantum circuit [107][108] [109] competes with the intrinsic limitation on the number of gates that can be realized in the coherence time of the hardware. A possible solution is to study alternative designs of quantum algorithms schemes and potentially rework the algorithms sequences already proposed in the literature to minimize the number of applicable gates. Reducing the number of gates implies minimizing the overall error in the system, thus enhancing the efficiency of algorithms implementable on the quantum processor.

Bibliography

[1] Arute, F., Arya, K., Babbush, R. et al. Quantum supremacy using a programmable superconducting processor. Nature 574, 505–510 (2019).

[2] S. Leontica, F. Tennie, T. Farrow. *Simulating molecules on a cloud-based 5-qubit IBM-Q universal quantum computer*. Communications Physics 4, Article number: 112 (2021)

[3] Yariv Yanay, Jochen Braumüller, Simon Gustavsson, William D. Oliver, Charles Tahan. *Two-dimensional hard-core Bose–Hubbard model with superconducting qubits*, npj Quantum Information 6, Article number: 58 (2020)

[4] Zhou, Min-Gang ; Liu, Zhi-Ping ; Yin, Hua-Lei ; Li, Chen-Long ; Xu, Tong-Kai ; Chen, Zeng-Bing. *Quantum Neural Network for Quantum Neural Computing*. Research, Volume 6, article id. 0134 (2023).

[5] Mst Shapna Akter. *Quantum Cryptography for Enhanced Network Security: A Comprehensive Survey of Research, Developments, and Future Directions* (2023).

[6] Enrique Martín-López, Anthony Laing, Thomas Lawson, Roberto Alvarez, Xiao-Qi Zhou, Jeremy L. O'Brien. *Experimental realization of Shor's quantum factoring algorithm using qubit recycling*. Nature Photonics 6, 773–776 (2012).

[7] Abhijith J., Adetokunbo Adedoyin at al. *Quantum Algorithm Implementations for Beginners*. ACM Transactions on Quantum Computing, Volume 3, Issue 4, 18 (2022).

[8] David P. DiVincenzo, IBM. *The Physical Implementation of Quantum Computation*. (2008)

[9] Jens Koch et al. *Charge-insensitive qubit design derived from the Cooper pair box*. Physical Review A 76.4 (2007).

[10] T. E. Roth, R. Ma and W. C. Chew. *The Transmon Qubit for Electromagnetics Engineers: An introduction*. IEEE Antennas and Propagation Magazine, vol. 65, no. 2 (2023).

[11] A. Barone, G. Paterno. *Physics and applications of the Josephson effect*. Vol. 1. Wiley Online Library (1982).

[12] C. P. Poole, H. A. Farach, R. J. Creswick e R. Prozorov, *Superconductivity*, Academic Press (1995).

[13] M. Tinkham. *Introduction to Superconductivity*. (Second Edition), McGraw-Hill (1996).

[14] Matthew David Reed *Entanglement and Quantum Error Correction with Superconducting Qubits* (2013).

[15] P. Krantz ; M. Kjaergaard ORCID; F. Yan; T. P. Orlando; S. Gustavsson; W. D. Oliver. *A Quantum Engineer's Guide to Superconducting Qubits*. Applied Physics Reviews 6, 021318 (2019).

[16] F. Tafuri. *Fundamentals and frontiers of the Josephson effect*, volume 286. Springer Nature (2019).

[17] Y. Nakamura, Y. A. Pashkin, and J. S. Tsai, *Coherent control of macroscopic quantum states in a single-Cooper-pair box*. Nature (London) 398, 786 (1999).

[18] Bouchiat, V.; Vion, D.; Joyez, P.; Esteve, D.; Devoret, M. H. . *Quantum Coherence with a Single Cooper Pair*. Physica Scripta. IOP Publishing. T76 (1): 165-170 (1998).

[19] T.P. Orlando , J.E. Mooji , Lin Tian , Caspar H. van der Wal , L. Levitov , Seth Lloyd , J.J. Mazo. *A Superconducting Persistent Current Qubit*. Science 285, 1036 (1999).

[20] Schuster, David. *Circuit quantum electrodynamics* (2007).

[21] Joseph A. Valery, Shoumik Chowdhury, Glenn Jones, and Nicolas Didier. *Dynamical Sweet Spot Engineering via Two-Tone Flux Modulation of Superconducting Qubits*. PRX Quantum 3, 020337 (2022).

[22] David Zueco, Georg M. Reuther, Sigmund Kohler, and Peter Hänggi. *Qubit-oscillator dynamics in the dispersive regime: Analytical theory beyond the rotating-wave approximation*. Phys. Rev. A 80, 033846 (2009).

[23] Tahereh Abad, Anton Frisk Kockum, Göran Johansson. *Impact of decoherence on the fidelity of quantum gates leaving the computational subspace* (2023).

[24] John M. Martinis, S. Nam, J. Aumentado, K. M. Lang, and C. Urbina. *Decoherence of a superconducting qubit due to bias noise*. Phys. Rev. B 67, 094510 (2003).

[25] S.E. Rasmussen, K.S. Christensen, S.P. Pedersen, L.B. Kristensen, T. Bækkegaard, N.J.S. Loft, and N.T. Zinner. *Superconducting circuit companion - an introduction with worked examples*. PRX Quantum, 2(4):040204 (2021).

[26] Sebastian Probst, F.B. Song, Pavel A. Bushev, Alexey V. Ustinov, and Martin Weides. *Efficient and robust analysis of complex scattering data under noise in microwave resonators.* Review of Scientific Instruments, 86(2):024706 (2015).

[27] Gianluigi Catelani, Robert J. Schoelkopf, Michel H. Devoret, and Leonid I. Glazman. *Relaxation and frequency shifts induced by quasiparticles in superconducting qubits.* Physical Review B, 84(6):064517 (2011).

[28] R.M. Lutchyn, L.I. Glazman, and A.I. Larkin. *Kinetics of the superconducting charge qubit in the presence of a quasiparticle.* Physical Review B, 74(6):064515 (2006).

[29] J. Majer, J. M. Chow, J. M. Gambetta, Jens Koch, B. R. Johnson, J. A. Schreier, L. Frunzio, D. I. Schuster, A. A. Houck, A. Wallraff, A. Blais, M. H. Devoret, S. M. Girvin, R. J. Schoelkopf. *Coupling Superconducting Qubits via a Cavity Bus*. Nature 449, 443-447 (2007).

[30] S. Filipp, M. G¨oppl, J. M. Fink, M. Baur, R. Bianchetti, L. Steffen, and A. Wallraff1. *Multi-mode mediated exchange coupling in cavity QED* (2010).

[31] Shang-Yu Huang, Hsi-Sheng Goan. *Optimal control for fast and high-fidelity quantum gates in coupled superconducting flux qubits*. Phys. Rev. A 90, 012318 (2014).

[32] Ilya N. Moskalenko, Ilya A. Simakov, Nikolay N. Abramov, Alexander A. Grigorev, Dmitry O. Moskalev, Anastasiya A. Pishchimova, Nikita S. Smirnov, Evgeniy V. Zikiy, Ilya A. Rodionov, Ilya S. Besedin. *High fidelity two-qubit gates on fluxoniums using a tunable coupler*. Nature, 8, 130 (2022).

[33] Chengxian Zhang, Tao Chen, Xin Wang, Zheng-Yuan Xue. *Implementation of geometric quantum gates on microwave-driven semiconductor charge qubits*. Adv. Quantum Technol. 4, 2100011 (2021).

[34] Qiskit website: https://qiskit.org/

[35] M. Mottonen, J. J. Vartiainen. *Decompositions of general quantum gates*. Ch. 7 in Trends in Quantum Computing Research (NOVA Publishers, New York) (2006).

[36] Ciaran Hughes, Joshua Isaacson, Anastasia Perry, Ranbel F. Sun, Jessica Turner. *Quantum Computing for the Quantum Curious* (2021).

[37] J. M. Gambetta, F. Motzoi, S. T. Merkel, and F. K. Wilhelm. *Analytic control methods for high-fidelity unitary operations in a weakly nonlinear oscillator* Phys. Rev. A 83, 012308 (2011).

[38] F. Motzoi and F. K. Wilhelm. *Improving frequency selection of driven pulses using derivative-based transition suppression*. Phys. Rev. A 88, 062318 (2013).

[39] Zijun Chen, Julian Kelly, Chris Quintana, R. Barends, B. Campbell, Yu Chen, B. Chiaro, A. Dunsworth, A.G. Fowler, E. Lucero, E. Jeffrey, A. Megrant, J. Mutus, M. Neeley, C. Neill, P.J.J. O'Malley, P. Roushan, D. Sank, A. Vainsencher, J. Wenner, T.C. White, A.N. Korotkov, and John M. Martinis. *Measuring and Suppressing Quantum State Leakage in a Superconducting Qubit*. Phys. Rev. Lett. 116, 020501 (2016).

[40] David C. McKay, Christopher J. Wood, Sarah Sheldon, Jerry M. Chow, Jay M. Gambetta. *Efficient Z-Gates for Quantum Computing*. Phys. Rev. A 96, 022330 (2017).

[41] J T Muhonen et al. *Quantifying the quantum gate fidelity of single-atom spin qubits in silicon by randomized benchmarking* J. Phys.: Condens. Matter 27 154205 (2015).

[42] Claude Cohen-Tannoudji, Bernard Diu, and Frank Laloe. *Quantum Mechanics*. Quantum Mechanics, Volume 2 (1986).

[43] H. G. Ahmad, *Physics of the Josephson Effect in Junctions with Ferromagnetic Barriers towards Quantum Circuits and RF Applications* (2021).

[44] Mahdi Naghiloo. *Introduction to Experimental Quantum Measurement with Superconducting Qubits*. Quantum Physics (2019).

[45] Xianjing Zhou, Xinhao Li, Qianfan Chen, Gerwin Koolstra, Ge Yang, Brennan Dizdar, Yizhong Huang, Christopher S. Wang, Xu Han, Xufeng Zhang, David I. Schuster, Dafei Jin. *Electron charge qubits with 0.1 millisecond coherence time* (2022).

[46] Hanhee Paik, D. I. Schuster, Lev S. Bishop, G. Kirchmair, G. Catelani, A. P. Sears, B. R. Johnson, M. J. Reagor, L. Frunzio, L. Glazman, S. M. Girvin, M. H. Devoret, R. J. Schoelkopf. *Observation of High Coherence in Josephson Junction Qubits Measured in a Three-Dimensional Circuit QED Architecture*. Phys. Rev. Lett. 107, 240501 (2011).

[47] Ahmad, H. G., Jordan, C., van den Boogaart, R., Waardenburg, D., Zachariadis, C., Mastrovito, P., Georgiev, A. L. & Massarotti, D. *Investigating the Individual*

Performances of Coupled Superconducting Transmon Qubits. Condensed Matter, 8(1), 29 (2023).

[48] L. DiCarlo, J. M. Chow, J. M. Gambetta, Lev S. Bishop, B. R. Johnson, D. I. Schuster, J. Majer, A. Blais, L. Frunzio, S. M. Girvin, R. J. Schoelkopf. *Demonstration of Two-Qubit Algorithms with a Superconducting Quantum Processor*. Nature volume 460, pages240–244 (2009).

[49] Matthias Steffen, M. Ansmann, R. McDermott, N. Katz, Radoslaw C. Bialczak, Erik Lucero, Matthew Neeley, E. M. Weig, A. N. Cleland, and John M. Martinis. *State Tomography of Capacitively Shunted Phase Qubits with High Fidelity*. Phys. Rev. Lett. 97, 050502 (2006).

[50] F. Motzoi, J. M. Gambetta, P. Rebentrost, and F. K. Wilhelm. *Simple pulses for elimination of leakage in weakly nonlinear qubits*. Phys. Rev. Lett. 103, 110501 (2009). DOI: https://doi.org/10.1103/PhysRevLett.103.110501

[51] J. M. Chow, L. DiCarlo, J. M. Gambetta, F. Motzoi, L. Frunzio, S. M. Girvin, and R. J. Schoelkopf. *Optimized driving of superconducting artificial atoms for improved single-qubit gates*. Phys. Rev. A 82, 040305 (2010).

[52] Jozsa, Richard. *Fidelity for Mixed Quantum States*. Journal of Modern Optics, vol. 41, Issue 12 (1994).

[53] Michael A. Nielsen. *A simple formula for the average gate fidelity of a quantum dynamical operation*. Phys. Lett. A 303 (4): 249-252 (2002).

[54] Abad, T., Fernández-Pendás, J., Frisk Kockum, A., Johansson, G. *Universal Fidelity Reduction of Quantum Operations fromWeak Dissipation*. Phys. Rev. Lett. 2022,129, 150504 (2022).

[55] Jonas Bylander et al. *Noise spectroscopy through dynamical decoupling with a superconducting flux qubit*. Nature Physics 7.7 (2011).

[56] Christopher J. Wood and Jay M. Gambetta. *Quantification and characterization of leakage errors*. Phys. Rev. A 97, 032306 (2018).

[57] M. A. Rol, F. Battistel, F. K. Malinowski, C. C. Bultink, B. M. Tarasinski, R. Vollmer, N. Haider, N. Muthusubramanian, A. Bruno, B. M. Terhal, L. DiCarlo. *A fast, low-leakage, high-fidelity two-qubit gate for a programmable superconducting quantum computer*. Phys. Rev. Lett. 123, 120502 (2019).

[58] M. A. Rol; L. Ciorciaro; F. K. Malinowski; B. M. Tarasinski; R. E. Sagastizabal; C. C. Bultink; Y. Salathe; N. Haandbaek; J. Sedivy; L. DiCarlo. *Time-domain characterization and correction of on-chip distortion of control pulses in a quantum processor*. Appl. Phys. Lett. 116, 054001 (2020).

[59] Su-Kuan Chu, Chen-Te Ma, Rong-Xin Miao, Chih-Hung Wu. *Maximally Entangled State and Bell's Inequality in Qubits* (2017).

[60] Diego García-Martín, Germán Sierra. *Five Experimental Tests on the 5-Qubit IBM Quantum Computer*. Journal of Applied Mathematics and Physics Vol.6 No.7, 1460-1475 (2018).

[61] M. A. Nielsen and Isaac L. Chuang. P*rogrammable Quantum Gate Arrays*. Phys. Rev. Lett. 79, 321 (1997).

[62] David P. DiVincenzo. *Fault-tolerant architectures for superconducting qubits*. Phys. Scr. 2009, 014020 (2009).

[63] R. Barends et al. *Superconducting quantum circuits at the surface code threshold for fault tolerance*.Nature 508, 500 (2014).

[64] Charles H. Bennett, Gilles Brassard, Claude Crépeau, Richard Jozsa, Asher Peres, and William K. Wootters. *Teleporting an Unknown Quantum State via Dual Classical and Einstein-Podolsky-Rosenchannels*. Phys. Rev. Lett. 70, 1895 (1993).

[65] L. Steffen, Y. Salathe, M. Oppliger, P. Kurpiers, M. Baur, C. Lang, C. Eichler, G. Puebla-Hellmann, A. Fedorov, and A. Wallraff. *Deterministic quantum teleportation with feed-forward in a solid state system*. Nature 500, 319 (2013).

[66] J. E. Johnson, C. Macklin, D. H. Slichter, R. Vijay, E. B. Weingarten, John Clarke, and I. Siddiqi. *Heralded State Preparation in a Superconducting Qubit*. Phys. Rev. Lett. 109, 050506 (2012).

[67] D. Ristè, J. G. van Leeuwen, H.-S. Ku, K. W. Lehnert, and L. DiCarlo. *Initialization by Measurement of a Superconducting Quantum Bit Circuit*. Phys. Rev. Lett. 109, 050507 (2012).

[68] Yves Salathé, Philipp Kurpiers, Thomas Karg, Christian Lang, Christian Kraglund Andersen, Abdulkadir Akin, Sebastian Krinner, Christopher Eichler, and Andreas Wallraff. *Low-latency Digital Signal Processing for Feedback and Feed Forward in Quantum Computing and Communication*. Phys. Rev. Applied 9, 034011 (2018).

[69] M. Jerger, S. Poletto, P. Macha, U. H¨ubner, E. Il'ichev, and A. V. Ustinov, *Frequency division multiplexing readout and simultaneous manipulation of an array of flux qubits*. Applied Physics Letters 101, 042604 (2012).

[70] V. Schmitt, X. Zhou, K. Juliusson, B. Royer, A. Blais, P. Bertet, D. Vion, and D. Esteve, *Multiplexed readout of transmon qubits with Josephson bifurcation amplifiers*. Phys. Rev. A 90, 062333 (2014).

[71] E. Jeffrey, D. Sank, J. Y. Mutus, T. C. White, J. Kelly, R. Barends, Y. Chen, Z. Chen, B. Chiaro, A. Dunsworth, A. Megrant, P. J. J. O'Malley, C. Neill, P. Roushan, A. Vainsencher, J. Wenner, A. N. Cleland, and J. M. Martinis, *Fast accurate state measurement with superconducting qubits*. Phys. Rev. Lett. 112, 190504 (2014).

[72] S. Filipp, P. Maurer, P. J. Leek, M. Baur, R. Bianchetti, J. M. Fink, M. G¨oppl, L. Steffen, J. M. Gambetta, A. Blais, and A. Wallraff. *Two-qubit state tomography using a joint dispersive readout*. Phys. Rev. Lett. 102, 200402 (2009).

[73] L. DiCarlo, M. D. Reed, L. Sun, B. R. Johnson, J. M. Chow, J. M. Gambetta, L. Frunzio, S. M. Girvin, M. H. Devoret, and R. J. Schoelkopf. *Preparation and measurement of three-qubit entanglement in a superconducting circuit*. Nature 467, 574–578 (2010).

[74] H. -S. Yeo et al., *High-Fidelity Multiplexed Single-Shot Readout for Transmon Qubits With High-Power Measurement*. IEEE Transactions on Applied Superconductivity, vol. 33, no. 5 (2023).

[75] T. Walter, P. Kurpiers, S. Gasparinetti, P. Magnard, A. Potočnik, Y. Salathé, M. Pechal, M. Mondal, M. Oppliger, C. Eichler, and A. Wallraff. *Rapid High-Fidelity Single-Shot Dispersive Readout of Superconducting Qubits*. Phys. Rev. Applied 7, 054020 (2017).

[76] H. London, G. R. Clarke, and Eric Mendoza. *Osmotic Pressure of He^3 in Liquid He^4, with Proposals for a Refrigerator to Work below $1K$*. Phys. Rev. 128, 1992 (1962).

[77] Rohde&Schwarz ZVL6 Datasheet: https://www.testequipmenthq.com/datasheets/Rohde-Schwarz-ZVL6-Datasheet.pdf

[78] Keysight M3202A AWG data sheet: https://www.keysight.com/us/en/assets/7018-05392/data-sheets/5992-1798.pdf

[79] Keysight M3102A Digitizer data sheet: https://www.keysight.com/us/en/assets/7018-05399/data-sheets/5992-1805.pdf

[80] Labber software manual: https://www.keysight.com/us/en/assets/3122-1301/technical-overviews/M5401LxxA-Labber.pdf

[81] Keysight website: https://www.keysight.com/us/en/home.html

[82] $R\&S$ SMA100B RF generator datasheet: https://scdn.rohde-schwarz.com/ur/pws/dl_downloads/pdm/cl_brochures_and_datasheets/specifications/5215_1018_22/SMA100B_dat-sw_en_5215-1018-22_v0702.pdf

[83] Quantify: https://quantify-os.gitlab.io/

[84] Qblox website: https://www.qblox.com/

[85] QuantWare website: https://www.quantware.eu

[86] Julian Kelly et al. *Optimal quantum control using randomized benchmarking*. Physical review letters 112.24 (2014).

[87] Richard Versluis et al. *Scalable quantum circuit and control for a superconducting surface code*. Physical Review Applied 8.3 (2017).

[88] Austin G Fowler et al. *Surface codes: Towards practical large-scale quantum computation*. Physical Review A 86.3 (2012).

[89] Philip Krantz. *Investigation of Transmon Qubit Designs -A Study of Plasma Frequency Predictability*. (2010).

[90] Resonator tools from Sebastian Probst: https://github.com/sebastianprobst/resonator_tools.git

[91] Luigi Frunzio et al. *Fabrication and characterization of superconducting circuit QED devices for quantum computation*. IEEE Trans. on Appl. Superc. 15, 860-863 (2005).

[92] Xin-You Lü et al. *Two-qubit gate operations in superconducting circuits with strong coupling and weak anharmonicity* New J. Phys. 14 073041 (2012).

[93] Michiel A Rol et al. *Time-domain characterization and correction of on-chip distortion of control pulses in a quantum processor*. Applied Physics Letters 116.5 (2020).

[94] J. M. Chow, J. M. Gambetta, L. Tornberg, Jens Koch, Lev S. Bishop, A. A. Houck, B. R. Johnson, L. Frunzio, S. M. Girvin, R. J. Schoelkopf. *Randomized benchmarking and process tomography for gate errors in a solid-state qubit*. Phys. Rev. Lett. 102, 090502 (2009).

[95] J. Kelly, R. Barends, B. Campbell, Y. Chen, Z. Chen, B. Chiaro, A. Dunsworth, A. G. Fowler, I.-C. Hoi, E. Jeffrey, A. Megrant, J. Mutus, C. Neill, P. J. J. O'Malley, C. Quintana, P. Roushan, D. Sank, A. Vainsencher, J. Wenner, T. C. White, A. N. Cleland, John M. Martinis. *Optimal quantum control using randomized benchmarking*. Phys. Rev. Lett. 112, 240504 (2014).

[96] Aktar, Shamminuj & Bärtschi, Andreas & Badawy, Abdel-Hameed & Eidenbenz, Stephan. *A Divide-and-Conquer Approach to Dicke State Preparation* (2021).

[97] Samudra Dasgupta, Travis S. Humble. *Stability of noisy quantum computing devices* (2021).

[98] Yaakov S. Weinstein. *Pseudo-Random Circuits from Clifford Plus T-Gates*. Physical Review A 88, 062303, (2013).

[99] V. Negîrneac, H. Ali, N. Muthusubramanian, F. Battistel, R. Sagastizabal, M. S. Moreira, J. F. Marques, W. Vlothuizen, M. Beekman, N. Haider, A. Bruno, L. DiCarlo. *High-fidelity controlled-Z gate with maximal intermediate leakage operating at the speed limit in a superconducting quantum processor*. Phys. Rev. Lett. 126, 220502 (2021).

[100] Nielsen, Michael. *Quantum Computation and Quantum Information*. Cambridge University Press (2010).

[101] Denis Sych and Gerd Leuchs. *A complete basis of generalized Bell states*. New J. Phys. 11 013006 (2009).

[102] Hadamard decompositions by Quantum Inspire: https://www.quantum-inspire.com/kbase/hadamard/

[103] Daniel F. V. James, Paul G. Kwiat, William J. Munro, Andrew G. White. *On the Measurement of Qubits*. Physical Review A 64, 052312 (2001).

[104] Cramer, M., Plenio, M., Flammia, S. et al. *Efficient quantum state tomography*. Nat Commun 1, 149 (2010).

[105] Smithey, D.T., Beck, M., Raymer, M.G. and Faridani, A. *Measurement of the Wigner distribution and the density matrix of a light mode using optical homodyne tomography: Application to squeezed states and the vacuum.* Phys. Rev. Lett. 70, 1244–1247 (1993).

[106] Lvovsky, A.I. and Raymer, M.G. *Continuous-variable optical quantum-state tomography*. Rev. Mod. Phys. 81, 299–332 (2009).

[107] Cai, Z., Benjamin, S. *Constructing Smaller Pauli Twirling Sets for Arbitrary Error Channels*. Sci Rep 9, 11281 (2019).

[108] Shi Yu, Peng Xu, Xiaodong He, Min Liu, Jin Wang, Mingsheng Zhan. *Suppressing phase decoherence of a single atom qubit with CPMG sequence* (2013).

[109] Google Quantum AI. *Exponential suppression of bit or phase errors with cyclic error correction*. Nature 595, 383–387 (2021).

[110] Thomas E. Roth, Ruichao Ma, Weng C. Chew. *An Introduction to the Transmon Qubit for Electromagnetic Engineers* (2021).

[111] M. H. Devoret and R. J. Schoelkopf, *Superconducting circuits for quantum information: an outlook*. Science, vol. 339, no. 6124 (2013).

[112] A. P. M. Place, L. V. H. Rodgers, P. Mundada, B. M. Smitham, M. Fitzpatrick, Z. Leng, A. Premkumar, J. Bryon, A. Vrajitoarea, S. Sussman et al. *New material platform for superconducting transmon qubits with coherence times exceeding 0.3 milliseconds*. Nature Communications, vol. 12, no. 1 (2020)

[113] Yuan Xu, Ji Chu, Jiahao Yuan, Jiawei Qiu, Yuxuan Zhou, Libo Zhang, Xinsheng Tan, Yang Yu, Song Liu, Jian Li, Fei Yan, Dapeng Yu. *High-fidelity, high-scalability two-qubit gate scheme for superconducting qubits*. Phys. Rev. Lett. 125, 240503 (2020).

[114] Xiu Gu, Jorge Fernández-Pendás, Pontus Vikstål, Tahereh Abad, Christopher Warren, Andreas Bengtsson, Giovanna Tancredi et al. *Fast multi-qubit gates through simultaneous two-qubit gates*. PRX Quantum 2, 040348 (2021).